© Copyright 2017

Sarah M. Vorpahl

Correlating nanoscale optoelectronic and mechanical properties of solution processable thin film photovoltaic materials using scanning probe microscopy

Sarah Marie Vorpahl

A dissertation

submitted in partial fulfillment of the

requirements for the degree of

Doctor of Philosophy

University of Washington

2017

Reading Committee:

David Ginger, Chair

Brandi Cossairt

Xiaosong Li

Program Authorized to Offer Degree:

Chemistry

University of Washington

Abstract

Correlating nanoscale optoelectronic and mechanical properties of solution processable thin film photovoltaic materials using scanning probe microscopy

Sarah Marie Vorpahl

Chair of the Supervisory Committee:
Professor David S. Ginger
Chemistry

Solution processable materials present a competitive alternative to traditional silicon solar cells based on inexpensive processing and flexible form factors. Several competing technologies have entered the market in the past few years, including cadmium telluride and copper, indium, gallium, sulfur (CIGS) alloys. In addition to this nascent commercialized product, several emerging technologies also offer promising alternatives. Copper, zinc, tin, sulfur (CZTS) kesterite materials offers an earth abundant option, moving away from more price volatile minerals such as the indium used in CIGS. Hybrid perovskites (HPs) have been revealed as one of the most exciting new solution processable materials, with efficiency improving exponentially in just the past several years. This dissertation explores the underlying electrical and mechanical properties of both CZTS and HP thin films using scanning probe microscopy (SPM). Using several correlated SPM techniques, local functional properties are related to bulk performance as a way to help understand the fundamental properties that drive material characteristics.

TABLE OF CONTENTS

TABLE OF CONTENTS

LIST OF FIGURES

LIST OF TABLES

ACKNOWLEDGEMENTS

I first need to acknowledge the scientists that help me get me where I am today, including my colleagues past and present from both the Ginger and Hillhouse labs. To many to list, but I love you all. Special thanks to Profs David Ginger and Hugh Hillhouse for all your wisdom and guidance. I especially need to single out Dr. Raj Giridharagopal, who spent tireless hours getting me to the finish line. He is also my most favorite old person.

From my Seattle community: Lauren Kang, Soumya Samai, Jessica Kang, Sarah Holliday, Marylin+Jesse Leyva, Julieta Gruszko, Olivia Lenz, Sarah Fredrick, Tracy Hagan and all the CI crew, Kathryn Cogert, Nick Montoni, Juan Franco, Kevin O Malley, Ari Erikson (and sure, Ken too), Kimberly Davidson, Charlie Burrows, Robbyn Perdue, Elaine Klein, Stephanie Hemmingson, Jessica Whitman, Natalie Garcia, Jeremy Lehner, Dr. Felix Eickemeyer and all the beautiful members of the Seattle Peace Chorus. The whole Evans crew (Emily Finchum, Rebecca De Buen, Austin Sell, Emmi Obara, Nicole Kovski and especially Prof. Alison Cullen).

Every member, past and present from Women in Chemical Sciences, especially: Heidi Nelson, Addie Kingsland, Beth Mundy and Katie Corp. Very special acknowledgements to Profs. Brandi Cossairt, Sarah Keller and Dr. Kelly Edwards for always having my back.

From my Chicago community: Prof. Ken Nicholson, Prof. Emina Stojkovic, Valerie Henderson, Alance Ward, Sarah Mertz, Matty K., Gregg K,. Terra "Dopp" Dankowski., Lynda Wellhausen, Lauren Rodgers, Stephanie Levi and Marie Jaimes.

Always and forever: Justine Wolitzer, Kelly Brenner (and G too!), Emily Holtz, Lizzie Coyle, Justin and Matthieu Hughes-Nuger, Jason Sussberg, Kate Maclean, Tyler Moazed, Jen Weisberg, Steve Whitwall, Candace Hall, John Hann, Amanda and Sean and E.B. Wheaton (and Linda too!), Brian Lane, Jeff Flynn and Susan Parsons. And everyone else I am sure I am forgetting as I frantically race to the end.

To my extended families: Jean and Don Wolitzer, Noreen and Phil Hann, Ken and Georgeanne Nuger, Pat and Kathy Coyle and Lynne Brenner.

And of course to my family. Thank you for your love and support: Mom, Dad, Ellen and Phil.

And finally, Clare Isaacson. We really did make a great team.

DEDICATION

This dissertation is dedicated to my grandmother, Dorothy Fuchs. She was, and remains, the toughest woman I have ever known.

And to Calvin Elias Kohler, the reason we should be fighting like hell to protect our world.

Chapter 1. INTRODUCTION

1.1 MOTIVATION FOR ADVANCED ENERGY MATERIALS

Climate change and release of greenhouse gases (GHGs) increasingly threaten our planet and energy security. Developing clean energy technologies can help to mitigate increasing demand from the grid because of extreme weather events related to climate change. Solar power is the most readily abundant form of energy on the planet, with 174,000 TW of solar energy continuously hitting the earth, more than the approximately 150,000 TW used each year on earth. Currently, silicon solar panels are the most ubiquitous type of technology available holding around 90% of the market (MIT ref). However, these materials require intense processing and expensive equipment to become a commercial product. The capital expenditures (capex), or initial cost to build a 2 GW factory and stock it with the necessary equipment, for a complete raw silicon to module factory is around $2 billion dollars. This high start up costs limits the ability of new companies to successfully enter the market and impedes industry growth. Additionally, silicon modules are thick and rigid, meaning they have limited form factors than can be employed making them difficult to add to preexisting structures.

Photovoltaic materials that can be fabricated using solution processable ink routes can address both the problem of high capex and flexibility. These materials can be produced using a roll to roll processing technique, common to newspapers and plastic wrap, which increases the throughput of this technology and reduces the need for expensive purification and dicing equipment. Additionally, these materials are thin and flexible, allowing them to be integrated more readily into current structures as well as off grid technology important to newly electrifying and isolated markets.

This dissertation explores two solution processable photovoltaic materials; $Cu_2ZnSn(S,Se)_4$ (CZTSSe) and hybrid organic-inorganic perovskites (HPs). Both sets of work focus on the underlying optoelectronic and mechanical properties of these materials on the nanoscale. I use a set of correlated microscopies to understand the connections between local electronic properties and bulk photovoltaic functions.

1.2 Inorganic Thin Film Photovoltaic Material: CZTSSe

Thin film photovoltaics using copper zinc tin sulfoselenides, $Cu_2ZnSn(S,Se)_4$ (CZTSSe), are one type of solution processable materials for terawatt scale PV production. CZTSSe is a kesterite-type pentenary compound semiconductor with a direct band gap suitable for solar cell applications. One key attraction is that the component elements are all considered Earth-abundant, nontoxic materials. In addition, the band gap can be tuned from 1.45 to 0.96 eV by continuously replacing sulfur with selenium, which allows for matching the band gap to the solar spectrum.[1,2,3]

Although kesterite-related photovoltaics have been known since the late 1980s[4], this material has regained attention through the development of solution-based methods for fabrication of the active CZTSSe layer.[5,6,7,8] This technological achievement may eventually form the basis for commercially viable low-cost, large-area solar cell devices that could be printed and offer versatility in form factors.[9,10] The high crustal abundance of the constituent elements and high mineral extraction and production rates mean that CZTSSe may provide ultra-low cost electrical power without the financial risks associated with tellurium in CdTe or indium in $CuInGaSe_2$ (CIGSe). However, the record CZTSSe solar cell has an efficiency of 12.6%,[11] while several CIGSe devices with efficiencies greater than 20% have been reported.[12,13] This performance deficit is known to be due to several (potentially overlapping) physical phenomena in CZTSSe including the presence of local electrostatic potential fluctuations,[14] cation disorder,

large populations of defects and defect clusters,[15] and less passive grain boundaries.[16,17] Some or all of these cause decreased open circuit voltage and lower fill factor.[18] As a result, a better fundamental understanding of the materials chemistry of CZTSSe is needed along with the development of experimental techniques to remedy the problems

One of the main limitations of CZTSSe solar cells is the widely observed deficiency in open-circuit voltage (V_{OC}) compared to the band gap.[19] While the short-circuit current for CZTSSe can reach values of 37 mA/cm^2, close to the theoretical limit and comparable to what is typically observed in the case of $CuIn_xGa_{(1-x)}Se_2$ (CIGSe), both the fill factor (FF), typically <70%, and V_{OC}, typically <0.5 V, of solution processed CZTSSe cells fall short compared to their CIGSe counterparts.[20] Possible reasons for the observed voltage deficiency include recombination at the CdS/CZTSSe interface and low minority-carrier lifetimes in the active layer, possibly due to recombination at deep defects.[21] It has also been proposed that an interfacial layer formed at the CZTSSe/Mo interface, through the creation of a $MoSe_2$ layer, is likely to reduce the FF due to limitations on hole collection.[22] The intrinsic bulk material properties of kesterite and higher-order phases determined via bulk solar cell device characterization contribute decisively to the understanding of the device performance. However, it is not well-understood how the local, microscopic composition affects the electronic properties of the active layer.

In the case of CIGSe solar cells, scanning probe microscopy has been widely applied to understand the local structure of these high-efficiency chalcopyrite materials.[25-34] In particular, the study of the electronic nature of the CIGSe/CdS heterojunction, the electronic properties and types of grain boundaries, as well as the formation of trap/defect states, and the resulting band bending at grain boundaries have all attracted attention because of their importance to the overall device efficiency. Scanning Kelvin probe microscopy (SKPM) has been used to show that CIGSe, as well as

CZTSSe, films feature considerable heterogeneity in local electronic properties.[26.30,35,36]. This method detects the electrostatic force interaction between the tip and the sample to locally determine the work function of a given sample. Using this method we can construct maps of the difference in work function between the tip and surface, called the contact potential difference (CPD). We therefore use this technique to analyze the nanoscale spatial variation in work function arising from structural and chemical variations, which are of great interest for our materials. However, the origins for the contrast in observed surface potential variations, particularly in the case of CZTSSe, remain an area for speculation. *My work on CZTSSe explores how surface potential is connected to overall device performance in this material.*

1.3 Organic-Inorganic Thin Film Materials: Hybrid Perovskites

Perovskites are a group of materials having the general formula ABX_3, with calcium titanium oxide ($CaTiO_3$) being the prototypical structure that was studied after being discovered in the Ural mountains of Russia by Gustav Rose in 1936 (ref). In the most general formulation, the A and B sites are two differently sized cations, with A being larger than B, and the X site is an anion. A large class of perovskite oxide materials exist (where X = O) and have been studied for their myriad material properties such as superconductivity(ref) and ferroelectricity(ref). Another formulation of these materials is the hybrid organic-inorganic perovskite (HP). Here, the A site is typically an organic cation, such as methylammonium ($CH3NH_3^+$) or formamidinium ($CH(NH_2)_2^+$) (with more recent work using Cs^+ for an all inorganic crystal). The B site is a metal cation like lead (Pb^{2+}) or tin (Sn^{2+}). And finally, the X site is a halide, such as iodide (I-), bromide (Br-) or chloride (Cl-). Since 2009, this group of materials has been studied for its use as a photovoltaic material and the full scope of its remarkable material properties is still being realized. First, the precursors for these materials, simple salts made from different

combinations of the cations and anion (i.e. MAI, FAI, PbI2…) can be mixed to form inks. These inks can be easily deposited using any number of methods in the lab, such as doctor balding and spin coating, using relatively low temperatures (~100 °C). Looking towards commercialization, these simple solutions can also be made into thin films using a roll to roll printing method, such as employed by newspapers, which allows for large scale deployment.

In addition to being solution processable, the films that are created from these materials are shown to have exceptional optoelectronic properties such as high defect tolerance, high absorption coefficients, high open circuit voltage, long carrier lifetimes and diffusion lengths and a tunable bandgap as a function of halide content. The combination of these properties is remarkable compared to other solution processable thin films, including CZTSSe.

However, HPs are also highly unstable materials, with lifetimes on the order of days or even hours. To become a commercialized product it will be necessary to increase materials stability towards that of silicon, between 20-30 years (ref). Understanding the degradation pathways for HPs and their susceptibility to light, oxygen and moisture is a key to making them serious contenders on the solar cell market. Many recent studies are trying to understand the fundamental mechanisms of degradation (refs) while other work is being done to find more air and water stable formulations (refs). If this technological hurdle can be overcome, perovskites may have a chance of facing the markets as a single junction material. The more likely scenario that is being developed currently is exploiting the tunable bandgap of perovskites to act as a top layer material for silicon solar cells.(ref) Regardless of how commercialized this product becomes, it is clear that HPs are a remarkable class of materials with many possible optoelectronic applications. *My work looks at some of these fundamental properties, including*

degradation pathways, chemical composition as it relates to photoluminescence and ferroelectricity.

1.4 Scanning Probe Microscopy

Scanning probe microscopy is a technique that utilizes a tip with a sub-25-nm-radius apex attached to a microscopic cantilever. The local tip sample interactions are detected by recording the changes in the cantilever deflection captured by a photodiode. Depending on the dominant tip-sample interactions, we can collect local information about the topography, but also more complex electrical properties such as the local conductivity or work function. Measurements can be taken in either contact or non-contact mode depending on which electrical properties we are interested in probing.

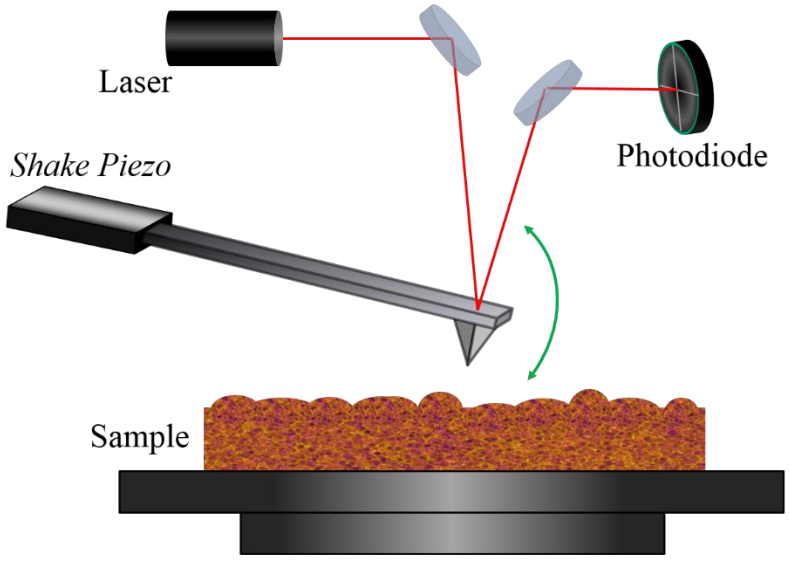

Figure 1 Atomic Force Microscopy Schematic
(Credit: Phil Cox)

One important electrical AFM technique I use to study a large variety of (semi)conducive thin films is conductive AFM. This contact technique characterizes variations in the sample

morphology while simultaneously probing the electrical current flowing between the sample and a metal-coated tip when a voltage bias is applied.

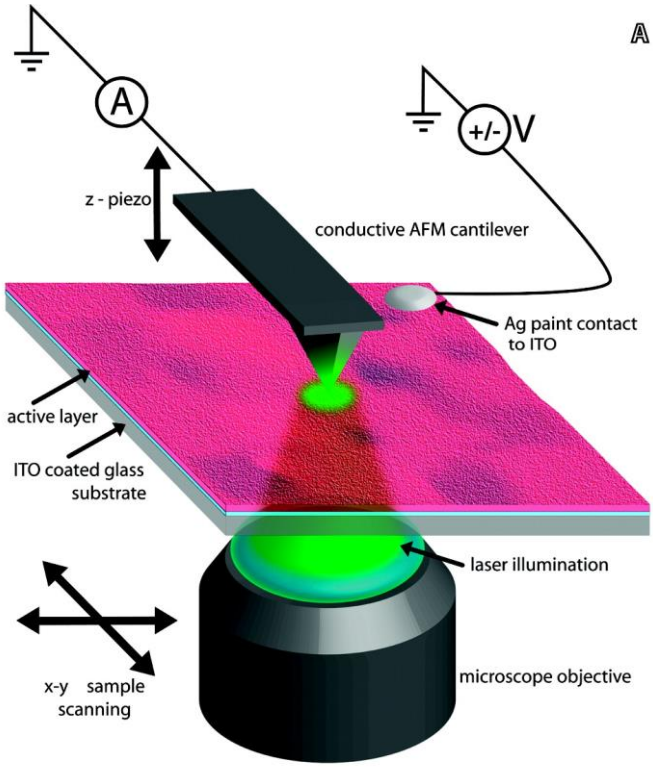

Figure 2 Photoconductive AFM Schematic

(from L.S.C. Pingree; O.G. Reid; D.S. Ginger (2010). "Electrical Scanning Probe Microscopy on Active Organic Electronic Devices". *Adv. Mater.* **21** (1): 19)

There are several ways we can use this technique. We can apply a constant bias/potential difference between the tip and the sample, for example in this case holes are first injected from the back-contact, then flow in the film, to be collected by the AFM tip. If the tip raster scans the sample, this measurement allows a correlation of the topographic features and the conductivity. For example, I will show you that the film morphology impacts the current intensity, which is related to the conductivity, and the current distribution across the films.

In order to estimate the local photovoltaic response, we can also perform this measurement by shining a light source (with known intensity) on a sample to create photo-generated carrier in the film and measure the current even when no external bias is applied. The photogenerated charges carriers in the film are transported to the different electrodes to generate a photo-current that is locally measure by using the AFM tip, this technique is called photoconductive AFM.

Another way to use this technique is by keeping the tip stationary and sweeping the voltage, while again collecting current through the tip. This measurement produces current-voltage characteristics which are important parameters for determining the efficiency of solar cells. However, for both methods there are experimental challenges with damaging the film given the contact with the surface (and potentially high voltages). Therefore, conductive AFM and photoconductive AFM help us to locally study the conductivity and the photo-response of our thin film materials.

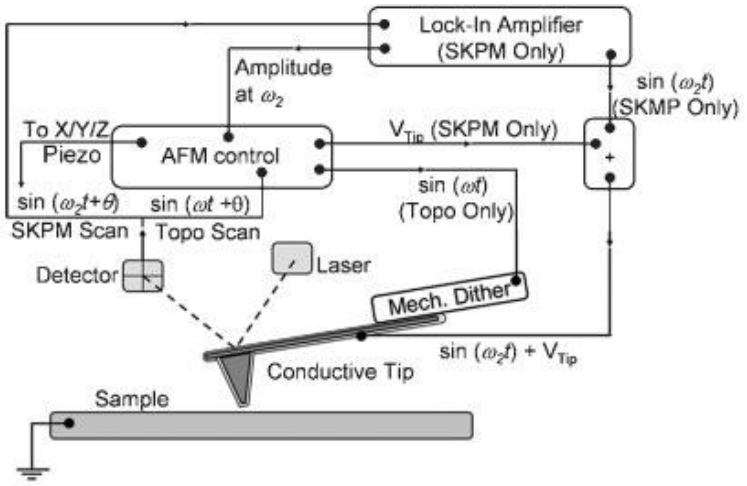

Figure 3 Scanning Kelvin Probe Microscopy Schematic

(from Pingree L S C, Reid O G and Ginger D S 2008 *Adv. Mater.* **20**)

Additionally, we want to be able to collect and study other local electronic properties in order to understand the differences between grains that may account for heterogeneities in the conductive

AFM signal. In perovskite for example, differences in interstitial ions, defects and traps may account for large local variations in collected current.

Another method to explore the heterogeneities between different grains in these thin films is a non-contact method called scanning Kelvin probe microscopy. Unlike conductive AFM that measures current, this method detects the electrostatic force interaction between the tip and the sample to locally determine the work function of a given sample. Using this method we can construct maps of the difference in work function between the tip and surface, called the contact potential difference. We can think about the meaning of the CPD a little later on. We therefore use this technique to analyze the relative nanoscale differences in work function arising from structural and chemical variations, which are of great interest for our materials.

To perform these measurements we can think of the AFM cantilever as a damped driven harmonic oscillator that is highly sensitive to changes in forces between the tip and the surface of the sample. The oscillations to the tip are driven by an applied AC bias at a given frequency called the resonance frequency which also has a characteristic amplitude. As the tip approaches the surface the changes in electrostatic forces induce a change in amplitude at the AC frequency. To actually measure these changes in forces SKPM uses a feedback loop to null out these electrostatic forces on the cantilever. By continually adjusting the applied voltage on the tip we maintain the condition that the bias on the tip minus the bias on the surface equals zero, thus canceling the oscillation at the AC frequency. The signal that is nulled out is in fact the contact potential difference.

This measurement of the CPD takes place during what's called the lift pass and it is the value you will see in my potential images throughout the talk. To ensure that our tip is only feeling the effect of long range electrostatic force, and not shorter range Van der Waal forces, we use a two

pass scanning technique. The first pass give us information about the topography of the film, in a standard AC mode AFM scan. The lift pass, raises the tip between 20-50 nm above the surface to ensure that it only measuring long range electrostatic forces.

Another important material property to probe on the nanoscale is ferroelectricity. Piezoresponse force microscopy (PFM) is a powerful technique for investigating local electromechnical response. This experiment employs a conductive tip in contact with the sample surface to apply a bias and measure mechanical vibrations. Specifically, this technique aims to measure the lattice formation that results from the converse piezoelectric effect, the creation of strain induced from an electrical field. This response can be measured using standard (vertical) PFM to look at polarization normal to the surface of the sample, which probes the up and down bending motion in the AFM tip and is seen as a vertical signal in the photodiode. PFM can also probe polarization that lies parallel to the sample surface using lateral PFM, which probes the twisting of the AFM tip and is read as the left to right displacement of the laser in the photodiode. Finally, local hysteresis loops that measure the coercive field necessary to switch domains from one metastable state to the next can be taken using dual amplitude resonance tracking (DART) mode (see Chapter 4 for further explanation and diagrams). In this measurement, the tip is again in contact with the sample surface and a voltage is ramped to collect the changing amplitude and phase response from the material. This technique has been used on a wide range of materials, from hard ceramics to soft biological samples and can produce both hysteresis loops and butterfly curves for each point scan.

1.5 SUMMARY

Chapter 2.1 investigates how the local work function of CZTSSe relates to local changes in ratios of sulfur (S) and selenium (Se) on the surface of the film. We use correlated maps of work

function from scanning Kelvin probe microscopy (SKPM) and chemical composition from energy dispersive X-ray spectroscopy (EDS) to understand the microscopic relationships between composition and electronic properties. We find that local fluctuations in the S/Se content leads to changes in the work function beyond the expected difference in CZTS and CZSTSe band gaps, suggesting that an increase in acceptor like defects is seen with increased S content.

Chapter 2.2 further investigates how processing conditions effect the energetic landscape of CZTSSe, using doped lithium (Li) films of CZTSSe from a molecular precursor route. Films incorporating Li directly into the precursor ink increase overall efficiency by 31%. We use SKPM correlated with conductive atomic force microscopy (cAFM) to understand how nanoscale electronic properties track with this boost in device parameters, especially for fill factor and shunt resistance. We find that the Li changes the polarity of the electric field at grain boundary and shows better over all current extraction from the bulk of the material. We hypothesize the Li competes for isoelectronic traps in the crystals and grain boundaries, creating grain boundaries that repel minority carriers and decrease recombination.

Turning to HPs in Chapter 3, we explore several aspects of this exciting new material. First, Chapter 3.1 looks at correlated photoluminescence and chemical maps from EDS to understand local heterogeneities in carrier lifetimes and non -radiative recombination at grain boundaries. We find that grain boundaries have dimmer PL and likely act as sites of non-radiative recombination, making their passivation an important issue for improving performance. We also find that there is a positive correlation between local chlorine content shown in EDS and PL intensity. Chapter 3.2 investigates the effects that both light and humidity have on the degradation and microstructure of HPs.

Chapter 4 looks at the electromechanical properties of HPs by investigating the ferroelectric nature of methylammonium lead iodide films using PFM.

Finally, Chapter 5 offers a perspective on policy drivers for increasing the penetration of renewables on the grid.

1.6 REFERENCES

1. Mitzi, D.; Gunawan, O.; Todorov, T.; Wang, K.; Guha, S. *Sol. Energy Mater. Sol. Cells* **2011**, 95, 1421–1436
2. Siebentritt, S.; Schorr, S. *Prog. Photovoltaics* **2012**, 20, 512– 519
3. Zhou, H.; Hsu, W.-C.; Duan, H.-S.; Bob, B.; Yang, W.; Song, T.-B.; Hsu, C.-J.; Yang, Y. *Energy Environ. Sci.* **2013**, 6, 2822– 2838
4. Ito, K.; Nakazawa, T. *Jpn. J. Appl. Phys. 1* **1988**, 27, 2094– 2097
5. Todorov, T.; Reuter, K.; Mitzi, D. *Adv. Mater.* **2010**, 22, E156– E159
6. Guo, Q.; Hillhouse, H.; Agrawal, R. *J. Am. Chem. Soc.* **2009**, 131, 11672– 11673
7. Yang, W.; Duan, H.; Bob, B.; Zhou, H.; Lei, B.; Chung, C.; Li, S.; Hou, W.; Yang, Y. *Adv. Mater.* **2012**, 24,6323– 6329
8. Ki, W.; Hillhouse, H. *Adv. Energy Mater.* **2011**, 1, 732– 735
9.Tian, Q.; Xu, X.; Han, L.; Tang, M.; Zou, R.; Chen, Z.; Yu, M.; Yang, J.; Hu, J. *CrystEngComm* **2012**, 14,3847– 3850
10.
Akhavan, V.; Goodfellow, B.; Panthani, M.; Steinhagen, C.; Harvey, T.; Stolle, C.; Korgel, B. *J. Solid State Chem.* **2012**, 189, 2– 12
11. W. Wang, M. T. Winkler, O. Gunawan, T. Gokmen, T. K. Todorov, Y. Zhu and D. B. Mitzi, *Adv. Energy Mater.*, 2013, **4**, 1301465
12. A. Chirila, P. Reinhard, F. Pianezzi, P. Bloesch, A. R. Uhl, C. Fella, L. Kranz, D. Keller, C. Gretener, H. Hagendorfer, D. Jaeger, R. Erni, S. Nishiwaki, S. Buecheler and A. N. Tiwari, *Nat. Mater.*, 2013, **12**, 1107–1111
13. P. Jackson, D. Hariskos, E. Lotter, S. Paetel, R. Wuerz, R. Menner, W. Wischmann and M. Powalla, *Prog. Photovoltaics*, 2011, **19**, 894–987
14. U. Rau and J. H. Werner, *Appl. Phys. Lett.*, 2004, **84**, 3735–3737
15. A. Walsh, S. Chen, S.-H. Wei and X.-G. Gong, *Adv. Energy Mater.*, 2012, **2**, 400–409
16. M. J. Romero, H. Du, G. Teeter, Y. F. Yan and M. M. Al-Jassim, *Phys. Rev. B: Condens. Matter Mater. Phys.*, 2011, **84**, 5
17. J. Li, D. B. Mitzi and V. B. Shenoy, *ACS Nano*, 2011, **5**, 8613–8619
18. T. Gokmen, O. Gunawan, T. K. Todorov and D. B. Mitzi, *Appl. Phys. Lett.*, 2013, **103**, 103506
19. Polizzotti, A.; Repins, I. L.; Noufi, R.; Wei, S.-H.; Mitzi, D. B. *Energy Environ. Sci.* **2013**, 6, 3171–3182
20. Siebentritt, S. *Thin Solid Films* **2013**, 535, 1– 4
21. Walsh, A.; Chen, S.; Wei, S.; Gong, X. *Adv. Energy Mater.* **2012**, 2, 400– 409
22. Gunawan, O.; Todorov, T.; Mitzi, D. *Appl. Phys. Lett.* **2010**, 97, 233506
23. Haight, R.; Shao, X.; Wang, W.; Mitzi, D. B. *Appl. Phys. Lett.* **2014**, 104, 033902
24. Redinger, A.; Mousel, M.; Wolter, M.; Valle, N.; Siebentritt, S. *Thin Solid Films* **2013**, 535, 291–295
25. Baier, R.; Abou-Ras, D.; Rissom, T.; Lux-Steiner, M.; Sadewasser, S. *Appl. Phys. Lett.* **2011**, 99,172102
26. Marron, D.; Sadewasser, S.; Meeder, A.; Glatzel, T.; Lux-Steiner, M. *Phys. Rev. B* **2005**, 71,033306
27. Sadewasser, S.; Glatzel, T.; Schuler, S.; Nishiwaki, S.; Kaigawa, R.; Lux-Steiner, M. *Thin Solid Films* **2003**,431, 257– 261

28. Sadewasser, S.; Glatzel, T. *Kelvin Probe Force Microscopy: Measuring and Compensating Electrostatic Forces*; Springer Verlag: Heidelberg, **2011**; Vol. 48.
29. Jiang, C.; Noufi, R.; Ramanathan, K.; AbuShama, J.; Moutinho, H.; Al-Jassim, M. *Appl. Phys. Lett.* **2004**,85, 2625– 2627
30. Jiang, C.; Noufi, R.; AbuShama, J.; Ramanathan, K.; Moutinho, H.; Pankow, J.; Al-Jassim, M. *Appl. Phys. Lett.* **2004**, 84, 3477– 3479
31.Jiang, C.; Contreras, M.; Repins, I.; Moutinho, H.; Yan, Y.; Romero, M.; Mansfield, L.; Nouf i, R.; Al-Jassim,M. *Appl. Phys. Lett.* **2012**, 101, 033903
32. Glatzel, T.; Steigert, H.; Sadewasser, S.; Klenk, R.; Lux-Steiner, M. *Thin Solid Films* **2005**, 480, 177–182
33. Takihara, M.; Minemoto, T.; Wakisaka, Y.; Takahashi, T. *Prog. Photovoltaics* **2013**, 21, 595– 599
34. Zhang, Z.; Hetterich, M.; Lemmer, U.; Powalla, M.; Holscher, H. *Appl. Phys. Lett.* **2013**, 102,023903
35. Li, J.; Chawla, V.; Clemens, B. *Adv. Mater.* **2012**, 24, 720– 723
36. Jeong, A.; Jo, W.; Jung, S.; Gwak, J.; Yun, J. *Appl. Phys. Lett.* **2011**, 99, 082103

Chapter 2. INVESTIGATING ELECTRICAL PROPERTIES OF CZTSSE

2.1 NANOSCALE SURFACE POTENTIAL VARIATION CORRELATES WITH LOCAL S/SE RATIO IN SOLUTION-PROCESSED CZTSSE SOLAR CELLS

Authors: Michael Salvador, Sarah M. Vorpahl, Hao Xin, Wesley Williamson, Guozheng Shao, Durmus U. Karatay, Hugh W. Hillhouse, David S. Ginger

2.1.1 *Overview*

Thin film solar cells made from Cu, Zn, Sn, S/Se can be processed from solution to yield high-performing kesterite (CZTS or CZTSSe) photovoltaics. We present a microstructural study of solution-deposited CZTSSe films prepared by nanocrystal-based ink approaches using scanning probe microscopy (SPM) and scanning electron microscopy (SEM) coupled with energy dispersive X-ray spectroscopy (EDS). We correlate scanning Kelvin probe microscopy (SKPM) maps of local surface potential with SEM/EDS images of the exact same regions of the film, allowing us to relate observed variations in surface potential to local variations in stoichiometry. Specifically, we find a correlation between surface potential and the S/(S+Se) composition ratio. In particular, we find that regions with molar S/(S+Se) > 0.1 are often associated with regions of more negative surface potential and thus higher work function. The change in work function is larger than the expected change in the valence band position with these small changes in sulfur, and thus the data suggest an increase in acceptor-like defects with increasing sulfur. These findings provide new experimental insight into the microscopic relationships between composition, structure and electronic properties in these promising photovoltaic materials.

2.1.2 *Introduction*

$Cu_2ZnSn(S_x,Se_{1-x})_4$ (CZTSSe) is a kesterite-type pentenary compound semiconductor with a direct band gap suitable for solar cell applications. One key attraction is that the component elements are all considered Earth-abundant, non-toxic materials. In addition, the band gap can be tuned from ≈1.45 to 0.96 eV by continuously replacing sulfur with selenium, which allows for matching the band gap to the solar spectrum.[1-3]

Although kesterite-related photovoltaics have been known since the late 1980's,[4] this material has regained attention through the development of solution-based methods for fabrication of the active CZTSSe layer.[5-8] This technological achievement may eventually form the basis for commercially viable low-cost, large-area solar cell devices that could be printed and offer versatility in form factors.[9,10]

One of the main limitations of CZTSSe solar cells is the widely observed deficiency in open-circuit voltage (V_{OC}) compared to the band gap.[11] While the short-circuit current for CZTSSe can reach values of 37 mA/cm^2, close to the theoretical limit and comparable to what is typically observed in the case of CIGSe, both the fill factor (FF), typically <70%, and V_{OC}, typically <0.5 V, of solution processed CZTSSe cells fall short compared to their CIGSe counterparts.[12] Possible reasons for the observed voltage deficiency include recombination at the CdS/CZTSSe interface and low minority-carrier lifetimes in the active layer, possibly due to recombination at deep defects.[12-15] It has also been proposed that an interfacial layer formed at the CZTSSe/Mo interface, through the creation of a $MoSe_2$ layer, is likely to reduce the FF due to limitations on hole collection.[14]

While a fundamental understanding of the factors limiting V_{OC} and FF is still lacking, there are indications that the complex origins of electronic defects derive in part from local

compositional variations including secondary phases and crystal lattice defects with mid-band-gap energies.[12,13] Additionally, the relative sulfur to selenium composition ratio for mixed kesterites can have important implications on device performance. For example, Redinger et al. observed that in the case of mixed S,Se kesterites the formation of ZnS at the buffer/absorber interface can lead to increased series resistance and interface recombination whereas this limitation is mostly inhibited in the pure Se kesterite.[16]

The intrinsic bulk material properties of kesterite and higher-order phases determined via bulk solar cell device characterization contribute decisively to the understanding of the device performance. However, it is not well understood how the local, microscopic composition affects the electronic properties of the active layer.

In the case of Cu(In, Ga)Se_2 (CIGSe) solar cells, scanning probe microscopy has been widely applied to understand the local structure of these high-efficiency chalcopyrite materials.[17-26] In particular, the study of the electronic nature of the CIGSe/CdS heterojunction, the electronic properties and types of grain boundaries, as well as the formation of trap/defect states and the resulting band bending at grain boundaries have all attracted attention because of their importance to the overall device efficiency. Scanning Kelvin probe microscopy (SKPM) has been used to show that CIGSe, as well as CZTSSe, films feature considerable heterogeneity in local electronic properties.[18,22,27,28] However, the origins for the contrast in observed surface potential variations, particularly in the case of CZTSSe, remain an area for speculation.

Herein, we seek to improve the understanding of how the local structure and composition can affect the micro- and nanoscopic electrical properties of CZTSSe films. We describe scanning probe microscopy (SPM), scanning electron microscopy (SEM) and energy dispersive X-ray spectroscopy (EDS) measurements on solution processed, hydrazine-free CZTSSe films

prepared by the nanocrystal route.[29] We carefully correlate topography, surface potential, and chemical composition on a nanometer scale (experimental details regarding device fabrication and characterization are described in the supporting information). By mapping the same sample area, we find a correlation between the local surface potential and the S/(S+Se) ratio. This correlation suggests that regions of the film with a higher S content have a deeper work function, indicative of a higher concentration of acceptor-like defect states, thus providing insight into how heterogeneous composition influences the electronic properties of these films.

2.1.3 *Discussion and Results*

Figure 1 shows a schematic representation of how we explore the local electronic properties and surface potential variations of solution processed polycrystalline CZTSSe films by combining SPM, SEM and EDS images. We fabricated CZTSSe thin films by solution processing using nanocrystal inks.[29] Films prepared in parallel were used for nanoscale characterization and for the fabrication of solar cells. SKPM is particularly suitable for correlating electronic properties with morphology in solar cell materials on the nanoscale[30,31] while SEM/EDS is capable of resolving chemical composition with sub-micron lateral resolution in thin films.[32]

Figure 2a shows the light and dark I-V curves of a full CZTSSe photovoltaic device. The solar cell yielded a total area power conversion efficiency of ~7.3% under simulated solar illumination based on a J_{SC} of 33.9 mA/cm^2, a V_{OC} of 0.39 V and a FF of 55%, which is in line with previous reports on these materials.[29] The series and shunt resistance of this device were 1.14 Ωcm^2 and 260 Ωcm^2, respectively. Figure 2b, c and d show the atomic force microscopy (AFM) topography (see also Figure S2), phase, and SKPM signal of the identical sample area of a CZTSSe film on a Mo-coated soda lime glass substrate. The topography for the CZTSSe film reveals that large, heterogeneous crystallites are created using the nanocrystal ink route (see also Figure S4).

Understanding the sign convention used for changes in potential in SKPM is critical for interpreting these images. SKPM measures nanoscale changes in electrostatic forces and/or force gradients between the AFM cantilever tip and the surface of the sample due to the contact potential difference (CPD). A more positive CPD is indicative of a region with a smaller work function (relative to the tip). Likewise, a more negative CPD is indicative of a region with a larger work function (relative to the tip).[33] For a semiconductor with a constant bandgap, the potential can reveal information about defects (i.e. a smaller work function would correspond to a region with more donor-like defects, and a larger work function to a region with more acceptor-like defects).

The SKPM image in Figure 2d reveals surface potential variations of the same magnitude (~200 mV) as previously reported SKPM data on CZTSSe films, albeit made using different processing techniques.[21,22,27] Furthermore, we observe large potential variations on topographically flat regions, and find similar topographic features with opposite potential contrast (Figure 2d and Figure S3) – both observations are consistent with signals that are dominated by electronic structure rather than topography. Figure 2d also shows a striking terraced pattern of alternating high and low surface potential on top of what appear to be individual CZTSSe crystallites in the topography image. Although not resolved in the topography image, we speculate that these variations in potential might be evidence of crystal terraces terminated with alternating crystallographic planes.[17,23] A structural analysis using electron backscattering diffraction might clarify these observations but is outside the scope of the present work.

The SKPM images show clear heterogeneity in surface potential, which seems consistent with the qualitative descriptions of the electronic properties of CZTSSe suggested by other studies.[27,34] However, SKPM by itself cannot explain the origin of the observed variations in

surface potential which can vary by nearly ~200 mV across a few hundred nanometers. The chemical composition of CZTSSe films is one factor that can influence the electronic properties of the films and, therefore, the power conversion efficiency of CZTSSe photovoltaic devices.[16,35] We thus asked if it is possible that microscopic compositional variations of the films are correlated with any of the observed differences in the surface potential seen in the CZTSSe films. To answer this question, we correlated our SKPM potential maps with SEM/EDS measurements (Figure S1).

The SEM map shown in Figure 3a features the exact same CZTSSe sample area as shown in Figure 2 (black square in Figure 3a; see also Figure S5). We acquired EDS maps of the Cu, Zn, Sn, S, and Se signals over the entire SEM image area (Figure S6), and we observed spatial variation in both the EDS maps and line traces of the individual elements (Figure S7). Notably, the spatial EDS signals of Se, Cu, and Zn are predominantly correlated with topography (film thickness). However, the EDS signal of S does not follow the same trend (Figure S7 – S9). Additionally, we ruled out any contribution of the Mo substrate to the measured S signal with a detailed analysis in the spectral overlap region of the S and Mo EDS signals (Figure S12 – S16).

We then performed an image correlation analysis on the SEM and AFM topography scans to exactly overlap with the corresponding EDS and SKPM maps (see Figure S10 for details). Figure 3c shows a correlated EDS map of the molar S/(S+Se) composition after median and Gaussian image filtering to reduce noise. Clear variations in the S/(S+Se) composition ratio are observed, ranging from essentially 100% Se (S/(S+Se)=0) to nearly 1 part S for every 6 parts of Se (see also Figure 3f).

Figure 3d overlays a filtered S/(S+Se) ratio map and the corresponding surface potential scan (see also Figure S11). While the correlation is not perfectly 1:1, it is clearly not random.

Importantly, we observe that areas of high S/(S+Se) ratio tend to be associated with areas of more negative surface potential (compare also Figure 2d for SKPM signal). Further comparison of the EDS and SKPM signals using EDS line scans supports our observation that the surface potential and the S/(S+Se) ratios are strongly correlated: an increase of the S/(S+Se) ratio leads to a more negative surface potential (Figure 3e, f).

Finally, Figure 4 summarizes the key findings of this work. The observed changes in local surface potential are directly related to variation in work function across the film. The band gap of CZTSSe is known to shift ~5 meV per 0.01 change in S/(S+Se) ratio.[34] The work function increase in regions of high S/(S+Se) ratio can be as high as 100 meV compared to the lowest regions of the film. Since this shift is larger than the expected change in the positions of the band edges over the observed range in composition (~40 meV for the valence band edge), we conclude that the change in work function over the S-rich regions is indicative of a higher concentration of acceptor-like defects in those areas (Figure 4). We believe it is plausible that the different intrinsic native point defect concentrations and ionization energies associated with the S-rich regions could lead to the observed band bending. Indeed, this hypothesis is consistent with the general observation that selenium rich devices are higher performing than the sulfur rich counterparts, hypothesized to result from fewer mid gap Shockley-Read-Hall active defects.[36] While a better understanding of the interplay between compositional and electronic inhomogeneity is still required, our current results thus lead us to speculate that a reduction in the local variation in S/(S+Se) ratio could lead to improved performance in solution-processed CZTSSe solar cell devices.

2.1.4 *Conclusion*

Using SPM and SEM techniques, we studied the nanoscale electrical and morphological properties of solution-processed CZTSSe films prepared by nanocrystal inks. We observed that the S/(S+Se) ratio is not spatially uniform over the surface of this film. We found that variations in the S/(S+Se) ratio were correlated with variations in surface potential from correlated SKPM potential maps. Specifically, we observed spikes in the S/(S+Se) ratio that matched with increases of the local work function, consistent with S-rich regions of the film featuring more acceptor like defects. Although the variations in S concentration are not likely responsible for all of the observed surface potential variations, they clearly play an important role in these films.

This work provides the first direct evidence that significant portions of the observed spatial variation in surface potential can be associated with local variations in the S/(S+Se) ratio for solution processed CZTSSe films. These findings suggest that it might prove useful to examine how different processing routes affect the homogeneity of the S/(S+Se) ratio across the film, and if those variations can be controlled to improve device performance.

2.1.5 *Appendix A*

2.1.6 *Acknowledgements*

This paper is based on research supported by the National Science Foundation Sustainable Energy Pathways program (CHE-1230615). M. S. acknowledges primary support from a fellowship by the Portuguese Fundação para a Ciência e a Tecnologia (SFRH/BPD/71816/2010). S. M. V. was supported by the Department of Defense (DoD) through the National Defense Science & Engineering Graduate Fellowship (NDSEG) Program.

2.1.7 *Figures*

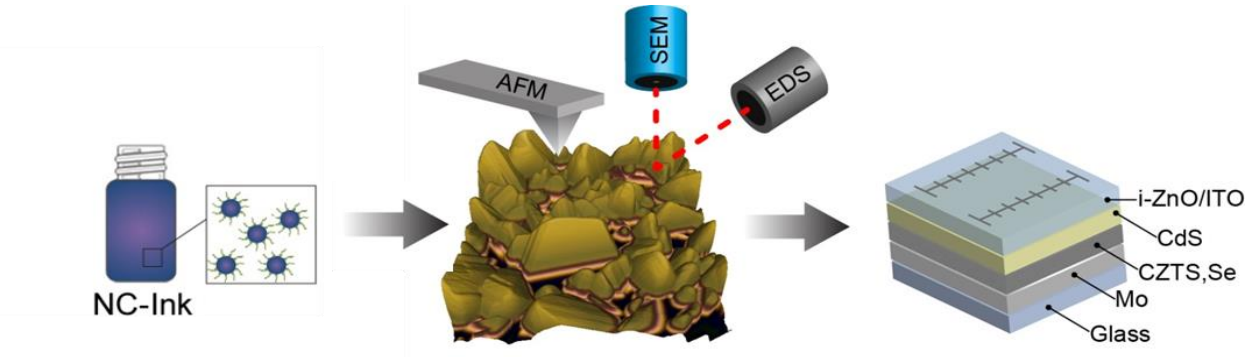

Figure 4 Scheme describing the work flow of nanoscrystal ink fabrication and characterization

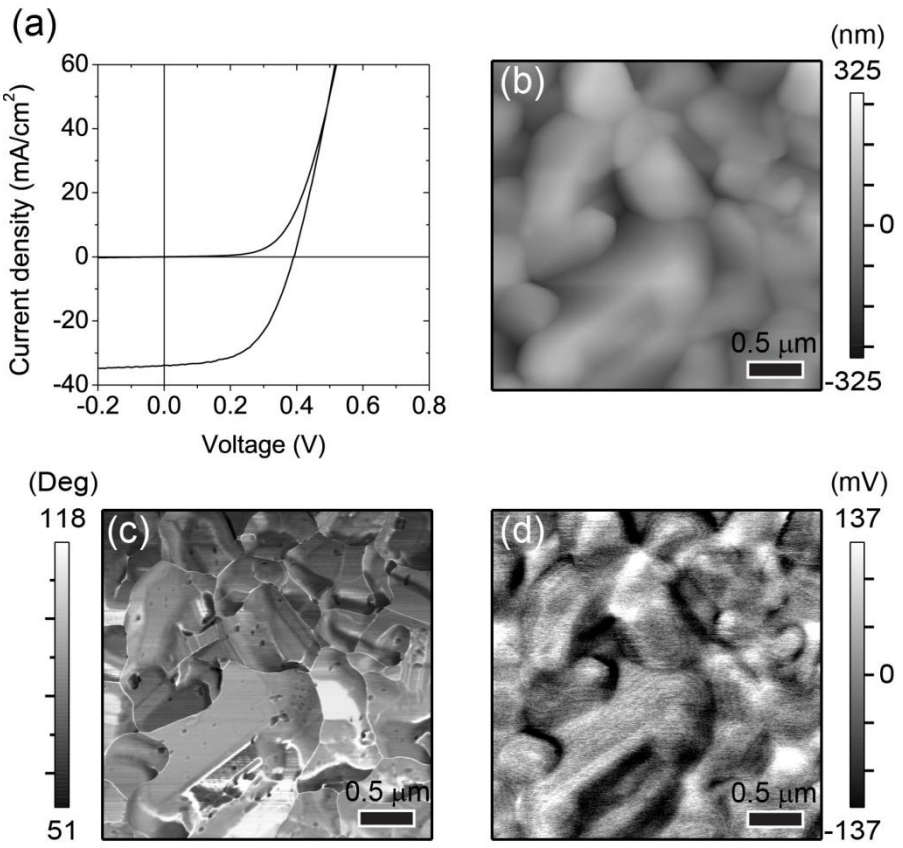

Figure 5 Device performance and SPM imaging using an active layer of nanocrystal precursor CZTS with post-selenium processing (CZTSSe)

a) dark and light I-V characteristics of a CZTSSe solar cell (same geometry as shown in Figure 1); b), c) and d) show the atomic force microscopy (AFM) topography, AFM phase signal and surface potential, respectively, of the same sample area (scale bar is 500 nm).

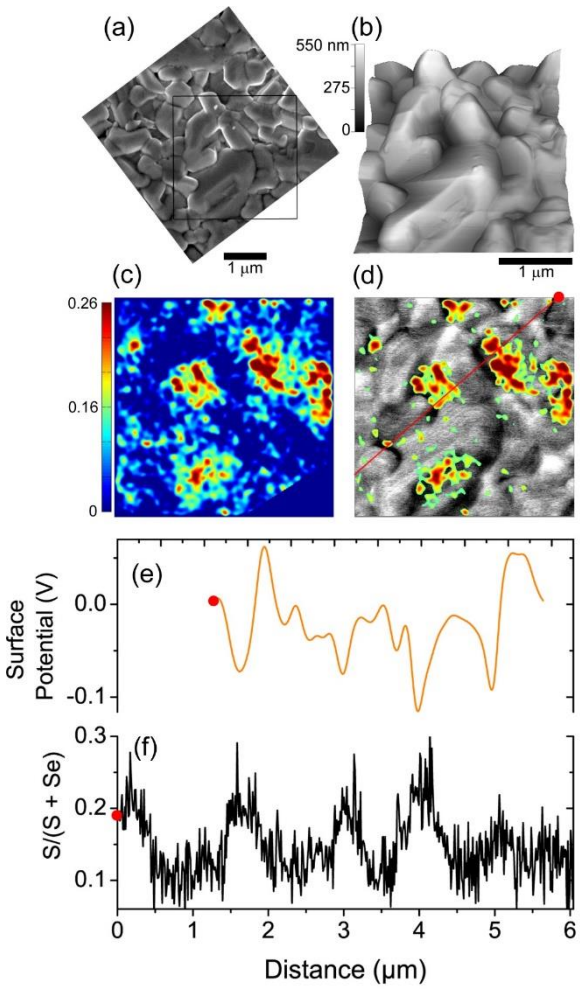

Figure 6 Correlation of SEM/EDS micrographs and line scans with SKPM data: molar S/(S+Se) ratios vs. surface potential.

a) SEM micrograph around the area scanned in Figure 2 (black square). The bar represents 1µm. b) 3D rendering of AFM topography. c) Correlated EDS map of S/(S+Se) ratio after median image filtering (before taking the S/(S+Se) ratio) and Gaussian image filtering (of the S/(S+Se) ratio). d) Overlaid images of correlated SKPM micrograph (grey scale, flattened) and S/(S+Se) EDS map (color). The SKPM micrograph is the same as in Figure 3b and is included here to clarify the correlation between composition and surface potential. e) and f) show the SKPM signal and S/(S+Se) ratio along the red line trace in d) (EDS line scan with 20

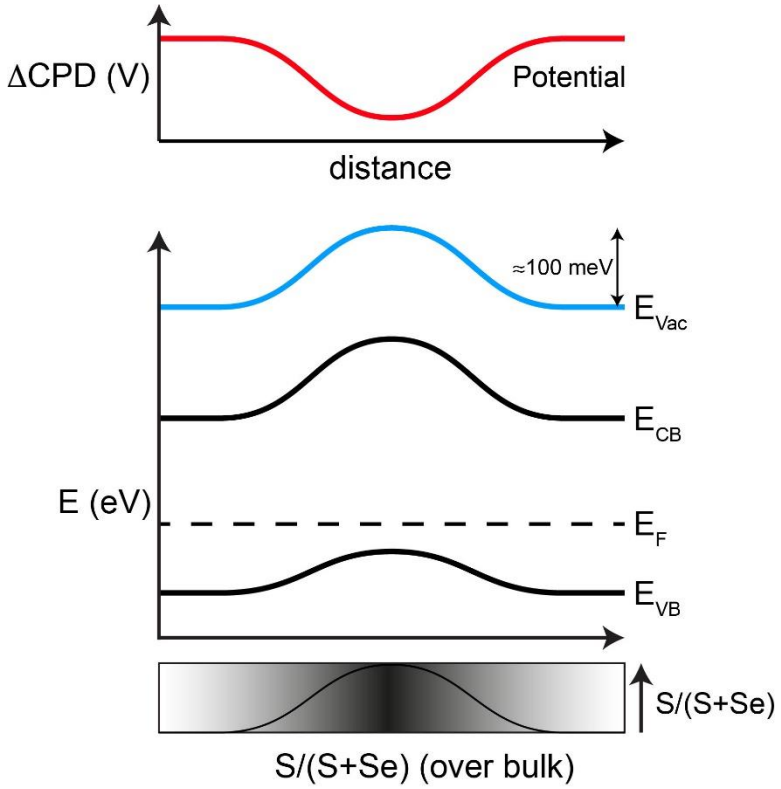

Figure 7 Schematic electronic band diagram describing the relation between contact potential difference (CPD) and S/(S+Se) ratio as extracted from experimental SKPM data

2.1.8 *References*

(1) Mitzi, D.; Gunawan, O.; Todorov, T.; Wang, K.; Guha, S. *Sol. Energy Mater. Sol. Cells* **2011**, *95*, 1421-1436.

(2) Siebentritt, S.; Schorr, S. *Prog. Photovoltaics* **2012**, *20*, 512-519.

(3) Zhou, H.; Hsu, W.-C.; Duan, H.-S.; Bob, B.; Yang, W.; Song, T.-B.; Hsu, C.-J.; Yang, Y. *Energ. & Environ. Sci.* **2013**, *6*, 2822-2838.

(4) Ito, K.; Nakazawa, T. *Jpn. J. Appl. Phys. 1* **1988**, *27*, 2094-2097.

(5) Todorov, T.; Reuter, K.; Mitzi, D. *Adv. Mater.* **2010**, *22*, E156-E159.

(6) Guo, Q.; Hillhouse, H.; Agrawal, R. *J. Amer. Chem. Soc.* **2009**, *131*, 11672-11673.

(7) Yang, W.; Duan, H.; Bob, B.; Zhou, H.; Lei, B.; Chung, C.; Li, S.; Hou, W.; Yang, Y. *Adv. Mater.* **2012**, *24*, 6323-6329.

(8) Ki, W.; Hillhouse, H. *Adv. Energy Mater.* **2011**, *1*, 732-735.

(9) Tian, Q.; Xu, X.; Han, L.; Tang, M.; Zou, R.; Chen, Z.; Yu, M.; Yang, J.; Hu, J. *CrystEngComm* **2012**, *14*, 3847-3850.

(10) Akhavan, V.; Goodfellow, B.; Panthani, M.; Steinhagen, C.; Harvey, T.; Stolle, C.; Korgel, B. *J. Solid State Chem.* **2012**, *189*, 2-12.

(11) Polizzotti, A.; Repins, I. L.; Noufi, R.; Wei, S.-H.; Mitzi, D. B. *Energ. & Environ. Sci.* **2013**, *6*, 3171-3182.

(12) Siebentritt, S. *Thin Solid Films* **2013**, *535*, 1-4.

(13) Walsh, A.; Chen, S.; Wei, S.; Gong, X. *Adv. Energy Mater.* **2012**, *2*, 400-409.

(14) Gunawan, O.; Todorov, T.; Mitzi, D. *Appl. Phys. Lett.* **2010**, *97,* 233506.

(15) Haight, R.; Shao, X.; Wang, W.; Mitzi, D. B. *Appl. Phys. Lett.* **2014**, *104,* 033902.

(16) Redinger, A.; Mousel, M.; Wolter, M.; Valle, N.; Siebentritt, S. *Thin Solid Films* **2013**, *535*, 291-295.

(17) Baier, R.; Abou-Ras, D.; Rissom, T.; Lux-Steiner, M.; Sadewasser, S. *Appl. Phys. Lett.* **2011**, *99,* 172102.

(18) Marron, D.; Sadewasser, S.; Meeder, A.; Glatzel, T.; Lux-Steiner, M. *Phys. Rev. B* **2005**, *71,* 033306.

(19) Sadewasser, S.; Glatzel, T.; Schuler, S.; Nishiwaki, S.; Kaigawa, R.; Lux-Steiner, M. *Thin Solid Films* **2003**, *431*, 257-261.

(20) Sadewasser, S.; Glatzel, T. *Kelvin Probe Force Microscopy: Measuring and Compensating Electrostatic Forces*; Springer Verlag: Heidelberg, 2011; Vol. 48.

(21) Jiang, C.; Noufi, R.; Ramanathan, K.; AbuShama, J.; Moutinho, H.; Al-Jassim, M. *Appl. Phys. Lett.* **2004**, *85*, 2625-2627.

(22) Jiang, C.; Noufi, R.; AbuShama, J.; Ramanathan, K.; Moutinho, H.; Pankow, J.; Al-Jassim, M. *Appl. Phys. Lett.* **2004**, *84*, 3477-3479.

(23) Jiang, C.; Contreras, M.; Repins, I.; Moutinho, H.; Yan, Y.; Romero, M.; Mansfield, L.; Noufi, R.; Al-Jassim, M. *Appl. Phys. Lett.* **2012**, *101*, 033903.

(24) Glatzel, T.; Steigert, H.; Sadewasser, S.; Klenk, R.; Lux-Steiner, M. *Thin Solid Films* **2005**, *480*, 177-182.

(25) Takihara, M.; Minemoto, T.; Wakisaka, Y.; Takahashi, T. *Prog. Photovoltaics* **2013**, *21*, 595-599.

(26) Zhang, Z.; Hetterich, M.; Lemmer, U.; Powalla, M.; Holscher, H. *Appl. Phys. Lett.* **2013**, *102,* 023903.

(27) Li, J.; Chawla, V.; Clemens, B. *Adv. Mater.* **2012**, *24*, 720-723.

(28) Jeong, A.; Jo, W.; Jung, S.; Gwak, J.; Yun, J. *Appl. Phys. Lett.* **2011**, *99,* 082103.

(29) Guo, Q.; Ford, G.; Yang, W.; Walker, B.; Stach, E.; Hillhouse, H.; Agrawal, R. *J. Amer. Chem. Soc.* **2010**, *132*, 17384-17386.

(30) O'Dea, J.; Brown, L.; Hoepker, N.; Marohn, J.; Sadewasser, S. *Mrs Bull.* **2012**, *37*, 642-650.

(31) Balke, N.; Bonnell, D.; Ginger, D.; Kemerink, M. *Mrs Bull.* **2012**, *37*, 633-637.

(32) Abou-Ras, D.; Caballero, R.; Fischer, C.; Kaufmann, C.; Lauermann, I.; Mainz, R.; Monig, H.; Schopke, A.; Stephan, C.; Streeck, C.; Schorr, S.; Eicke, A.; Dobeli, M.; Gade, B.; Hinrichs, J.; Nunney, T.; Dijkstra, H.; Hoffmann, V.; Klemm, D.; Efimova, V.; Bergmaier, A.; Dollinger, G.; Wirth, T.; Unger, W.; Rockett, A.; Perez-Rodriguez, A.; Alvarez-Garcia, J.; Izquierdo-Roca, V.; Schmid, T.; Choi, P.; Muller, M.; Bertram, F.; Christen, J.; Khatri, H.; Collins, R.; Marsillac, S.; Kotschau, I. *Microsc. Microanal.* **2011**, *17*, 728-751.

(33) Palermo, V.; Palma, M.; Samori, P. *Adv. Mater.* **2006**, *18*, 145-164.

(34) Chen, S.; Walsh, A.; Yang, J.; Gong, X.; Sun, L.; Yang, P.; Chu, J.; Wei, S. *Phys. Rev. B* **2011**, *83,* 125201.

(35) Haight, R.; Barkhouse, A.; Gunawan, O.; Shin, B.; Copel, M.; Hopstaken, M.; Mitzi, D. *Appl. Phys. Lett.* **2011**, *98,* 253502.

(36) Chen, S.; Walsh, A.; Gong, X.-G.; Wei, S.-H. *Adv. Mater.* **2013**, *25*, 1522-1539.

2.2 Lithium-Doping Inverts the Nanoscale Electric Field at the Grain Boundaries in Cu2ZnSn(S,Se)4 and Increases Photovoltaic Efficiency

Authors: Sarah Vorpahl, Hao Xin, Andrew. Collord, Ian Braly, Alexander Uhl, Brian Krueger, David. Ginger, and Hugh Hillhouse

2.2.1 *Overview*

Passive grain boundaries (GBs) are essential for polycrystalline solar cells to reach high efficiency. However, the GBs in Cu2ZnSn(S,Se)4 have less favorable defect chemistry compared to CuInGaSe2. Here, using scanning probe microscopy we show that lithium doping of Cu2ZnSn(S,Se)4 changes the polarity of the electric field at the GB such that minority carrier electrons are repelled from the GB. Solar cells with lithium-doping show improved performance, enabling a new record for solution-processed Cu2ZnSn(S,Se)4 from benign solvents. We propose that lithium competes for copper vacancies (forming benign isoelectronic LiCu defects) resulting in a reduction of donors like ZnCu. The effects of lithium doping reported here establish that extrinsic species are able to alter the bulk native point defect chemistry of Cu2ZnSn(S,Se)4 and tailor the nanoscale electric fields near the GB. This will be essential for this low-cost Earth abundant element semiconductor to achieve efficiencies that compete with CuInGaSe2 and CdTe.

2.2.2 *Introduction*

Thin film photovoltaics using copper zinc tin sulfoselenides, Cu2ZnSn(S,Se)4 or CZTSSe, are one of the most promising materials for terawatt scale PV production. The high crustal abundance of the constituent elements and high mineral extraction and production rates mean

that CZTSSe may provide ultra-low cost electrical power without the financial risks associated with tellurium in CdTe or indium in CuInGaSe2 (CIGSe). However, the record CZTSSe solar cell has an efficiency of 12.6%,1 while several CIGSe devices with efficiencies greater than 20% have been reported.2, 3 This deficit is known to be due to several (potentially overlapping) physical phenomena in CZTSSe including the presence of local electrostatic potential fluctuations,4 cation disorder, large populations of defects and defect clusters,5 and less passive grain boundaries.6, 7 Some or all of these cause decreased open circuit voltage and lower fill factor.8 As a result, a better fundamental understanding of the materials chemistry of CZTSSe is needed along with the development of experimental techniques to remedy the problems.

Many of the current paradigms for understanding the defect chemistry of CZTSSe are based on the knowledge of the defect chemistry of CIGSe since they are so closely related structurally. It is well known that the addition of sodium into CIGSe absorber layers during film processing is critical to produce high efficiency CIGSe solar cells. The effect was discovered unintentionally when soda-lime glass was used as the substrate over 20 years ago.9, 10 The current understanding of the role of sodium is based on several decades of experimental evidence9-17 and ab initio calculations18-20 that indicate that sodium increases the acceptor concentration, passivates defects, and aides grain growth leading to larger open-circuit voltage and fill factor. While the exact mechanism is still debated, it has been argued that sodium: (1) increases the p-type carrier concentration by providing a shallow acceptor NaIn,13, 18 (2) reduces the concentration of the deep level created by InCu defects by occupying copper vacancies,13, 17, 18, 20 (3) passivates grain boundaries by promoting oxidation of VSe defects,11, 16 (4) assists grain growth by forming Na2Sex that acts as a selenium fluxing agent,21 or (5) modifies the electrostatics at the GB19, 22 to repel holes from the GB and perhaps improve minority carrier

collection. While several of these effects may occur in parallel, there is particularly strong experimental evidence for sodium effecting band bending. Jiang et al.19 showed that sodium creates a downward bend in the CB at the GBs of high quality CIGSe that leads to devices with 19.2% efficiency. The downward bend is indicated by a positive spike in the contact potential difference (CPD) measured by scanning Kelvin probe microscopy (SKPM). However, Hanna et al.23 have argued that not all GBs are the same with regard to their electrostatics. Films with (112) or random orientation were shown to have a positive spike in the CPD at the GBs occurring at the top surface of the film (indicating downward bending of the CB), while films with (220/204) orientation showed a dip in the CPD at the GBs occurring on the surface of the film (indicating upward bending of the CB).

There have been far fewer studies focused on GBs or sodium in CZTSSe,24-26 but almost all good CZTSSe devices incorporate sodium since they are fabricated on soda lime glass and processed at high temperature (inherited from CIGSe). Experimentally, two studies have reported that CZTSSe has similar GB physics to CIGSe. Romero et al.6 compared cathodoluminescence in CZTSe and CIGSe and found a similar red-shift at the GBs in both samples, suggesting similar electrical properties at the GB. Additionally, Clemens et al.27 showed that a similar positive spike in the CPD appears at the GBs in both CZTSSe and CIGSe. Computationally, ab initio calculations have suggested that the GBs of CZTSSe should be significantly less passive7 than those of CIGSe. If this is true, a downward bend in the CB at the GB (drawing minority carrier electrons into the GB) could lead to increased recombination. As a result, the same nanoscale electrostatics that are beneficial for CIGSe may be deleterious for CZTSSe. More recently, another first principles study suggested that intrinsic CZTSe GBs are not passive due to the formation of Se-Se and Cu-Sn bonds at the GBs that result in deep level

states within the bandgap.28 Further, they suggest a mechanism involving migration of ZnSn, OSe and Na+i to explain the passivation of these states and the observation of downward band bending in SKPM experiments.

While it is exciting that many of the physical and chemical properties of CZTSSe and CIGSe are similar, CZTSSe devices still lag behind CIGSe devices, and understanding the differences between the materials may reveal opportunities to improve CZTSSe. There are some known differences in the bulk native point defect chemistry. For instance, the formation energies for the shallow acceptor and donor, CuZn and ZnCu, respectively, are small.29 The result is a highly compensated semiconductor (compared to CIGSe) where these two defects form a neutral defect cluster.

Here, we report experiments that significantly modify the defect chemistry of CZTSSe and enhance its optoelectronic quality and photovoltaic performance. We show the effects of Li doping in CZTSSe by incorporating LiF in the ink used to form the absorber layer. Previously, we reported 8.3% efficient CZTSSe solar cells from a solution of molecular complexes made by dissolving and complexing simple copper, zinc, and tin precursors with thiourea in a DMSO solvent.30 Compared to other solution phase processing techniques a DMSO molecular ink route has many advantages. It is much safer than hydrazine ink routes,1, 31 and it has fewer processing steps, higher material utilization, and greater reproducibility than nanocrystal-ink routes.31-33 It also provides a unique platform for easily introducing dopants and precisely controlling absorber stoichiometry. Here, we show that active area power conversion efficiencies of 10.5% (with no antireflective coating) can be achieved by adding LiF to a DMSO precursor ink. More importantly, we show that lithium incorporation dramatically changes the nanoscale electrostatics at the grain boundaries by using scanning Kelvin probe microscopy (SKPM).

Further, conductive AFM (cAFM) data show that the conductivity in the grain interiors as well as GBs increases by more than an order of magnitude with lithium incorporation. While Li2ZnSnS4 is a known wide-bandgap tetrahedrally coordinated semiconductor compound,34 to our knowledge this is the first report of lithium doping in CZTS, CZTSSe, or CZTSe. This report shows that not only can lithium be used to improve CZTSSe device performance, but that the paradigms inherited from CIGSe do not universally hold for CZTSSe. The knowledge of the defect chemistry and its effects on nanoscale electronic properties learned here provide a pathway for CZTSSe devices to reach much higher efficiencies.

2.2.3 *Results and Discussion*

Fig. 1a shows the current-voltage (J-V) characteristics of the best solar cells processed with and without LiF in the precursor ink. The maximum active area power conversion efficiencies (PCE) achieved in devices with and without LiF are 10.5% and 8.7%, respectively. The short circuit current density (Jsc), open circuit voltage (Voc), and fill factor (FF) for the two best devices are 34.9 mA/cm2, 0.452 V, and 66.4% and 31.9 mA/cm2, 0.444 V, and 61.3%, respectively. The average solar cell parameters based on 15 devices on the same substrate with standard deviations are summarized in Table 1. Improvements in all device parameters were observed after addition of LiF. Jsc increased by 5.6%, FF by 13.4%, and Voc by 5.2%, which lead to a 31% overall efficiency enhancement. The average series resistance (Rs) and shunt resistance (Rsh) extracted from the J-V curves are 0.38 Ω cm2 and 4095 Ω for devices with LiF and 0.53 Ω cm2 and 2781 Ω for devices without LiF. This is a 28% decrease in Rs and a 47% increase in Rsh. The lower Rs and higher Rsh in devices with LiF compared to that without LiF contribute to the higher FF. The average diode quality factor of the non-Li devices is 2.25 and decreases to 1.84 in the doped devices, revealing reduced recombination in the near-junction region of the absorber after Li

incorporation. Furthermore, Li doped devices show much higher uniformity as revealed by the much smaller standard deviations in every single device parameter (Table 1). The external quantum efficiency (EQE) spectra and the ratios of reverse biased to non-biased EQE [EQE(-1V)/EQE(0V)] of the solar cells are shown in Fig. 1b and 1c, respectively. EQE above 80% in the visible range with peak plateaus reaching 90% are observed in both films. Given that the lowest reflection

losses are expected to be about 10%, the high EQE suggests that the carrier collection efficiency is close to 100% in the CZTSSe near the junction.,38 This is further confirmed by the fact that the quantum efficiency at reverse-bias (Fig. 1c) for visible wavelengths does not change. Devices with Li doping show slightly higher EQE and lower [EQE(-1V)/EQE(0V)] ratio in longer (>800nm) wavelength. The better carrier collection efficiency at near infrared indicates a longer carrier diffusion length. The band gaps extracted from EQE data of lithium doped and non-Li devices are similar, but the band gap variation from Li-doped films is much smaller (Table 1). We note that the improvement in device performance with Li addition is highly reproducible. The average active area efficiency of 75 non-doped devices from 6 separate batches and 120 Li-doped devices from 8 batches are 7.00□1.44% and 9.46□0.94, respectively. For all side-by-side comparisons of batches of doped and non-doped, the minimum improvement in the doped was greater than 20% in each case.

Fig. 2 shows the scanning electron microscopy (SEM) images of the CZTSSe films processed with and without LiF. From the top view images (Fig. 2a and b), both films show densely packed grains with sizes up to several microns without obvious voids. No significant morphology change is observed with the lithium doped samples. Both cross section images (Fig. 2c and d)

show micron size grains extending through the absorber thickness. Some small voids are observed between the absorber layer and the back contact in both films. The X-ray diffraction (XRD) patterns (Fig. S1) show both films are predominantly kesterite phase, however, trace impurities of ZnSe or Cu2SnSe3 cannot be ruled out due to the overlap of the main XRD peaks. Both films with randomly oriented texture as determined by Lotgering factors23 (see Supplementary Information).

The stoichiometry of the absorber material measured by energy dispersive spectroscopy (EDS) is comparable for both films, Cu/(Zn+Sn)=0.74, Zn/Sn=1.14, and S/(S+Se)=0.10 for the film without LiF and Cu/(Zn+Sn)=0.72, Zn/Sn=1.16, and S/(S+Se)=0.10 for the film with LiF. Compared to the metal ratio in the precursor ink [Cu/(Zn+Sn)=0.714, Zn/Sn=1.04], about 10% of the tin is lost during selenization, presumably through the formation of volatile SnS or SnSe.39 The S/(S+Se) ratios measured by EDS agree well with those calculated from the XRD data (Table 1). No fluoride was detected by EDS, and it is likely lost as part of a volatile compound. EDS is not well suited for the detection of Li due to its small atomic mass. Therefore, the concentrations of Li in the films were determined using inductively coupled plasma mass spectroscopy (ICP-MS). The Li/Cu atomic ratio in the precursor ink is 0.023. After annealing, selenization, and soaking in DI water for 5 min, the Li/Cu atomic ratios were measured to be 7.3□10-3, 3.8□10-4, and 3.9□10-5 from samples of films scraped off the substrate (Fig. S2). The decrease of the Li/Cu ratio upon thermal annealing and selenization is very likely due to the evaporation of LiCl40 and/or Li2Se41,42 because of their low melting point and high vapor pressure The further reduce of Li after DI water soaking is due to dissolving of Li on the film

surface as confirmed by the XPS data (SI and Fig. S2). The atomic concentration of lithium in the selenized and washed film is 5.3□1016 cm-3.

To confirm the existence of Li on the surface prior to water rinsing and the absence of lithium rich surface compounds after rinsing, we conducted X-ray photoelectron spectroscopy (XPS) measurements (see Supplementary Information). As expected, Li and Na signals are detected on Li doped films after selenization. Both signals disappear after water soaking (Fig. S2). Although the exact mechanism of Li loss during annealing and selenization is not clear, it is possible that organolithium compounds, lithium chlorides, or lithium chalcogenides form and evaporate during annealing and selenization. In addition, we performed a LiF doping concentration dependence study (Table S1). Device improvements were achieved by doping the ink with LiF amounts as low as Li/(Cu+Zn+Sn)=0.0001. However, increased Li concentrations in the precursor ink resulted in improved device performance and homogeneity of the films.

We have also used SKPM and cAFM to characterize the nanoscale surface potential and conductivity of the CZTSSe absorber layer. Prior to performing these measurements, the films were soaked in DI water to remove any residual salts from the surface. As shown from XPS data (Fig. S3), no residual Na or Li is detectable on the film surface, thus the differences that we measure are the result of changes in the materials properties, not an artifact produced by a lithium rich surface layer. Fig. 3 shows both topography and potential maps of CZTSSe films from SKPM and accompanying line scans that show the correlation of topography and potential. In films without lithium doping, we observe a distinct positive peak in the contact potential difference (CPD) at the grain boundaries (Fig. 3a-c), consistent with previous studies of vacuum-

deposited CZTSSe films,27, 43 as well as studies of CIGSe films.44 This positive spike is consistent with a local accumulation of positive charge at the GB (local increase in the donor concentration), resulting in an electric field and several reports27, 28, 43 have suggested that this band bending facilitates electron collection through the GBs that is favorable for device performance. However, we show that in higher-performing Li-doped films there is a reversal of the electrostatics at the GBs. We find a dip in the CPD at the GB (Fig. 3d-f) for these Li doped films. This result is consistent with a local accumulation of negative charge at the GB resulting in an electric field and upward band bending towards the GB (Fig. 5b). We conclude that this inversion of electrostatics at the GB is a result of the incorporation of Li in the films and modification of the local defect chemistry. Because the GBs of CZTSSe are less passive than those of CIGSe, the band bending shown in Fig. 5b should be beneficial to device performance by creating a barrier for the minority carrier electrons to cross into the GB.

Assuming a constant bandgap, this upward band bending at the GB is equivalent to a local increase in the acceptor concentration at the GB. However, it is also possible that a thin layer of a lithium compound such as Li2O, Li2S, Li2Se, Li2SnO3, or Li2ZnSn(S,Se)4 forms at the GB, or the lithium acts as a catalyst for the formation of oxide compounds such as SnO2 or ZnO. Given the large bandgaps of all these compounds, they would result in a type II band offset so long as their work function is not significantly smaller than the bulk CZTSSe. As a result, band diagrams shown in Fige 5c are also possible. Based on the SKPM data alone, we cannot confirm or rule-out this hypothesis. However, if such layers do form, their effect would be to repel electrons away from the GB and block holes from entering the GB. The dramatic increase in shunt resistance is also likely related to the GBs given the similar morphology of the films with

and without lithium. If the GBs were a source of shunts, the creation of upward band bending at the GB would repel minority carrier electrons and increase the shunt resistance.

Li doping also dramatically affects the conductivity as shown in cAFM images (Fig. 4). For these conductivity maps, the current was collected by applying a positive voltage while raster scanning the AFM tip in contact with the sample. Films were not damaged under repeated scanning (Fig. S4 and S5). The biases applied to films with and without LiF were 100 mV and200 mV, respectively. From Fig. 4a and 4b we observe that the
Li-doped film shows greatly improved conductivity, even under a smaller applied bias. The current observed in the doped film is more than one order of magnitude higher than the current observed in the film without doping. Additionally, the conductivity of doped films is improved at both GBs and grain surfaces. We found that the conductivity in films without Li was consistent with that observed in CZTSSe27 and CIGSe45 films in the literature, with more conductive GBs than grain surfaces. The higher conductivity of both GBs and grain surfaces in Li-doped films is evidence of lithium being present and active throughout the entire film rather than just at the GBs. From a steric perspective, we note that sodium has a much larger Shannon radius (99 pm for tetrahedral coordination) than copper(I) (60 pm), but lithium (59 pm) is comparable in size to copper(I), zinc (60 pm) and tin(IV) (55 pm). This may allow lithium to be more easily incorporated into the bulk of the CZTSSe lattice and affect the defects and defect clusters in the bulk.

There are several possible mechanisms by which lithium could increase device performance and increase conductivity. Lithium could compete for copper vacancies and thereby: (1) reduce the

concentration of the shallow donor ZnCu (reducing compensation and increasing the p-type carrier concentration), (2) reduce the formation of the neutral defect complexes [VCu+ZnCu] and [CuZn+ZnCu], or (3) reduce the formation of the deep acceptor SnCu, (reducing SRH recombination and increasing the Voc, carrier diffusion length, and current collection efficiency while decreasing the diode quality factor). Lithium could also (4) form a Se fluxing compound that facilities selenization (reducing the concentration of the donor VSe), or (5) catalyze oxidation at the grain boundaries (forming OSe).16 It is also possible that (6) Li substitutes on Zn site forming a (likely) shallow acceptor LiZn. This could reduce the CuZn acceptor concentration, but if LiZn is shallower than CuZn then it would lead to a net increase in the p-type carrier concentration due to more complete ionization of the shallower acceptor. Effects (4) and (5) would result in a lower concentration of donor defects and could explain the increase in conductivity. However, because of the predicted high formation energy of VSe (>2.3 eV)29 we would expect that such defects are primarily present at surfaces and GBs and thus it would not explain the dramatic increase in the conductivity of the crystalline bulk. Similarly, for explanation (3), the predicted formation energy of SnCu is large (>1.7 eV) even under Cu-poor conditions.29 Therefore, the most likely explanations for the beneficial effect of lithium in CZTSSe are (1), (2), and (6).

These conclusions are consistent with the results of Nagaoka et al.25 who investigated the effects of sodium on CZTS single crystals. They found that sodium increased the effective hole concentration and reduced the thermal activation energy of conduction. This occurred along with a decrease in compensation and an increase in mobility, leading the authors to conclude that sodium occupies copper vacancies and prevents the formation of ZnCu. Thus we find lithium has

many of the same beneficial effects as sodium in the bulk, but the effects on the GBs are very different.

Direct measurements of carrier concentration would help elucidate exactly which mechanism (or mechanisms) are responsible for the improvements. However, for devices on a conductive back contact, Hall effect measurements are not possible, and thus we use capacitance-voltage (C-V) techniques. While these do not reveal an unambiguous carrier concentration, they do give insight about ionizable defects in the absorber layer of the completed PV devices. Drive-level capacitance profiling (DLCP) is an improvement on conventional C-V profiling. In DLCP the magnitude of the AC signal is extrapolated to zero. As a result, the measured room temperature DLCP concentration (NDLCP) quantifies the spatially dependent density-of-states that the quasi-Fermi levels sweep through. These include shallow states at the border between the depletion region and quasi-neutral region (that act like dopants) and deeper levels in the depletion region closer to the junction that can respond at the given frequency and temperature (that act as recombination centers). As a result, NDLCP, min at room temperature is not simply the carrier concentration, but a combination of shallow and deep defects.

DLCP data were collected for a large number of CZTSSe devices including devices based on DMSO molecular inks with and without LiF. We observe a general trend of increasing Voc with decreasing NDLCP, Min (Fig. S6). This is due to passivation of moderately deep defects that improve Voc. However, the average NDLCP, min for Li-doped and non-Li devices are 3.5x1015 cm-3 and 5x1015 cm-3, respectively. The difference is not statistically significant. However, Li containing devices do show statistically significant increases in Voc and decreases in diode

quality factor (Table 1), which indicates a reduction of deep defect states (at GB's, in the bulk, or at interfaces) by the addition of lithium. This result suggests that the states being affected are deeper than those that respond to the DLCP measurement at this frequency and temperature. Assuming a thermal emission prefactor similar to that in CIGSe,46 these states must be deeper than 0.4 eV above the valence band maximum in order not to contribute to NDLCP.

2.2.4 *Conclusions*

In summary, we report highly efficient CZTSSe solar cells with LiF addition directly from molecular precursor solutions. Structure, morphology, composition, contact potential and conductivity characterizations including XRD, ICPMS, EDS, SEM, XPS, SKPM and cAFM confirm that LiF greatly improves CZTSSe absorber material electronic quality. Notably, the improvements in device performance achieved with Li doping are accompanied by a concomitant inversion of the potential spike typically observed at CIGSe and CZTSSe grain boundaries. Our observation of a negative spike at the grain boundaries challenges the conventional wisdom that a positive spike at the boundaries is an inherent feature of better-performing devices. Additionally, the method of doping demonstrated here (direct addition to a precursor ink) is relatively simple. The 10.5% efficiency is the highest efficiency CZTSSe solar cell fabricated from solution processing in a non-hydrazine solvent. The additional control over defect chemistry enabled via solution doping opens the door to further improvements in CZTSSe solar cell efficiency, making an important step in the development of scalable manufacturing methods to produce terawatts of high efficiency PV modules.

2.2.5 *Appendix B*

2.2.6 *Acknowledgements*

The acknowledgements come at the end of an article after the conclusions and before the notes and references. H.W.H. and A.D.C. acknowledge support from the U. S. Department of Energy SunShot Initiative, Next Generation Photovoltaics 2 Program (DE-EE00053210). I.L.B. and H.W.H. acknowledges the National Science Foundation Sustainable Energy Pathways award (CHE-1230615) for supporting the DCLP measurements. D.S.G. and S.M.V. acknowledge the National Science Foundation Sustainable Energy Pathways award (CHE-1230615) for funding the SKPM and cAFM experiments. S.M.V. acknowledges fellowship support from the NDSEG program. A.R.U. acknowledges the financial support from the Swiss National Science Foundation (SNSF) under project number P2EZP2_152168.

2.2.7 *Figures*

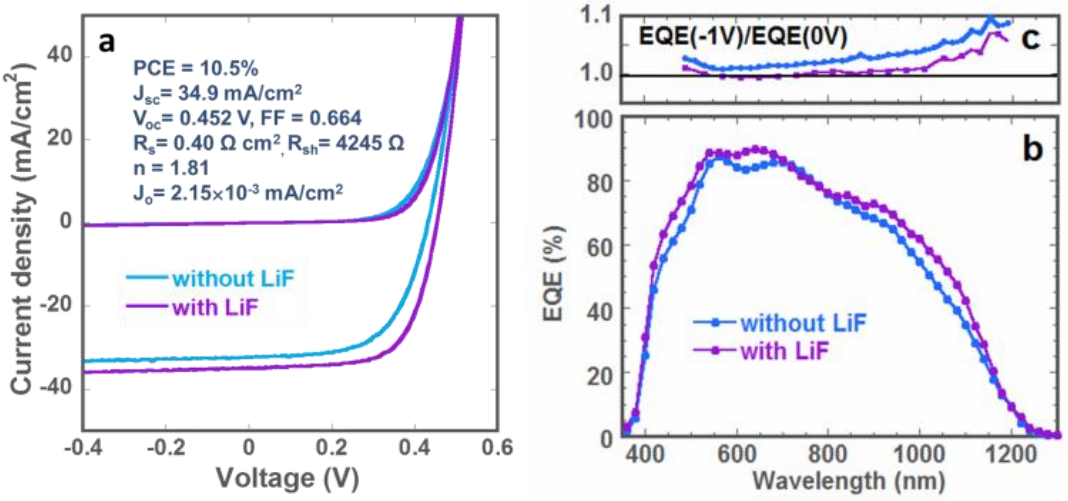

Figure 8 Current-voltage response and external quantum efficiency of CZTSSe solar cells with and without Li doping.

(a) J-V characteristics of the best CZTSSe solar cells measured in dark and under AM 1.5 simulated sunlight with the absorber films processed without and with LiF. The solar cell parameters of the Li-doped champion device are shown in the inset. (b) External quantum efficiency (EQE) of the solar cell. (c) Ratio of EQE measured under -1V bias verse 0V bias.

Table 11 Summary of material and photovoltaic device characteristics of CZTSSe films and devices with and without LiF

LiF	Cu/ (Zn+Sn)	Zn/Sn	S/(S+Se) XRDa/EDX	Ega (eV)	Jsc (mA/cm2)	Voc (V)	FF (%)	PCE (%)	n	Rs (Ω cm2)	Rsh (Ω)
No	0.74	1.14	0.09/010	1.08±0.023	32.2±0.6	0.426±0.011	57.8±2.6	7.93±0.47	2.25±0.16	0.53±0.11	2781±117
Yes	0.72	1.16	0.10/0.10	1.07±0.007	34.1±0.8	0.448±0.003	65.6±0.9	10.04±0.35	1.84±0.05	0.38±0.02	4095±54

a. Calculated from fitting the linear portion of (ln(1-EQE))2 versus energy.

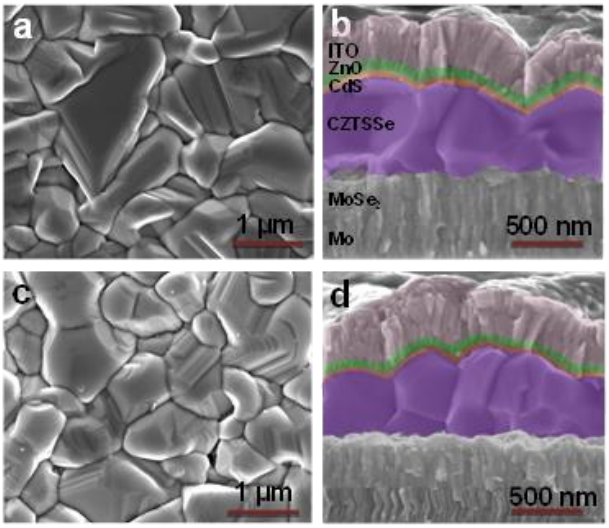

Figure 9 SEM images of CZTSSe absorber films.

(a,b) Top view (a) and cross section (b) SEM images of non-Li films. (c,d) Top view (c) and cross section (d) SEM images of Li-doped CZTSSe films. The cross section images (b) and (d) were measured from cleaved solar cell devices.

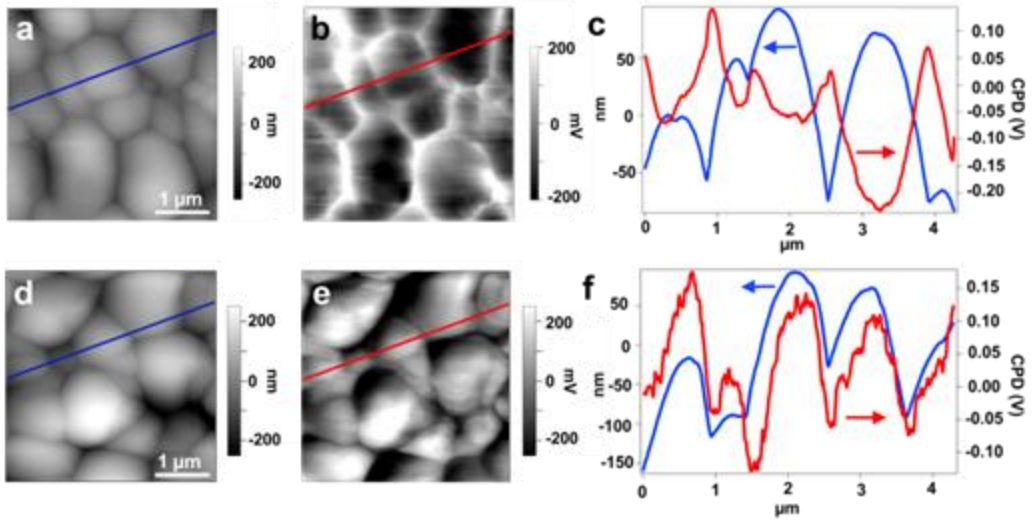

Figure 10 AFM topography images and SKPM potential maps.

(a,b,c) AFM topography (a), SKPM potential map (b), and plots of the topography and potential linescans (c) of CZTSSe films without Li-doping. (d,e,f) AFM topography, (d) potential map (e), and plots of the topography and potential linescans (f) of CZTSSe films with Li-doping.

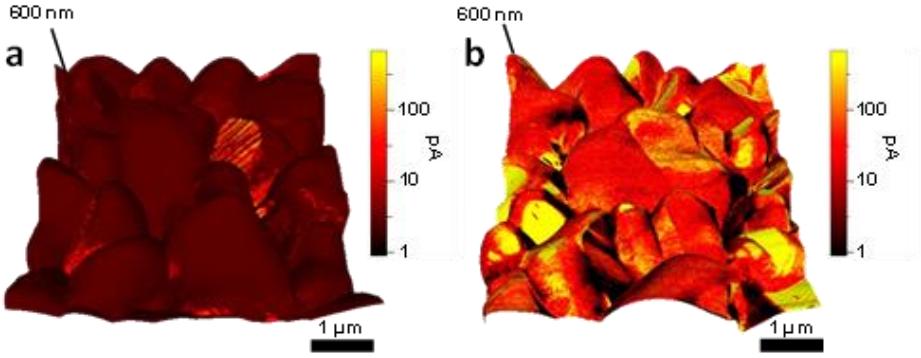

Figure 11 cAFM images. cAFM conductivity maps overlaid on AFM topography images for films without (a) and with (b) Li doping.

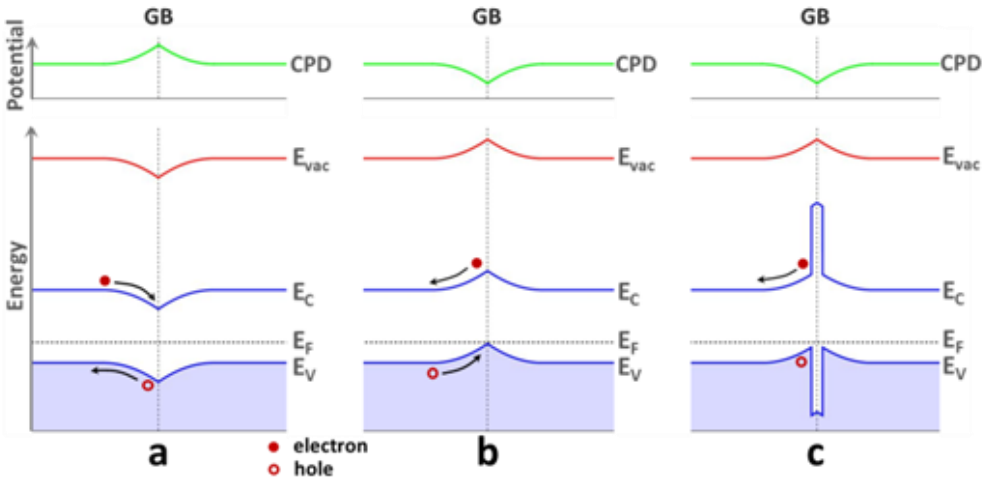

Figure 12 Schematic of the contact potential difference (CPD) from SKPM and band diagrams across a gain boundary (GB).

A positive spike in the CPB at the GB, which is observed for films with no lithium. (b) A dip in the CPD at the GB assuming constant bandgap. (c) A dip in the CPD at the GB along with the formation of a higher bandgap material at the GB. Li-doped films show a dip in the CPD at the GB as shown in panel (b) and (c). However, SKPM cannot distinguish between (b) and (c). The high bandgap material at the GB in part (c) is hypothesized to be Li2O, Li2Se, Li2ZnSnSe4, Li2SnO3, SnO2 or similar compound.

2.2.8 *References*

1. W. Wang, M. T. Winkler, O. Gunawan, T. Gokmen, T. K. Todorov, Y. Zhu and D. B. Mitzi, Adv. Energy Mater., 2013, 4, 1301465.
2. A. Chirila, P. Reinhard, F. Pianezzi, P. Bloesch, A. R. Uhl, C. Fella, L. Kranz, D. Keller, C. Gretener, H. Hagendorfer, D. Jaeger, R. Erni, S. Nishiwaki, S. Buecheler and A. N. Tiwari, Nat. Mater., 2013, 12, 1107-1111.
3. P. Jackson, D. Hariskos, E. Lotter, S. Paetel, R. Wuerz, R. Menner, W. Wischmann and M. Powalla, Prog. Photovoltaic, 2011, 19, 894-987. 4.
4. U. Rau and J. H. Werner, Appl. Phys. Lett., 2004, 84, 3735-3737.
5. A. Walsh, S. Chen, S.-H. Wei and X.-G. Gong, Adv. Energy Mater., 2012, 2, 400-409.
6. M. J. Romero, H. Du, G. Teeter, Y. F. Yan and M. M. Al-Jassim, Phys. Rev. B, 2011, 84, 5.
7. J. Li, D. B. Mitzi and V. B. Shenoy, Acs Nano, 2011, 5, 8613-8619.
8. T. Gokmen, O. Gunawan, T. K. Todorov and D. B. Mitzi, Appl. Phys. Lett., 2013, 103, 103506.
9. J. Hedstrom, H. Ohlsen, M. Bodegard, A. Kylner, L. Stolt, D. Hariskos, M. Ruckh and H. Schock, Proceedings of the 23th IEEE PVSC, 1993, 364-371.
10. B. M. Basol, V. K. Kapur, C. R. Leidholm, A. Minnick, A. Halani and Ieee, Proceedings of the 24th IEEE PVSC, 1994, 148-151.
11. D. Cahen and R. Noufi, Appl. Phys. Lett., 1989, 54, 558-560.
12. M. A. Contreras, B. Egaas, P. Dippo, J. Webb, J. Granata, K. Ramanathan, S. Asher, A. Swartzlander, R. Noufi and Ieee, Proceedings of the 26th IEEE PVSC, 1997, 359-362.
13. D. W. Niles, K. Ramanathan, F. Hasoon, R. Noufi, B. J. Tielsch and J. E. Fulghum, J. Vac. Sci. Technol. A, 1997, 15, 3044-3049.
14. T. Nakada, D. Iga, H. Ohbo and A. Kunioka, Jpn. J. Appl. Phys. Part 1, 1997, 36, 732-737.15.
15. L. Kronik, D. Cahen and H. W. Schock, Adv. Mater., 1998, 10, 31.
16. L. Kronik, U. Rau, J.-F. Guillemoles, D. Braunger, H.-W. Schock and D. Cahen, Thin Solid Films, 2000, 361–362, 353-359.
17. M. Igalson, A. Kubiaczyk, P. Zabierowski, M. Bodegard and K. Granath, Thin Solid Films, 2001, 387, 225-227.
18. S. H. Wei, S. B. Zhang and A. Zunger, J. Appl. Phys.,1999, 85, 7214-7218.
19. C. S. Jiang, R. Noufi, K. Ramanathan, J. A. AbuShama, H. R. Moutinho and M. M. Al-Jassim, Appl. Phys. Lett., 2004, 85, 2625-2627.
20. P. T. Erslev, J. W. Lee, W. N. Shafarman and J. D. Cohen, Thin Solid Films, 2009, 517, 2277-2281.
21. D. Braunger, D. Hariskos, G. Bilger, U. Rau and H. W. Schock, Thin Solid Films, 2000, 361, 161-166.
22. Y. Yan, C. S. Jiang, R. Noufi, S.-H. Wei, H. R. Moutinho and M. M. Al-Jassim, Phys. Rev. Lett., 2007, 99.
23. G. Hanna, T. Glatzel, S. Sadewasser, N. Ott, H. P. Strunk, U. Rau and J. H. Werner, Appl. Phys. A, 2006, 82, 1-7.
24. R. Haight, X. Shao, W. Wang and D. B. Mitzi, Appl. Phys. Lett., 2014, 104.
25. A. Nagaoka, H. Miyake, T. Taniyama, K. Kakimoto, Y. Nose, M. A. Scarpulla and K. Yoshino, Appl. Phys. Lett., 2014, 104.

26. T. Gershon, B. Shin, N. Bojarczuk, M. Hopstaken, D. B. Mitzi and S. Guha, Adv. Energy Mater., 2015, 5.
27. J. B. Li, V. Chawla and B. M. Clemens, Adv. Mater., 2012, 24, 720.
28. W.-J. Yin, Y. Wu, S.-H. Wei, R. Noufi, M. M. Al-Jassim and Y. Yan, Advanced Energy Materials, 2014, 4, n/a-n/a.
29. S. Chen, A. Walsh, X.-G. Gong and S.-H. Wei, Adv. Mater., 2013, 25, 1522-1539.
30. H. Xin, J. K. Katahara, I. L. Braly and H. W. Hillhouse, Adv. Energy Mater., 2014, 4.
31. T. K. Todorov, J. Tang, S. Bag, O. Gunawan, T. Gokmen, Y. Zhu and D. B. Mitzi, Adv. Energy Mater., 2013, Vol. 3, 34-38.
32. Q. Guo, G. M. Ford, W. C. Yang, B. C. Walker, E. A. Stach, H. W. Hillhouse and R. Agrawal, J. Amer. Chem. Soc., 2010, 132, 17384-17386.
33. K. E. Roelofs, Q. J. Guo, S. Subramoney and J. V. Caspar, J. Mater. Chem. A, 2014, 2, 13464-13470.
34. J. W. Lekse, B. M. Leverett, C. H. Lake and J. A. Aitken, J. Solid State Chem., 2008, 181, 3217-3222.
35. W. Ki and H. W. Hillhouse, Adv. Energy Mater., 2011, 1, 732-735.
36. L. S. C. Pingree, O. G. Reid and D. S. Ginger, Adv. Mater., 2009, 21, 19-28.
37. C. Groves, O. G. Reid and D. S. Ginger, Acc. Chem. Res., 2010, 43, 612-620.
38. S. S. Hegedus and W. N. Shafarman, Prog. Photovoltaics, 2004, 12, 155-176.
39. J. J. Scragg, J. T. Wätjen, M. Edoff, T. Ericson, T. Kubart and C. Platzer-Björkman, J. Amer. Chem. Soc., 2012.
40. http://chemister.ru/Database/properties-en.php?dbid=1&id=614.
41. P. T. Cunningh, S. A. Johnson and E. J. Cairns, J. Electrochem. Soc., 1971, 118, 1941-1944.
42. http://chemspider.com/Chemical-Structure.74834.html.
43. G. Y. Kim, J. R. Kim, W. Jo, D. H. Son, D. H. Kim and J. K. Kang, Nanoscale Res. Lett., 2014, 9.
44. C. S. Jiang, R. Noufi, J. A. AbuShama, K. Ramanathan, H. R. Moutinho, J. Pankow and M. M. Al-Jassim, Appl. Phys. Lett., 2004, 84, 3477-3479.
45. S. Sadewasser, D. Abou-Ras, D. Azulay, R. Baier, I. Balberg, D. Cahen, S. Cohen, K. Gartsman, K. Ganesan, J. Kavalakkatt, W. Li, O. Millo, T. Rissom, Y. Rosenwaks, H. W. Schock, A. Schwarzman and T. Unold, Thin Solid Films, 2011, 519, 7341-7346.
46. J. T. Heath, J. D. Cohen and W. N. Shafarman, J. Appl. Phys., 2004, 95, 1000-1010.

Chapter 3. LOCAL HETEROGENETIES AND DEGRADATION OF HYBRID PEROVSKITES

3.1 CORRELATING LOCAL CHEMICAL HETEROGENEITIES WITH PHOTOLUMINESCENCE IN HYBRID PEROVSKITES*

*Adapted from "Impact of Microstructure on Local Carrier Lifetime in Perovskite Solar Cells"

Authors: Dane W. deQuilettes, Sarah Vorpahl, Samuel D. Stranks, Hirokazu Nagaoka, Giles Eperon, Mark E. Ziffer, Henry Snaith, David S. Ginger

3.1.1 *Introduction*

Perovskites have emerged as one of the most promising new photovoltaic materials with efficiencies reaching over 20%, on par with existing, commercially available technologies[43-47]. These materials shown incredible optoelectronic properties, such as micron scale diffusion lengths[48], long carrier lifetimes[49], and high open circuit voltage[50]. However, there remains many open questions in the field concerning issues such as stability, defect chemistry and hysteresis in the solar cell current-voltage curves.

As active layers in solar cells, organic-inorganic perovskites[51] combine the promise of solution processing[53, 54] with the ability to tailor the band gap through chemical substitution,[52-57] yielding solar cell power conversion efficiencies as high as 20.1%58. In addition to their remarkable photovoltaic performance, perovskites also exhibit high fractions of radiative recombination, with apparent carrier lifetimes of 250 ns or longer[59,60], and are challenging the idea that solution-processed semiconductors inevitably possess high densities of performance-limiting defects.

Ensuring that all recombination is radiative is critical for approaching the thermodynamic efficiency limits for solar cells and other optoelectronic devices.[61]

3.1.2 *Results and Discussion*

In the article, "Impact of microstructure on local carrier lifetime in perovskite solar cells," (*Science*, 2015) we examine carrier recombination lifetimes measured by photoluminescence (PL), which is commonly taken as a hallmark of perovskite film quality with longer decay lifetimes used as indicators of better-performing materials.[59,60,62-64] Carrier recombination kinetics have been described as a combination of trap-assisted, monomolecular (first-order), and bimolecular (second-order) recombination.[55] Although most studies agree that radiative bimolecular recombination dominates at high initial carrier densities ($n_0 > 10^{17}$ cm^{-3})[65-68], reports of kinetics at lower excitation densities (and relevant to solar cell operation)[69] range from single-exponential[62,70], to biexponential[63.64], to stretched-exponential[56,59] functions with varying levels of fidelity. These distributions have in turn been explained in terms of unintentional doping[71] or charge trapping.[72] The perovskite growth conditions[53,54,60] and post-deposition treatments[62,73] can greatly alter film morphology, carrier lifetime, and device performance, yet the underlying relations between these parameters are important open questions. For instance, perovskite films grown from nonstoichiometric mixed halide (Cl/I) precursor solutions have exhibited lifetimes of hundreds of nanoseconds, but PL lifetimes in films grown from chloride-free precursors are generally much shorter.[59,70]

We correlate confocal PL and SEM to study structure/function relationships in perovskite films. We found substantial local PL heterogeneity even for $CH_3NH_3PbI_3$(Cl) films with average lifetimes of ~1 μs (comparable to the longest lifetimes reported) [59,60] which suggests that

considerable scope remains for reducing non-radiative recombination in these films. In addition to observing entire grains that appear dark, we also observed that grain boundaries are associated with PL quenching, indicating that they are not as benign as has been suggested previously[73,74]. We further used PL microscopy to show that post-deposition chemical treatments can activate previously dark regions in the film, and we correlated local EDS with confocal fluorescence maps, finding that brighter grains with longer lifetimes were associated with local spikes in Cl concentration.

Figure 1a shows an overlaid SEM/PL microscopy image of a $CH_3NH_3PbI_3(Cl)$ film on glass. We tracked the changes in PL intensity with Cl content (Fig. 1b) and showed that bright regions correlate with areas of higher relative Cl content (Cl/Cl+I). Although films prepared from Cl/I mixed halide precursors stoichiometrically resemble triiodides, there is evidence for residual Cl at levels of ~2 weight % or less. The lifetime enhancement in the presence of Cl is consistent with recent findings that Cl-rich nucleation sites lead to better crystal coalescence and helps explain why films grown in the presence of Cl have slower recombination rates. We hypothesize that Cl could be present at the surface or within the crystals, interstitially or substitutionally, or simply at the substrate surface as a residual but unincorporated component left over from the seeding of low-defect crystallites.

[New References starting here]

Finally, we explored the role of Cl in perovskite films by comparing SEM EDS elemental composition traces with local PL intensity traces. Figure 4A shows an overlaid SEM/PL microscopy image of a $CH_3NH_3PbI_3(Cl)$ film on glass. We tracked the changes in PL intensity with Cl content (Fig. 4B) and showed that bright regions correlate with areas of higher relative Cl

content (Cl/Cl+I) (trace Cl in $CH_3NH_3PbI_3$ control films, Fig. S11) (*19*). Although films prepared from Cl/I mixed halide precursors stoichiometrically resemble triiodides (*38*), there is evidence for residual Cl at levels of ~2 wt% or less (*13, 39*). The lifetime enhancement in the presence of Cl is consistent with recent findings that Cl-rich nucleation sites lead to better crystal coalescence (*40, 41*) and helps explain why films grown in the presence of Cl have slower recombination rates (*9, 17*). We hypothesize that the Cl could be present at the surface or within the crystals, interstitially or substitutionally, or simply at the substrate surface as a residual but unincorporated component leftover from the seeding of low-defect crystallites. We performed time-of-flight secondary ion mass spectrometry (Fig. S11F) (*19*), and found higher Cl content in the $CH_3NH_3PbI_3$(Cl) films compared to $CH_3NH_3PbI_3$ films without Cl. This data probes the top 2 nm of the film.

3.1.3 *Conclusion*

Although perovskite solar cells have better radiative efficiencies than many technologies such as dye-sensitized solar cells, organic solar cells, or even CdTe, they still suffer from greater non-radiative losses than inorganic materials such as GaAs, and are only at present approaching CIGS (*31*). Our results identify a subpopulation of dark grains and grain boundaries as specific targets for perovskite growth and passivation studies, and show that local fluorescence lifetime imaging provides a route by which changes in film processing can be evaluated to assess their influence on carrier recombination in films. By removing these non-radiative pathways to obtain uniform brightness with high emissivity across all grains, it is likely that we will see the performance of perovskite devices approach the thermodynamic limits for solar cells and other light-emitting devices.

3.1.4 *Acknowledgements*

This material is based in part upon work supported by the State of Washington through the University of Washington Clean Energy Institute. DWD acknowledges support from a National Science Foundation Graduate Research Fellowship (DGE-1256082). SMV acknowledges support from a National Defense Science and Engineering Graduate Fellowship. The research leading to these results has received funding from the European Union Seventh Framework Program [FP7/2007-2013] under Grant Agreement No. 604032 of the MESO project. GE is supported by the EPSRC and Oxford Photovoltaics Ltd. through a Nanotechnology KTN CASE award. The authors gratefully acknowledge funding from the National Institute for Biomedical Imaging and Bioengineering (NIH grant EB-002027) supporting NESAC/BIO and ToF-SIMS instrumentation. D.W.D thanks Ian Braly, David Moerman, and Brigit Miller for valuable assistance. S.M.V. gratefully acknowledges Dan Graham for assistance with ToF-SIMS. Additional data, including materials, methods, and key controls are available online as Supplementary Material (19).

3.1.5 *Figures*

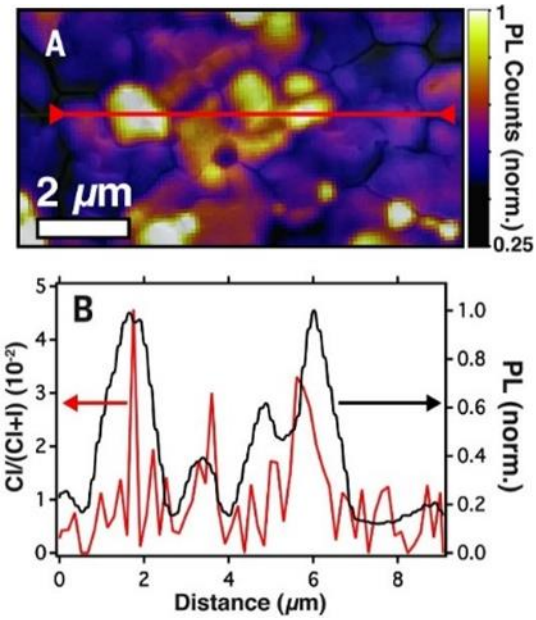

Figure 13 SEM micrograph overlaid on fluorescence image and EDS line scan showing that the local elemental weight ratio of Cl/(Cl+I) tracks areas of higher integrated PL intensity, indicating that Cl is associated with better-performing grains.

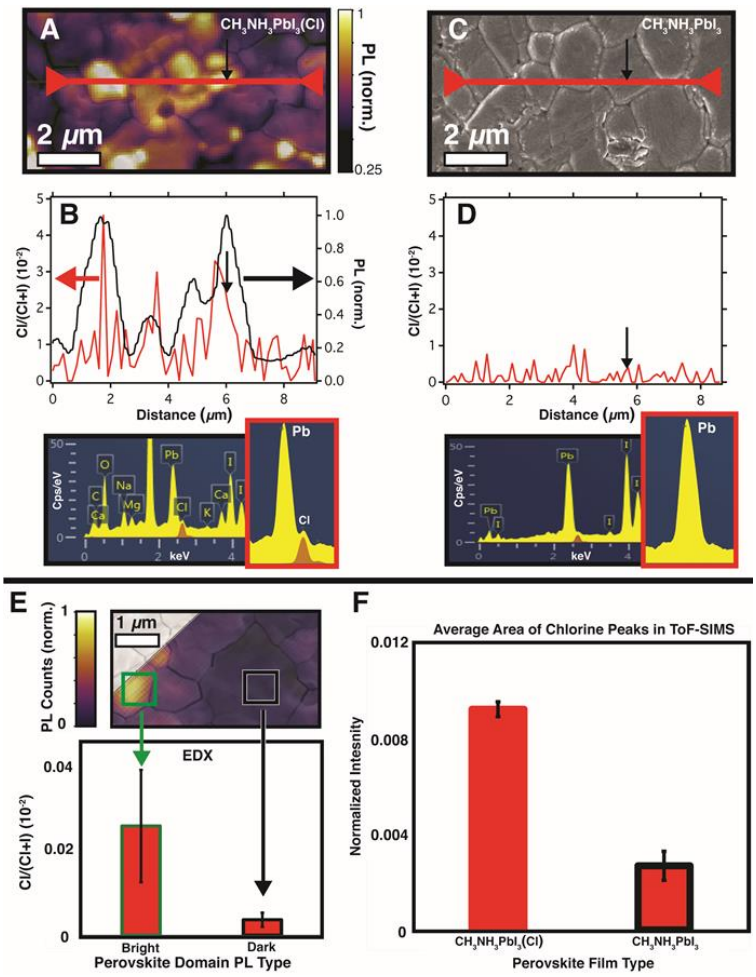

Figure 14 SEM and EDX of of CH3NH3PbI3(Cl) film

(A) SEM micrograph overlaid on fluorescence image of $CH_3NH_3PbI_3(Cl)$ film and (**B, top)** EDS linescan showing the local elemental weight ratio of Cl/(Cl+I) tracks areas of higher integrated photoluminescence intensity indicating that Cl is associated with the better performing grains. (**B, bottom**) Point spectra of area indicated by black arrow in (**B)**, showing detectable Cl. **(C)** SEM micrograph of $CH_3NH_3PbI_3$ film and (**D, top**) EDS linescan showing the local elemental weight ratio of Cl/(Cl+I) is within the baseline noise of the technique for films without intentional Cl. (**D, bottom**) Point spectra of area indicated by black arrow in (**D)**, showing no detectable concentration of Cl. **(E, top)** SEM micrograph overlaid on fluorescence image of $CH_3NH_3PbI_3(Cl)$ film and **(E, bottom)** EDX statistical analysis of point spectra collected in the bright domain (green square, Cl/(Cl+I) = 0.026 ± 0.013, N=4) versus the dark domain (black square, Cl/(Cl+I) = 0.004 ± 0.002, N=12). (**F)** ToF-SIMS data collected from 100 μm x 100 μm areas for two types of perovskite thin films on glass, $CH_3NH_3PbI_3(Cl)$ (red outline, Cl^- average intensity = 0.0092 ± 0.0003, N=6) and $CH_3NH_3PbI_3$ (black outline, Cl^- average intensity = 0.0027 ± 0.0006, N=5). In both samples, the Cl^- peak was normalized to the total counts. The ToF-SIMs sampling volume is confined to the top ~2 nm of the surface under the imaging conditions used, suggesting that Cl is present at least in the top layer.

3.1.6 *References*

43. Kojima, A.; Teshima, K.; Shirai, Y.; Miyasaka, T. J. Am. Chem. Soc. 2009, 131, 6050–6051,
44. Lee, M. M.; Teuscher, J.; Miyasaka, T.; Murakami, T. N.; Snaith, H. J. Science 2012, 338, 643– 6473.
45. Tan, Z. K.; Moghaddam, R. S.; Lai, M. L. Docampo, P.; Higler, R.; Deschler, F.; Price, M. Sadhanala, A. Pazos, L. M.; Nat. Nanotechnol. 2014, 9, 687– 692
46. Deschler, F.; Price, M.; Pathak, S.; Klintberg, L. E.; Jarausch, D.-D. Higler, R. Hüttner, S. Leijtens, T. Stranks, S. D.; Snaith, H. J. J. Phys. Chem. Lett. 2014, 5, 1421– 1426
47. Schmidt, L. C.; Pertegas, A.; Gonzalez-Carrero, S.; Malinkiewicz, O.; Agouram, S.; Minguez Espallargas,G.; Bolink, H. J.; Galian, R. E.; Perez-Prieto, J. J. Am. Chem. Soc. 2014, 136, 850–853
48. Li, y., Yan, W., Li, Y., Wang, S., Wang, w., Bian, Z., Xiao, L., Gong, Q. Scientific Reports 2015, 5, 14485
49. Wehrenfenning, C., Eperon, G., Johnston, M., Snaith, H., Herz, L. Adv. Mater. 2014, 26, 1584–1589
50. Yuchuan, S., Yuan, Y., Huang, J., Nature Energy 2016, 1, 15001
51. T. C. Sum, N. Mathews, Energ. Environ. Sci. 2014 7, 2518–2534
52. M. A. Green, A. Ho-Baillie, H. J. Snaith, Nat. Photonics 2014 8, 506–514
53. J. Burschka, N. Pellet, S. J. Moon, R. Humphry-Baker, P. Gao, M. K. Nazeeruddin, M. Grätzel, Nature 2013 499, 316–319
54. G. E. Eperon, V. M. Burlakov, P. Docampo, A. Goriely, H. J. Snaith, Adv. Funct. Mater. 2014 24, 151–157
55. G. Xing, N. Mathews, S. S. Lim, N. Yantara, X. Liu, D. Sabba, M. Grätzel, S. Mhaisalkar, T. C. Sum, Nat. Mater. 2014 13, 476–480
56. G. E. Eperon, S. D. Stranks, C. Menelaou, M. B. Johnston, L. M. Herz, H. J. Snaith, Energ. Environ. Sci. 2014 7, 982–988
57. J. H. Noh, S. H. Im, J. H. Heo, T. N. Mandal, S. I. Seok, Nano Lett 2013. 13, 1764–1769
58. S. D. Stranks, G. E. Eperon, G. Grancini, C. Menelaou, M. J. Alcocer, T. Leijtens, L. M. Herz, A. Petrozza, H. J. Snaith, Science 2013 342, 341–344
59. H. Zhou, Q. Chen, G. Li, S. Luo, T. B. Song, H. S. Duan, Z. Hong, J. You, Y. Liu, Y. Yang, Science 345, 542–546 (2014).
60. O. D. Miller, E. Yablonovitch, S. R. Kurtz, IEEE J. Photovolt 2012. 2, 303–311
61. N. K. Noel, A. Abate, S. D. Stranks, E. S. Parrott, V. M. Burlakov, A. Goriely, H. J. Snaith, ACS Nano, 2014 8, 9815–9821
62. J. You, Z. Hong, Y. M. Yang, Q. Chen, M. Cai, T. B. Song, C. C. Chen, S. Lu, Y. Liu, H. Zhou, Y. Yang, ACS Nano, 2014, 8, 1674–1680
63. P. W. Liang, C. Y. Liao, C. C. Chueh, F. Zuo, S. T. Williams, X. K. Xin, J. Lin, A. K. Jen, Adv. Mater. 2014, 26, 3748–3754
64. S. D. Stranks, V. M. Burlakov, T. Leijtens, J. M. Ball, A. Goriely, H. J. Snaith, Phys. Rev. Appl .2014 2, 034007
65. F. Deschler, M. Price, S. Pathak, L. E. Klintberg, D.-D. Jarausch, R. Higler, S. Hüttner, T. Leijtens, S. D. Stranks, H. J. Snaith, M. Atatüre, R. T. Phillips, R. H. Friend, J. Phys. Chem. Lett. 2014, 5, 1421–1426

66. C. Wehrenfennig, M. Liu, H. J. Snaith, M. B. Johnston, L. M. Herz, Energ. Environ. Sci.2014, 7, 2269–2275
67. J. S. Manser, P. V. Kamat, Nat. Photonics 2014 8, 737–743
68. G. Xing, N. Mathews, S. Sun, S. S. Lim, Y. M. Lam, M. Grätzel, S. Mhaisalkar, T. C. Sum, Science 2013, 342, 344–347
69. Y. Yamada, T. Nakamura, M. Endo, A. Wakamiya, Y. Kanemitsu, J. Am. Chem. Soc. 2014 136, 11610–11613
70. M. Saba, M. Cadelano, D. Marongiu, F. Chen, V. Sarritzu, N. Sestu, C. Figus, M. Aresti, R. Piras, A. G. Lehmann, C. Cannas, A. Musinu, F. Quochi, A. Mura, G. Bongiovanni, Nat. Commun. 2014 5, 5049
71 A. Abate, M. Saliba, D. J. Hollman, S. D. Stranks, K. Wojciechowski, R. Avolio, G. Grancini, A. Petrozza, H. J. Snaith, Nano Lett. 2014 14, 3247–3254
72. S. Watanabe, A. Punge, G. Hollopeter, K. I. Willig, R. J. Hobson, M. W. Davis, S. W. Hell, E. M. Jorgensen, Nat. Methods 8, 80–84 (2011)
73. E. Edri, S. Kirmayer, A. Henning, S. Mukhopadhyay, K. Gartsman, Y. Rosenwaks, G. Hodes, D. Cahen, Nano Lett 2014. 14, 1000–1004
74. W. J. Yin, T. Shi, Y. Yan, Adv. Mater 2014. 26, 4653–4658
75. Zhang, W., Pathak, S., Sakai, N., Stergiopoulos, T., Nayak, P., Noel, N., Haghighirad, A., Burlakov, V., deQuilettes, D., Sadhanala, A., Li, W., Liduo, W., Ginger, D., Friend, R., Snaith, H. Nature Commun. 2015, 6, 10030

3.2 Photodecomposition and Morphology Evolution of Organometal Halide Perovskite Solar Cells

Authors: Sarah M. Vorpahl , Fukashi Matsumoto, Jannel Q. Banks, Esha Sengupta, and David S. Ginger

3.2.1 *Overview*

We study the photoinduced degradation of hybrid organometal perovskite photovoltaics under illumination and ambient atmosphere using UV-vis absorption, atomic force microscopy, and device performance. We correlate the structural changes in the surface of the perovskite film with changes in the optical and electronic properties of the devices. The photodecomposition of the methylammonium lead triiodide perovskite layer itself proceeds much more slowly than the photodegradation of the performance of devices with fullerene/bathocuproine/aluminum top contacts, indicating that the active layer is more stable than the interface with the electrodes in this geometry. The evolution of the perovskite active layer performance proceeded through several phases: (1) an initial improvement in device characteristics, (2) a plateau with very slow degradation and finally (3) a catastrophic decline in material performance accompanied by marked changes in film morphology. The rapid increase in surface roughness of the active perovskite semiconductor associated with sudden failure also correlates with decreased absorption at the perovskite band edge and growth of a lead iodide absorption feature. We find that degradation requires both light and moisture, is accelerated at increased humidity, and scales linearly with light intensity, depending primarily on total photon dose.

3.2.2 *Introduction*

Organometal halide perovskites have re-emerged as a promising material for light-harvesting and light-emitting technologies.[1-5] Intense research is being undertaken in the hopes of commercializing solar cells within the next decade[6] and rapid improvement in solar cell efficiencies[7-11] are being reported. However, exploration of device stability and degradation of the materials has been less studied[12] compared to research on device engineering[13-14] and device physics.[15-19]

Nevertheless, the importance of stability is widely recognized,[12] and several studies have examined the stability of perovskite solar cells in humid air using a variety of conditions and device structures.[20-24] For instance, Yang et al. found that the identity of the hole transport layer has a dramatic effect on the degradation of triiodide perovskite films using *in situ* UV-vis measurements, with 2,2',7,7'-tetrakis-(N,N-di-4-methoxyphenylamino)-9,9'-spirobifluorene (Spiro-OMeTAD) and poly[bis(4-phenyl)(2,4,6-trimethylphenyl)amine] (PTAA) causing more rapid degradation than poly(3-hexylthiophene-2,5-diyl) (P3HT).[25] Misra et al. reported that encapsulated triiodide films degraded more quickly when exposed to elevated temperatures (~50 °C) thus concluding that degradation is thermally activated,[26] while Frost et al. have proposed that, in theory, small Lewis bases such as water, should contribute to an acid base reaction leading to irreversible decomposition of the perovskite to PbI_2.[27]

Here, we characterize the evolution of organometal halide perovskite semiconductor layers exposed to controlled photon doses using UV-vis absorption spectroscopy, atomic force microscopy (AFM), and device measurements. We correlate optical properties with morphology using AFM for *in situ* characterization of material property evolution during degradation. We find that the perovskite material itself is much more stable under exposure to light and humidity than a

device is after ([6,6]-phenyl-C_{61}-butyric acid methyl ester (PCBM)/bathocuproine (BCP)/Al layers have been added. The changes in the bare perovskite layer proceeds in three main steps. First a small increase in device performance characteristics is seen, followed by a period of little to no degradation. Finally, there is a sudden inflection point towards an exponential, and irreversible, decay in performance. Notably, we find that changes in film morphology correlate with these steps in the process of degradation: the films become suddenly rougher at the same point the performance begins decreasing rapidly. Using correlated characterization techniques we relate the stability of the perovskite material to its performance in a completed device.

3.2.3 *Results and Discussion*

We fabricated $CH_3NH_3PbI_3$ perovskite films utilizing a solvent engineering technique as introduced by Jeon et al.[28] Briefly, we made films by spin coating from a mixed solvent of γ-butyrolactone (GBA) and dimethylsulfoxide (DMSO) followed by toluene dripping, on poly(3,4-ethylenedioxythiophene):poly(4-styrenesulfonate) (PEDOT:PSS)-coated indium tin oxide (ITO) substrates, which produced uniform and semi-transparent films. We studied the photochemical decomposition of these films on both PEDOT:PSS/ITO without top contacts, and completed devices with top contacts PCBM/BCP/Al (see Figure 1A for device structure) by exposing them to 100 mW/cm^2 illumination from a white LED in air at room temperature (~25 °C) and 40% relative humidity. We controlled humidity using a home-built humidity controllable container (Figure S1). After degrading the perovskite films on PEDOT:PSS/ITO we incorporated these partially damaged layers into completed devices of the same structure (ITO/PEDOT:PSS/$CH_3NH_3PbI_3$/PCBM/BCP/Al). We then measured the device performance of

both sets of films (those perovskite films degraded before and after incorporation into a device active layer).

Figure 1B-E shows how the solar cell performance parameters, including short circuit current (J_{SC}), open circuit voltage (V_{OC}), fill factor (FF), and power conversion efficiency (PCE) evolve upon illumination for fixed exposure doses of light ranging from 0 to 3800 J/cm^2. The values are plotted as a function of photon dose for both pre-degraded devices (i.e. devices made from degraded films, black line) and post-degraded devices (i.e. made from fresh films and then degraded in the device geometry at V_{OC}, red line). A full list of device parameters is included in Supporting Information (Table S1). The PCE, FF, V_{OC} and J_{SC} for devices made from pre-degraded films were generally stable out to ~3000 J/cm^2 then decayed rapidly. Interestingly, there was a slight increase in J_{SC}, FF and V_{OC} up through ~1500 J/cm^2. Post-degraded devices had a much shorter period of stability. PCE and FF for these devices decayed rapidly after minimal photon dose. We found that bare perovskite material was much more stable before adding finishing contacts, with the amount of dose to a 50% loss in PCE being 450 J/cm^2 for the post-degraded device and 3300 J/cm^2 for the pre-degraded device (over 7× more photon dose). We thus conclude that the more rapid decline of the completed device is due to more rapid damage of the PCBM/BCP/Al contact than the perovskite or PEDOT:PSS contact. Although reports have shown that PCBM can be beneficial in passivating surface defect states,[29] fullerene is also easily oxidized under operating conditions.[30] These results are consistent with the rapid degradation of Al contacts that has been studied in the OLED and OPV literature[31] and suggest that engineering interfacial layers and electrode materials, as well as careful encapsulation should bring similar benefits to perovskites as they have brought to OLEDs and OPVs. Importantly, we also note that the stability of the semiconductor active layer out to nearly 3000 J/cm^2 under illumination in an air environment

compares favorably to similar studies of the degradation of all-organic semiconductor active layers, which can show performance degradation at doses of ~400 J/cm^2.[32-36] These data further show the importance of material engineering of interfacial layers and electrodes to increase efficiencies and stability.[13,37]

Figure 2A shows the current density-voltage (J-V) curves of the pre-degraded devices, which were made from films degraded with 0, 1500, 3000, 3400, 3600 and 3800 J/cm^2 photon doses. Reverse scans (open circuit to short circuit, solid line) and forward scans (short circuit to open circuit, not shown) were taken for each device. We found that the deviation between the max power points of these curves taken in alternate directions (hysteresis)[38] increased with increasing photon dose (Figure S2), indicating that increased hysteresis correlates with more degraded perovskite films.[39-40]

Recent research has suggested that hysteresis is a result of the quality of the perovskite/electrode contact.[41] The increased hysteresis we observed with increased aging is consistent with this hypothesis, as well as with findings that suggest that these defect states can result from formation of PbI_2,[42] a known degradation product.[43-44]

Figure 2B shows EQE spectra of the same fresh and degraded devices. We observed a gradual decay in the EQE with increasing photon dose, with a dramatic change in spectral shape at 3800 J/cm^2. However, at the perovskite band edge (750 nm) we saw an initial enhancement of EQE (from 40% to 54%) up to a photon dose of 1500 J/cm^2, which tracks with the initial rise in device performance. After the initial increase in EQE, there was again a return to the level of the as-prepared film by ~3000 J/cm^2 and then a rapid decrease at higher photon doses. We saw a similar increase in the EQE for a device that was exposed to humid air (40% RH, r.t.) without light irradiation for a longer time (18 hours), and no enhancement of EQE for a device exposed to 1500

J/cm^2 photon dose under nitrogen atmosphere (Figure S3). These data suggest that a small amount of water vapor modifies the film, allowing for an initial boost in optical and electrical properties. However, Yang et al. reported enhanced performance in devices when fabricated under low humidity (~30%) conditions,[37, 45] revealing reduced carrier recombination loss in these devices, indicating there is a limitation to how much moisture may be beneficial to device performance.

In addition, the J_{SC} values measured under simulated AM1.5G light are systematically smaller, and show systematically increasing deviations at longer degradation times, from the J_{SC} values estimated by integrating the EQE curves taken at low intensity with the AM1.5G spectra. This discrepancy is commonly observed owing to the increased non-geminate recombination under the strong light intensity.[46-47] Since we observed larger discrepancies as the films became more degraded we speculate that the rate of trap-mediated non-geminate recombination is increasing with degradation,[48-49] a supposition that is also consistent with the increased hysteresis as described above.

Figure 3 shows UV-vis spectra and AFM micrographs of representative films taken at different exposures. We found that the absorption of the perovskite film at several wavelengths (including the band edge at 750 nm) decreased slowly at first (Figure 3A, B) with a sharp decrease at high doses (>3000 J/cm^2) correlating with the J-V curves and EQE. We also observed an increase in the peak at 500 nm starting at the lowest amount of photon dose, which we assign to the formation of PbI_2 during degradation.[50] The peak from a pure PbI_2 film is included for comparison (Figure 3A, black dotted trace). This assignment is consistent with the formation of PbI_2 crystals in degraded perovskite films as reported elsewhere[51-52] and has been confirmed by X-ray diffraction (XRD) measurements for films made from PbI_2 precursor by others.[53]

Figure 3B plots the normalized absorbance at various wavelengths as a function of photon dose, and the root-mean-square roughness values taken from AFM micrographs of each film. Like the device performance data in Figure 1, the UV-Vis data in Figure 3B show a slow gradual change, followed by a sudden decrease in absorbance at the perovskite band edge occurring at ~3000 J/cm^2 under these conditions. Interestingly, this drop in absorbance and PCE is accompanied by a sharp increase in surface roughness of the films. Figure 3C shows AFM images taken at various stages of degradation. The mean particle diameter of the crystals increased with increasing photon dose (Figure S4). We also confirmed the increase in roughness values by an *in situ* AFM measurement of a single perovskite film under humid air with light irradiation (Figure S5 in supporting information, a time-lapse movie is also available as a supporting material). We studied a number of different films, all of which followed the same degradation trajectory (Figure S6). We find that the initially slow decay followed by a sharp drop correlated between the UV-Vis, surface roughness, and device performance and suggests the optical properties are connected to the change in morphology as a function of photon dose. Like the device performance, the change in surface morphology was photoactivated: similar samples stored and imaged in humid air in the dark showed little structural change over the same time period (Figure S7).

To better understand the formation of PbI_2 and other degradation products, we estimated the molar percentage of the degradation products by fitting the absorption spectra of the degraded films as a superposition of neat $CH_3NH_3PbI_3$ and PbI_2 (black (a) and red (b) lines in Figure 4). We then computed a molar percentage of Pb species from the fitted thickness data (see Figure S6). We found that the PbI_2 component gradually increased as the photon dose increased, with a significant jump after 3000 J/cm^2. However, we note that after degradation began, the sum of $CH_3NH_3PbI_3$ and PbI_2 molar percentage no longer came to the 100% total of a fresh perovskite. We assigned

this missing fraction to the formation of other Pb compounds in addition to PbI_2, and we plot this additional species as "unknown" as the blue line (c) in Figure 4. Notably, the formation of unidentified degradation products (deviation of the spectrum from a superposition of $CH_3NH_3PbI_3$ and PbI_2) was more prominent at greater photon doses. These results indicate at large photon doses there is a drastic conversion of the perovskite that correlates with a large change in morphology and device parameters. Additionally, we showed that neither high doses of light irradiation under inert atmosphere nor exposure in humid air without light irradiation separately cause degradation of the perovskite absorption (green (d) and purple (e) lines respectively, Figure 4). Therefore, we concluded that both humid air *and* light are necessary components to activate the degradation of perovskite by this pathway.

To separate the contribution of the effects from humidity and light intensity, we plot the decay of the 750 nm peak signal (perovskite band edge) from UV-vis absorbance data. Figure 5 shows how the absorbance changes as a function of both humidity and irradiation. Figure 5A shows the humidity dependence at a constant light exposure of 100 mW/cm^2 light. Figure 5B shows the dependence of the perovskite peak under various light intensities in 40% RH air. We observed that there was a strong humidity dependence for the films but that the degradation of the perovskite layer depends on light intensity to a much lesser extent. It is well-known that hybrid perovskites are sensitive to humidity.[25] To better understand how adsorption kinetics relate to device performance, we fit the data in Figure 5 using the Elovich equation[54], which is often used to model chemisorption data, as an empirical fit for our data. Further information about the fitting can be found in supporting information (Figure S8). Using these fits we can speculate that the period of slow degradation prior to an irreversible decline in performance involves an adsorption reaction between perovskite and water vapor. While the exact mechanism of decomposition remains

unclear, the model successfully parameterizes the observed humidity dependence (Table S2) and quantifies the observation that the degradation occurs faster at higher humidities.

3.2.4 *Conclusion*

We studied the degradation of $CH_3NH_3PbI_3$ perovskite semiconductor layers as a function of controlled irradiation with visible light. We found that perovskite active layers on PEDOT:PSS are more stable against photodecomposition in humid air than are fully completed perovskite solar cells with PCBM/BCP/Al contacts in place, indicating that the stability of this device geometry is limited by the contacts and not the inherent stability of the perovskite active layer. Examining the perovskite film itself, we observed a multi-step degradation behavior as measured by device performance, UV-vis and film morphology evolution. We observed a small enhancement of the electronic properties up to 1500 J/cm^2 followed by little or no degradation until ~3000 J/cm^2, when we found a swift and irreversible decay in optical and electronic properties. In this later degradation stage, we observed a sudden drop in the UV-vis absorption at the perovskite band edge of 750 nm along with a decrease in PCE. We correlated these changes in material stability with a change in morphology from small to larger crystals and increase in the formation of PbI_2. We observed that the degradation of the perovskite film increased with increasing humidity, but found that degradation was linear in light intensity, depending primarily on total exposed photon dose. The multi-step degradation pathway we observed is suggestive of multiple processes occurring in the film (passivation, decomposition, and gross morphology changes) and indicates that detailed kinetic and mechanistic studies may lead to the engineering of more stable perovskite devices.

3.2.5 *Appendix C*

3.2.6 *Acknowledgements*

SMV acknowledges support from the Department of Defense (DoD) through the National Defense Science & Engineering Graduate Fellowship (NDSEG) Program. We also acknowledge support for the SPM imaging of perovskites through DOE BES grant DE-SC0013957.

3.2.7 *Figures*

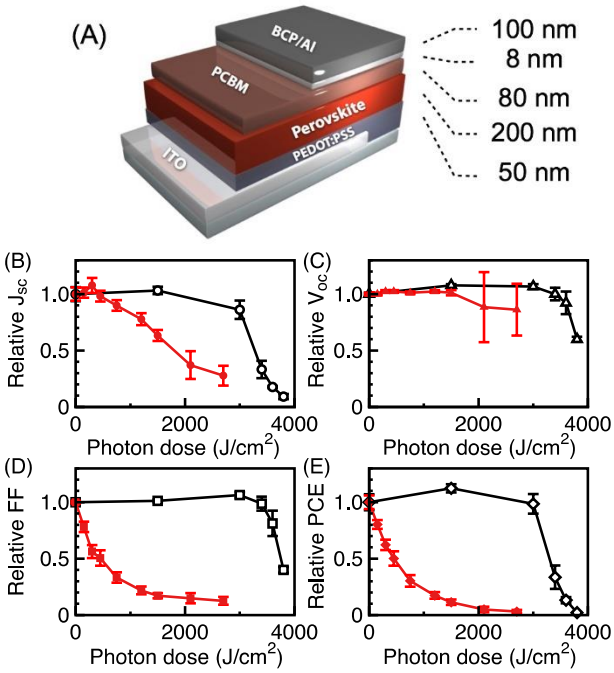

Figure 15 Schematic of device structure and JV characteristics for $CH_3NH_3PbI_3$ devices

(A) Schematic of device structure. Variation of normalized (at t=0) photovoltaic parameters of (B) J_{SC}, (C) V_{OC}, (D) FF, and (E) PCE for reverse scans of the devices completing PCBM/BCP/Al layers after degradation (black lines), for the devices completing PCBM/BCP/Al layers before degradation (red lines) as a function of photon dose. The data were averaged from 8 or 6 pixels as shown in Table S1. Error bars represent the standard deviation across the devices.

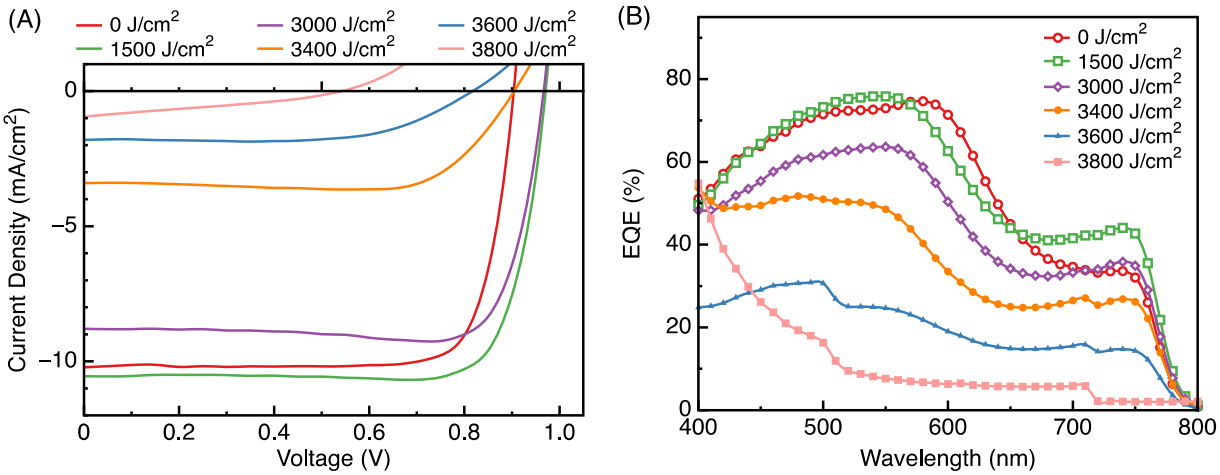

Figure 16 JV curves and EQE for CH3NH3PbI3 devices

(A) Current density-voltage curves measured under simulated AM1.5G solar illumination at 100 mW/cm^2 intensity for ITO/PEDOT:PSS/$CH_3NH_3PbI_3$/PCBM/BCP/Al devices fabricated from degraded films at various photon doses. Curves were obtained by reverse scan (open circuit to short circuit). (B) External quantum efficiency spectra of devices fabricated from degraded $CH_3NH_3PbI_3$ films. The curves and spectra were averaged from 8 pixels for 3000 J/cm^2 and below, 6 pixels for the rest.

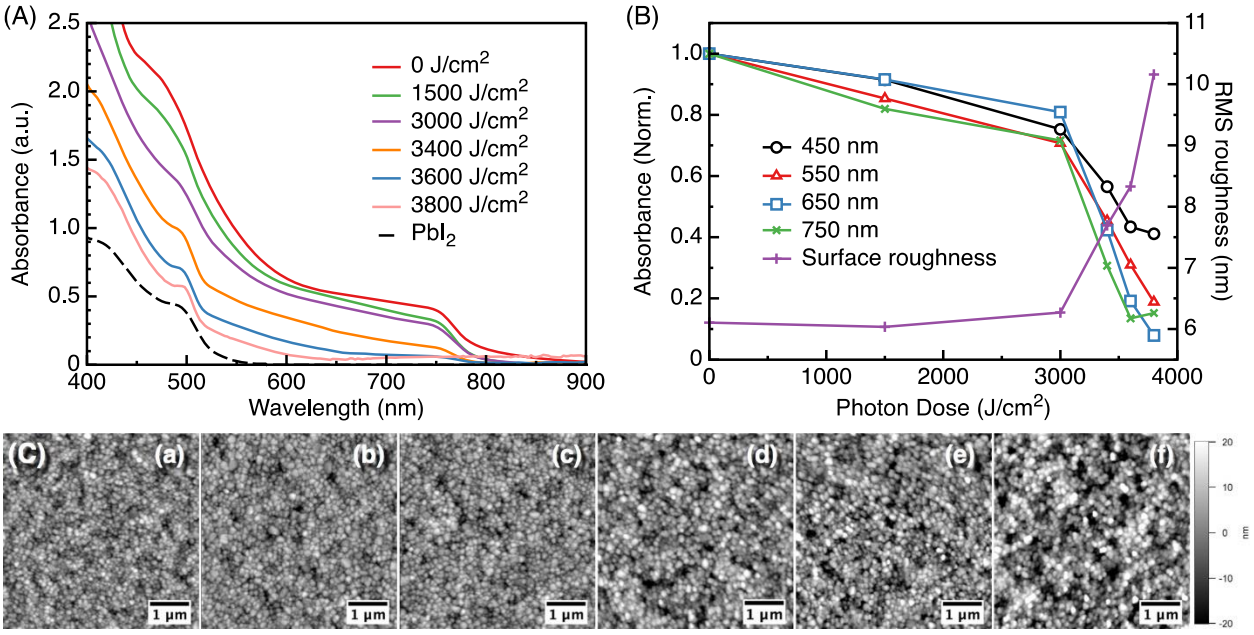

Figure 17 UV-vis and AFM topography images for CH3NH3PbI3 films.

UV-vis absorption spectra of individual $CH_3NH_3PbI_3$ films degraded under 100 mW/cm^2 irradiation at various photon doses (r.t., 40% humidity), and a PbI_2 film. (B) Plots for absorbances at various wavelengths and root-mean-square roughness obtained from (C) AFM topology images (5 × 5 μm) of $CH_3NH_3PbI_3$ films at (a) 0 J/cm^2 (b) 1500 J/cm^2 (c) 3000 J/cm^2 (d) 3400 J/cm^2 (e) 3600 J/cm^2 (f) 3800 J/cm^2 photon irradiation. The absorbance values were normalized by the pristine absorbance of each film.

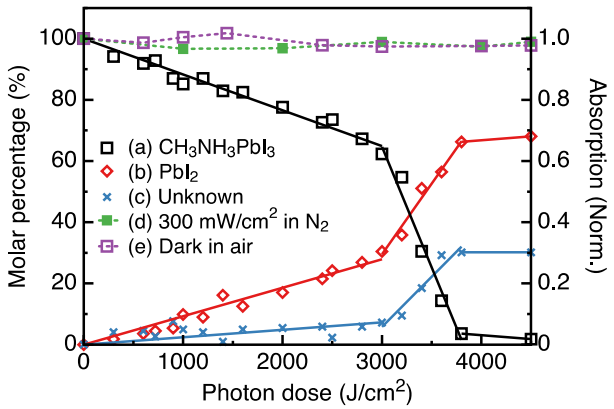

Figure 18 Plots for molar percentage (left axis) of CH3NH3PbI3, PbI2, and unknown materials as a function of photon dose

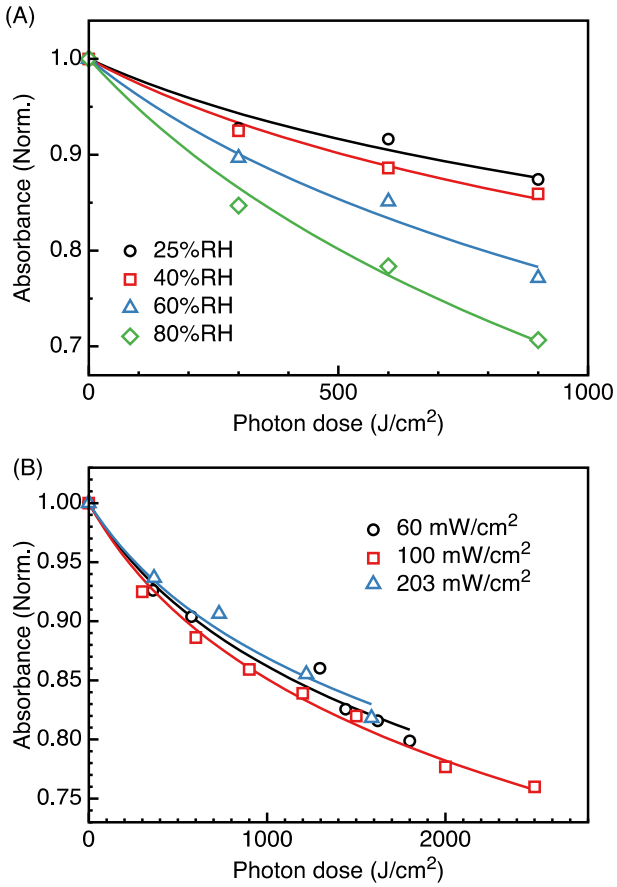

Figure 19 Humidity and photon dose dependence of CH3NH3PbI3 films

(A) Humidity dependence of absorbance at 750 nm of $CH_3NH_3PbI_3$ films under 100 mW/cm^2 light exposure in air, (B) degradation of absorbance at 750 nm of $CH_3NH_3PbI_3$ films with 60, 100, and 203 mW/cm^2 light intensity in 40%RH air as a function of photon dose. Lines are fits to the modified Elovich equation[51] to guide the eye.

3.2.8 *References*

References

(1) Kojima, A.; Teshima, K.; Shirai, Y.; Miyasaka, T. Organometal Halide Perovskites as Visible-Light Sensitizers for Photovoltaic Cells. J. Am. Chem. Soc. 2009, 131, 6050-6051.
(2) Lee, M. M.; Teuscher, J.; Miyasaka, T.; Murakami, T. N.; Snaith, H. J. Efficient Hybrid Solar Cells Based on Meso-Superstructured Organometal Halide Perovskites. Science 2012, 338, 643-647.
(3) Tan, Z. K.; Moghaddam, R. S.; Lai, M. L.; Docampo, P.; Higler, R.; Deschler, F.; Price, M.; Sadhanala, A.; Pazos, L. M.; Credgington, D., et al. Bright Light-Emitting Diodes Based on Organometal Halide Perovskite. Nat. Nanotechnol. 2014, 9, 687-692.
(4) Deschler, F.; Price, M.; Pathak, S.; Klintberg, L. E.; Jarausch, D.-D.; Higler, R.; Hüttner, S.; Leijtens, T.; Stranks, S. D.; Snaith, H. J., et al. High Photoluminescence Efficiency and Optically Pumped Lasing in Solution-Processed Mixed Halide Perovskite Semiconductors. J. Phys. Chem. Lett. 2014, 5, 1421-1426.
(5) Schmidt, L. C.; Pertegas, A.; Gonzalez-Carrero, S.; Malinkiewicz, O.; Agouram, S.; Minguez Espallargas, G.; Bolink, H. J.; Galian, R. E.; Perez-Prieto, J. Nontemplate Synthesis of CH3NH3PbBr3 Perovskite Nanoparticles. J. Am. Chem. Soc. 2014, 136, 850-853.
(6) Carnie, M. J.; Charbonneau, C.; Davies, M. L.; Troughton, J.; Watson, T. M.; Wojciechowski, K.; Snaith, H.; Worsley, D. A. A One-Step Low Temperature Processing Route for Organolead Halide Perovskite Solar Cells. Chem. Commun. 2013, 49, 7893-7895.
(7) Xiao, Z.; Bi, C.; Shao, Y.; Dong, Q.; Wang, Q.; Yuan, Y.; Wang, C.; Gao, Y.; Huang, J. Efficient, High Yield Perovskite Photovoltaic Devices Grown by Interdiffusion of Solution-Processed Precursor Stacking Layers. Energy Environ. Sci. 2014, 7, 2619-2623.
(8) Im, J. H.; Jang, I. H.; Pellet, N.; Gratzel, M.; Park, N. G. Growth of CH3NH3PbI3 Cuboids with Controlled Size for High-Efficiency Perovskite Solar Cells. Nat. Nanotechnol. 2014, 9, 927-932.
(9) Nie, W.; Tsai, H.; Asadpour, R.; Blancon, J.-C.; Neukirch, A. J.; Gupta, G.; Crochet, J. J.; Chhowalla, M.; Tretiak, S.; Alam, M. A., et al. High-Efficiency Solution-Processed Perovskite Solar Cells with Millimeter-Scale Grains. Science 2015, 347, 522-525.
(10) Wang, F.; Yu, H.; Xu, H.; Zhao, N. HPbI3: A New Precursor Compound for Highly Efficient Solution-Processed Perovskite Solar Cells. Adv. Funct. Mater. 2015, 25, 1120-1126.
(11) Jeon, N. J.; Noh, J. H.; Yang, W. S.; Kim, Y. C.; Ryu, S.; Seo, J.; Seok, S. I. Compositional Engineering of Perovskite Materials for High-Performance Solar Cells. Nature 2015, 517, 476-480.
(12) Niu, G.; Guo, X.; Wang, L. Review of Recent Progress in Chemical Stability of Perovskite Solar Cells. J. Mater. Chem. A 2015, 3, 8970-8980.
(13) Abrusci, A.; Stranks, S. D.; Docampo, P.; Yip, H. L.; Jen, A. K.; Snaith, H. J. High-Performance Perovskite-Polymer Hybrid Solar Cells Via Electronic Coupling with Fullerene Monolayers. Nano Lett. 2013, 13, 3124-3128.
(14) Jeng, J.-Y.; Chiang, Y.-F.; Lee, M.-H.; Peng, S.-R.; Guo, T.-F.; Chen, P.; Wen, T.-C. CH3NH3PbI3 Perovskite/Fullerene Planar-Heterojunction Hybrid Solar Cells. Adv. Mater. 2013, 25, 3727-3732.

(15) Stranks, S. D.; Eperon, G. E.; Grancini, G.; Menelaou, C.; Alcocer, M. J. P.; Leijtens, T.; Herz, L. M.; Petrozza, A.; Snaith, H. J. Electron-Hole Diffusion Lengths Exceeding 1 Micrometer in an Organometal Trihalide Perovskite Absorber. Science 2013, 342, 341-344.
(16) Luo, S.; Daoud, W. A. Recent Progress in Organic–Inorganic Halide Perovskite Solar Cells: Mechanisms and Material Design. J. Mater. Chem. A 2015, 3, 8992-9010.
(17) Bretschneider, S. A.; Weickert, J.; Dorman, J. A.; Schmidt-Mende, L. Research Update: Physical and Electrical Characteristics of Lead Halide Perovskites for Solar Cell Applications. APL Materials 2014, 2, 040701.
(18) deQuilettes, D. W.; Vorpahl, S. M.; Stranks, S. D.; Nagaoka, H.; Eperon, G. E.; Ziffer, M. E.; Snaith, H. J.; Ginger, D. S. Impact of Microstructure on Local Carrier Lifetime in Perovskite Solar Cells. Science 2015, 348, 683-686.
(19) Nagaoka, H.; Ma, F.; deQuilettes, D. W.; Vorpahl, S. M.; Glaz, M. S.; Colbert, A. E.; Ziffer, M. E.; Ginger, D. S. Zr Incorporation into TiO2 Electrodes Reduces Hysteresis and Improves Performance in Hybrid Perovskite Solar Cells While Increasing Carrier Lifetimes. J. Phys. Chem. Lett. 2015, 6, 669-675.
(20) Liu, J.; Wu, Y.; Qin, C.; Yang, X.; Yasuda, T.; Islam, A.; Zhang, K.; Peng, W.; Chen, W.; Han, L. A Dopant-Free Hole-Transporting Material for Efficient and Stable Perovskite Solar Cells. Energy Environ. Sci. 2014, 7, 2963-2967.
(21) Kwon, Y. S.; Lim, J.; Yun, H.-J.; Kim, Y.-H.; Park, T. A Diketopyrrolopyrrole-Containing Hole Transporting Conjugated Polymer for Use in Efficient Stable Organic–Inorganic Hybrid Solar Cells Based on a Perovskite. Energy Environ. Sci. 2014, 7, 1454-1460.
(22) Hu, Q.; Wu, J.; Jiang, C.; Liu, T.; Que, X.; Zhu, R.; Gong, Q. Engineering of Electron-Selective Contact for Perovskite Solar Cells with Efficiency Exceeding 15%. ACS Nano 2014, 8, 10161-10167.
(23) Kim, J. H.; Liang, P.-W.; Williams, S. T.; Cho, N.; Chueh, C.-C.; Glaz, M. S.; Ginger, D. S.; Jen, A. K.-Y. High-Performance and Environmentally Stable Planar Heterojunction Perovskite Solar Cells Based on a Solution-Processed Copper-Doped Nickel Oxide Hole-Transporting Layer. Adv. Mater. 2015, 27, 695-701.
(24) Hawash, Z.; Ono, L. K.; Raga, S. R.; Lee, M. V.; Qi, Y. Air-Exposure Induced Dopant Redistribution and Energy Level Shifts in Spin-Coated Spiro-Meotad Films. Chem. Mater. 2015, 27, 562-569.
(25) Yang, J.; Siempelkamp, B. D.; Liu, D.; Kelly, T. L. Investigation of CH3NH3PbI3 Degradation Rates and Mechanisms in Controlled Humidity Environments Using in Situ Techniques. ACS Nano 2015, 9, 1955-1963.
(26) Misra, R. K.; Aharon, S.; Li, B.; Mogilyansky, D.; Visoly-Fisher, I.; Etgar, L.; Katz, E. A. Temperature- and Component-Dependent Degradation of Perovskite Photovoltaic Materials under Concentrated Sunlight. J. Phys. Chem. Lett. 2015, 6, 326-330.
(27) Frost, J. M.; Butler, K. T.; Brivio, F.; Hendon, C. H.; van Schilfgaarde, M.; Walsh, A. Atomistic Origins of High-Performance in Hybrid Halide Perovskite Solar Cells. Nano Lett. 2014, 14, 2584-2590.
(28) Jeon, N. J.; Noh, J. H.; Kim, Y. C.; Yang, W. S.; Ryu, S.; Seok, S. I. Solvent Engineering for High-Performance Inorganic-Organic Hybrid Perovskite Solar Cells. Nat. Mater. 2014, 13, 897-903.
(29) Shao, Y.; Xiao, Z.; Bi, C.; Yuan, Y.; Huang, J. Origin and Elimination of Photocurrent Hysteresis by Fullerene Passivation in CH3NH3PbI3 Planar Heterojunction Solar Cells. Nat. Commun. 2014, 5, 5784.

(30) Reese, M. O.; Nardes, A.; Rupert, B. Photoinduced Degradation of Polymer and Polymer–Fullerene Active Layers: Experiment and Theory. Adv. Funct. Mater. 2010, 20, 3476-3483.
(31) Jørgensen, M.; Norrman, K.; Krebs, F. C. Stability/Degradation of Polymer Solar Cells. Sol. Energ. Mat. Sol. Cells 2008, 92, 686-714.
(32) Cox, P. A.; Waldow, D. A.; Dupper, T. J.; Jesse, S.; Ginger, D. S. Mapping Nanoscale Variations in Photochemical Damage of Polymer/Fullerene Solar Cells with Dissipation Imaging. ACS Nano 2013, 7, 10405-10413.
(33) Galisteo-López, J. F.; Anaya, M.; Calvo, M. E.; Míguez, H. Environmental Effects on the Photophysics of Organic–Inorganic Halide Perovskites. J. Phys. Chem. Lett. 2015, 6, 2200-2205.
(34) Zhao, C.; Chen, B.; Qiao, X.; Luan, L.; Lu, K.; Hu, B. Revealing Underlying Processes Involved in Light Soaking Effects and Hysteresis Phenomena in Perovskite Solar Cells. Adv. Energy Mater. 2015. 5, DOI: 10.1002/aenm.201500279.
(35) Shao, G.; Rayermann, G. E.; Smith, E. M.; Ginger, D. S. Morphology-Dependent Trap Formation in Bulk Heterojunction Photodiodes. J. Phys. Chem. B 2013, 117, 4654-4660.
(36) Reid, O. G.; Rayermann, G. E.; Coffey, D. C.; Ginger, D. S. Imaging Local Trap Formation in Conjugated Polymer Solar Cells: A Comparison of Time-Resolved Electrostatic Force Microscopy and Scanning Kelvin Probe Imaging. J. Phys. Chem. C 2010, 114, 20672-20677.
(37) Zhou, H.; Chen, Q.; Li, G.; Luo, S.; Song, T.-b.; Duan, H.-S.; Hong, Z.; You, J.; Liu, Y.; Yang, Y. Interface Engineering of Highly Efficient Perovskite Solar Cells. Science 2014, 345, 542-546.
(38) Snaith, H. J.; Abate, A.; Ball, J. M.; Eperon, G. E.; Leijtens, T.; Noel, N. K.; Stranks, S. D.; Wang, J. T.-W.; Wojciechowski, K.; Zhang, W. Anomalous Hysteresis in Perovskite Solar Cells. J. Phys. Chem. Lett. 2014, 5, 1511-1515.
(39) Xie, F. X.; Zhang, D.; Su, H.; Ren, X.; Wong, K. S.; Grätzel, M.; Choy, W. C. H. Vacuum-Assisted Thermal Annealing of CH3NH3PbI3 for Highly Stable and Efficient Perovskite Solar Cells. ACS Nano 2015, 9, 639-646.
(40) Wei, J.; Zhao, Y.; Li, H.; Li, G.; Pan, J.; Xu, D.; Zhao, Q.; Yu, D. Hysteresis Analysis Based on the Ferroelectric Effect in Hybrid Perovskite Solar Cells. J. Phys. Chem. Lett. 2014, 5, 3937-3945.
(41) Zhang, Y.; Liu, M.; Eperon, G. E.; Leijtens, T. C.; McMeekin, D.; Saliba, M.; Zhang, W.; de Bastiani, M.; Petrozza, A.; Herz, L. M., et al. Charge Selective Contacts, Mobile Ions and Anomalous Hysteresis in Organic-Inorganic Perovskite Solar Cells. Mater. Horiz. 2015, 2, 315-322.
(42) Supasai, T.; Rujisamphan, N.; Ullrich, K.; Chemseddine, A.; Dittrich, T. Formation of a Passivating CH3NH3PbI3/PbI2 Interface During Moderate Heating of CH3NH3PbI3 Layers. Appl. Phys. Lett. 2013, 103, 183906.
(43) Christians, J. A.; Miranda Herrera, P. A.; Kamat, P. V. Transformation of the Excited State and Photovoltaic Efficiency of CH3NH3PbI3 Perovskite Upon Controlled Exposure to Humidified Air. J. Am. Chem. Soc. 2015, 137, 1530-1538.
(44) Niu, G.; Li, W.; Meng, F.; Wang, L.; Dong, H.; Qiu, Y. Study on the Stability of CH3NH3PbI3 Films and the Effect of Post-Modification by Aluminum Oxide in All-Solid-State Hybrid Solar Cells. J. Mater. Chem. A 2014, 2, 705-710.

(45) You, J.; Yang, Y. M.; Hong, Z.; Song, T.-B.; Meng, L.; Liu, Y.; Jiang, C.; Zhou, H.; Chang, W.-H.; Li, G., et al. Moisture Assisted Perovskite Film Growth for High Performance Solar Cells. Appl. Phys. Lett. 2014, 105, 183902.
(46) Mauer, R.; Howard, I. A.; Laquai, F. Effect of Nongeminate Recombination on Fill Factor in Polythiophene/Methanofullerene Organic Solar Cells. J. Phys. Chem. Lett. 2010, 1, 3500-3505.
(47) Dibb, G. F. A.; Jamieson, F. C.; Maurano, A.; Nelson, J.; Durrant, J. R. Limits on the Fill Factor in Organic Photovoltaics: Distinguishing Nongeminate and Geminate Recombination Mechanisms. J. Phys. Chem. Lett. 2013, 4, 803-808.
(48) Schäfer, S.; Petersen, A.; Wagner, T. A.; Kniprath, R.; Lingenfelser, D.; Zen, A.; Kirchartz, T.; Zimmermann, B.; Würfel, U.; Feng, X., et al. Influence of the Indium Tin Oxide/Organic Interface on Open-Circuit Voltage, Recombination, and Cell Degradation in Organic Small-Molecule Solar Cells. Phys. Rev. B 2011, 83, 165311.
(49) Heumueller, T.; Mateker, W. R.; Sachs-Quintana, I. T.; Vandewal, K.; Bartelt, J. A.; Burke, T. M.; Ameri, T.; Brabec, C. J.; McGehee, M. D. Reducing Burn-in Voltage Loss in Polymer Solar Cells by Increasing the Polymer Crystallinity. Energ. Environ. Sci. 2014, 7, 2974-2980.
(50) Ahuja, R.; Arwin, H.; da Silva, A. F.; Persson, C.; Osorio-Guillén, J. M.; Souzaa de Almeida, J.; Moyses Araujo, C.; Veje, E.; Veissid, N.; An, C. Y., et al. Electronic and Optical Properties of Lead Iodide. J. Appl. Phys. 2002, 92, 7219-7224.
(51) Ito, S.; Tanaka, S.; Manabe, K.; Nishino, H. Effects of Surface Blocking Layer of Sb2S3 on Nanocrystalline TiO2 for CH3NH3PbI3 perovskite Solar Cells. J. Phys. Chem. C 2014, 118, 16995-17000.
(52) Kim, J. H.; Williams, S. T.; Cho, N.; Chueh, C.-C.; Jen, A. K. Y. Enhanced Environmental Stability of Planar Heterojunction Perovskite Solar Cells Based on Blade-Coating. Adv. Energy Mater. 2015, 5, DOI: 10.1002/aenm.201401229.
(53) Zhang, W.; Saliba, M.; Moore, D. T.; Pathak, S. K.; Horantner, M. T.; Stergiopoulos, T.; Stranks, S. D.; Eperon, G. E.; Alexander-Webber, J. A.; Abate, A., et al. Ultrasmooth Organic-Inorganic Perovskite Thin-Film Formation and Crystallization for Efficient Planar Heterojunction Solar Cells. Nat. Commun. 2015, 6, 6142.
(54) Low, M. J. D. Kinetics of Chemisorption of Gases on Solids. Chem. Rev. 1960, 60, 267-312.

Chapter 4. INVESTIGATING FERROELECTRIC PROPERTIES OF METHYLAMMONIUM LEAD IODIDE PEROVSKITE FILMS

Authors: Sarah M. Vorpahl, Rajiv Giridharagopal, Giles E. Eperon, Ilka M. Hermes, Stefan A. L. Weber, David S. Ginger

4.1 DISAPPEARANCE OF FERROIC DOMAIN STRUCTURE UPON HEATING METHYLAMMONIUM LEAD TRIIODIDE PEROVSKITE FROM TETRAGONAL TO CUBIC PHASE

4.1.1 *Overview*

We study the ferroic properties of the archetypal semiconductor halide perovskite methylammonium lead triiodide ($CH_3NH_3PbI_3$ or MAPI) that is currently being investigated for use in thin film solar cells and light emitting diodes. We use piezoresponsive force microscopy (PFM) to image polycrystalline thin films. We find these films exhibit ferroic domains and these domains reversibly appear and disappear below and above the tetragonal-to-cubic phase transition temperature. Importantly, we observe these domains to exhibit a PFM signal that is predominantly in-plane for films with the (110) plane oriented parallel to the substrate, providing a measure of the polarization relative to the crystal orientation. We characterize the polarization and its temporal response using both local switching spectroscopy and time-dependent PFM spectra. These data show hysteresis loops with the polarization switching with bias, but relaxing back on time scales of several minutes. We propose that our results are consistent with the existence of ferroelectric

behavior due the off-centering of the Pb^{2+} cation, although the local polarization response is complicated by the presence of local ionic and electronic conductivity.

4.1.2 *Introduction*

Almost since the first reports of high efficiency photovoltaics based on methylammonium lead triiodide ($CH_3NH_3PbI_3$), the presence, and even importance, of ferroic order in these materials has been a topic of interest and even controversy.[1-11] Early work proposed that ferroelectric order could (favorably) help reduce carrier recombination,[3,4] or (unfavorably) lead to hysteresis in the current voltage (J-V) curves of devices with ferroelectric domains.[3,5,6] While initial studies failed to find evidence for ferroic order,[7] and the most current understanding attributes the J-V hysteresis primarily to ion motion,[8] other researchers have found evidence for ferroelastic domains using transmission electron microscopy,[9] photothermal induced resonance,[10] and piezoresponsive force microscopy.[11] Recently, Cahen and co-workers have argued that even bulk single crystals exhibit true ferroelectric domains.[2]

At present, the nature and origin of this ferroic order, even in the best-studied $CH_3NH_3PbI_3$ perovskite systems remains unclear. Although early studies suggested ferroic ordering of the dipolar methylammonium cation could occur,[12, 13] the relatively weak interactions, and rapid rotations of the methylammonium cation, [14,17] suggest such ordering may be unlikely. Even without dipolar ordering, it is possible that the chemical origin of polarized domain formation can arise from structural distortions of the inorganic lattice.[15]

To investigate these issues, we study perovskite films using piezoresponsive force microscopy (PFM).[16] We study both vertical and lateral PFM signatures and, importantly, measure PFM as we

heat a $CH_3NH_3PbI_3$ sample through the tetragonal to cubic phase transition that occurs around 55° C. Finally, we use local electrical switching and time-resolved polarization to investigate the dynamic nature of domain polarization.

4.1.3 *Results and Discussion*

We focus on probing the ferroic nature of polycrystalline $CH_3NH_3PbI_3$ samples deposited on compact titania.[17] Figure 1 shows our experimental schematic and images for both vertical and lateral PFM. Briefly, PFM is a scanning probe microscopy technique that scans a conductive tip in contact with the surface of a film to apply a bias and map the local piezoelectric response to this bias, tracking lattice deformation.[18] In particular, PFM exploits the high Q of the AFM cantilever at contact resonance to amplify the response, where the contact resonance mode is excited electrically via an AC voltage applied between the tip and the substrate.[19,20] In this work, we primarily employ dual amplitude resonance tracking (DART) for better decoupling of topography from piezoresponse.[21] In these PFM images, the average amplitude and phase response of the cantilever is due to the response of the material to the AC stimulus. In the idealized case, the PFM phase response will exhibit a 180° difference in phase response between oppositely oriented domains.[22] For vertical PFM (Figure 1a-d), the out-of-plane deformation of the sample is detected through the vertical bending motion of the tip. For lateral PFM (Figure 1e-h), in-plane vibrations from shear strain are detected in a similar manner using the torsional motion of the cantilever.[23,24] These changes in motion of the cantilever are detected using the vertical and horizontal position of a laser reflected off the cantilever onto a 4-part photodiode.

Figure 1b shows the AFM topography for a typical $CH_3NH_3PbI_3$ sample fabricated using a one-step deposition and post-processing solvent annealing. This annealing process has been previously

shown to increase crystallinity.[11] We see that grain sizes vary from 500-1100 nm and the samples have an RMS roughness of 24.1 ± 0.8 nm. Larger images of the films show distinct grain boundaries and minimal holes (Figure S1). Figure 1c shows the vertical amplitude response in PFM for the same area of film. The amplitude response in vertical PFM is a measure of the vertical surface displacement of the tip due to the AC bias. Fig. 1 shows well-ordered domains in almost every grain of our $CH_3NH_3PbI_3$ films. These images are consistent with recent reports of ferroeleastic domain structure, revealing domains with similar morphology. [9-11]

Figure 1d shows the out-of-plane phase response for the $CH_3NH_3PbI_3$ films. The phase is nearly constant across the entire image of Figure 1d. We see no out-of-plane phase signal, with the only deviations at the sharp crystal edges attributable to topographic crosstalk. One would expect that vertically oriented ferroelectric domains would show phase contrast of 180° as the film either expands or contracts in response to the applied field. The absence of such phase contrast implies the absence of vertically oriented domains. Therefore, we conclude that our maps, which over many samples show no vertical phase contrast, indicate that any spontaneous polarization is not out-of-plane in nature.

Previous studies have used vertical PFM and observed similar results, interpreting the apparent ferroic domain structure in the vertical amplitude signal as arising from cross-talk with an in-plane piezoresponse.[25] In order to explicitly test this hypothesis on our samples, we acquired lateral-mode PFM images on the same region of the sample where we had acquired vertical PFM images.

Figure 1f shows the topography from the exact same area as the vertical measurements. Figure 1g shows the resulting lateral mode PFM amplitude image, and Figure 1h the corresponding lateral mode PFM phase image. The lateral amplitude image in Figure 1g shows similar banding and

domain structure to the vertical image shown in Figure 1c. However, while the vertical PFM phase image in Figure 1d shows a nearly constant phase across the entire image, the lateral PFM phase image in Figure 1h reveals striking domains with nearly 180° (160°) offsets (see line scans, Figure S2). We conclude from this map that the spontaneous polarization lies parallel to the surface of the film.

Next, we use X-ray diffraction (XRD) to analyze any crystalline orientation in our films, and thus correlate the film structure with ferroic polarization. We find that our perovskite films are oriented with the (110) plane parallel to the surface of the film (Figure S3). Röhm et al. suggested that both a displacement of the Pb in the inorganic cage and organic cation rotation are the chemical origin of ferroelectricity,[26] and Rakita et al. concluded that a pyroelectric response arose in $CH_3NH_3PbI_3$ from contacts placed along the (110) plane due to the polar nature of $CH_3NH_3PbI_3$.[2] To investigate the link between structure and the chemical nature of ferroic domains, we characterize an all-inorganic perovskite, $CsPbI_3$. Figure S4 shows the same vertical and lateral PFM analysis for the Cs-based film as performed for the $CH_3NH_3PbI_3$ films. We find, that like the $CH_3NH_3PbI_3$ films, the $CsPbI_3$ shows no signal in the vertical phase maps but does show domain-like structure in the lateral phase maps. From these data, we conclude that the MA^+ cation is not necessary for ferroic domain ordering observed in PFM.

Having observed ferroic ordering in our samples, and having confirmed that the piezoresponsive axis lies in the plane of the sample when the (110) plane is parallel to the surface of our sample, we next turn to investigate the microscopic origins of the ferroic order in more detail. Perovskites in the tetragonal phase can exhibit ferroic response due to a loss of centrosymmetry.[27] Thus, one test to distinguish between the effects of ordering of A-site cations,[11] and alternative explanations like off-center distortion of the tetragonal phase,[28] is to probe the ferroic order in the sample as it

is heated through the tetragonal-to-cubic phase transition, which occurs around 55° C for $CH_3NH_3PbI_3$ films.

Because of the quality and ease of imaging with vertical PFM, we used the vertical PFM to follow changes in the ferroic domain structure as our samples were heated through the phase transition. Figure 2 shows the vertical PFM signals taken using DART mode PFM. Figure 2a shows the $CH_3NH_3PbI_3$ film in the dark, at 25° C under a nitrogen atmosphere. We again see the well-ordered domains. Using the environmental heating stage in our Cypher ES AFM, we slowly heat (0.2 °C/s) the sample to 65°C and reimage the film in the exact same area. We calibrate temperatures for the stage using a thermocouple at all temperatures between 0-70 °C. Figure 2b shows the amplitude signal at 65°C, which is past the tetragonal to cubic transition at ~55°C. Strikingly, above the tetragonal-to-cubic phase transition temperature, we see no evidence of ordered domains in the PFM image (see Figure S6 for further images, including images taken just above and just below the transition temperature).

We next lowered the temperature of the sample temperature back to 25° C at the same rate. Figure 2c shows PFM image of the sample after returning to 25° C, with domains reappearing in the same location as before heating. We observed similar behavior on many samples, with the domains reappearing at their original positions. To our knowledge, this is the first observation of the perovskite PFM signal changing at elevated temperature. Since the PFM signal disappears suddenly above the transition temperature, and reappears suddenly upon cooling (rather than gradually fading out and then back in) we conclude that the disappearance of the signal is associated with the passage of the sample through the tetragonal to cubic phase transition. Because of the importance of tetragonal symmetry in ferroelectric order, we conclude that the

disappearance of the domains imaged in PFM when passing into the centrosymmetric cubic phase is an observation consistent with the assignment of ferroelectric domains.

One of the defining characteristics of a ferroelectric material is the ability to switch between different metastable states with the application of an electric field.[16] As such, the hallmark of ferroelectric order in PFM imaging is the observation of hysteresis loops that retain their remnant polarization after removal of the applied bias, and that disappear when probed with electric fields higher than the coercive field.[22] However, despite several reports of vertical PFM signals in $CH_3NH_3PbI_3$ perovskite films prepared via different methods, the observation of clear hysteresis loops has remained challenging. [7,11, 26] Therefore, we next turn to explore the response of our PFM signals at a variety of time and voltage scales using piezoresponse switching spectroscopy.[20]

In switching spectroscopy, hysteresis loops plot the phase signal from PFM as a function of applied DC voltage being swept back and forth between positive and negative bias (See Figure S7 for more details). Similarly, butterfly loops plot the amplitude response from PFM as a function of the same back and forth applied DC bias. For a ferroelectric material both measurements reflect the bias-dependent nature of oriented dipoles with increasing bias. Figure 3 shows 2D maps and electrical switching loops from both lateral (Figure 3a-c) and vertical (Figure 3d-f) PFM. We start by looking at the lateral phase on a $CH_3NH_3PbI_3$ film (Figure 3a). Figure 3b and 3c show the representative hysteresis loop and butterfly curves from this sample, respectively. These measurements are taken between -5 and 5 volts DC bias and 0.05 second pulse width of 50% duty cycle (0.05 s on, 0.05 s off). We find that the hysteresis loops open barely 100°, while the butterfly curve in Figure 3c shows an asymmetric response for positive and negative bias. In a classic ferroelectric material, we would expect to see hysteresis loops

closer to 180° difference in phase and a symmetric response for both polarities in the butterfly curve. It is possible that friction forces between the tip and the surface may experimentally limit lateral electrical switching.[25] However, we also consider how other – non ferroelectric – dynamics in the system may contribute to the observed electrical switching response. We turn to vertical hysteresis to further probe the nature of polarization in our films.

Figure 3d shows the vertical phase map taken on the same area of $CH_3NH_3PbI_3$ film. We see no out-of-plane domains in this image and therefore would anticipate no electrical switching loops from vertical poling. Figure 3e and 3f show the hysteresis loop and butterfly curve obtained for this sample. Interestingly, we do see a very strong response for both measurements. Therefore, we consider the time constant of the phase change and ask whether the hysteresis seen in electrical switching is permanent on a longer time scale. We first analyze the frequency dependence of our hysteresis loops, which has been used to show that electrical switching comes from ionic motion in halide perovskite films.[8] Figure S7 shows that at slower frequencies of 0.05 Hz or lower, where the polarization may have a chance to decay in time, there is a slight closing of the hysteresis loop. We next look to even longer time scales to characterize the temporal nature of depolarization for switched domains. Figure S8 shows the phase before and after polarization with a +2.8 V applied DC bias (above the coercive bias). We find that after six minutes the phase flips back to its original state, showing that electrical switching is only semi-permanent. Taken together with the in-plane polarization we see in $CH_3NH_3PbI_3$, and the clear disappearance of PFM signal above the tetragonal-to-cubic transition, we propose that films are ferroelectric. However, we also suggest that local electrical switching is heavily influenced by ionic motion, given the transient behavior and frequency dependence of hysteresis loops. Figure S9 shows temperature-dependent hysteresis loops, taken between 0-68° C. Consistent with the image data, we observe that above the phase

transition the loops collapse and the hysteretic behavior disappears. These data help further support our proposal that while ionic motion may contribute to electrical switching response and depolarization, there is also a contribution from ferroelectric ordering.

4.1.4 *Conclusion*

In conclusion, we have studied the ferroic properties of $CH_3NH_3PbI_3$ perovskite using both vertical and lateral mode PFM, and as a function of temperature. We find that for films with the (110) plane oriented predominantly parallel to the film surface that the PFM signal is dominated by an in-plane response. Importantly, we observe that the domain structure in the PFM images disappears as the sample is heated above the tetragonal-to-cubic phase transition temperature, and that this structure reappears upon cooling. The transition to the cubic phase of $CH_3NH_3PbI_3$ perovskite could release strain within the lattice, consistent with earlier assignments of ferroelastic behavior.[9-11] However, ferroelastic behavior in the absence of ferroelectric polarization would not necessarily be expected to give rise to a PFM signal. We thus interpret our results as evidence for the role of the loss of symmetry in the tetragonal phase underpinning the ferroelectric order in the $CH_3NH_3PbI_3$ perovskite. In particular, we suggest that an off-center displacement of the Pb^{2+} due to a "ferroelectric distortion" of the PbI_6 octahedra could be consistent with our observations.[29] Future studies may find correlation of PFM response with local crystal orientation, as well as the PFM response from single crystals, useful in further illuminating this relationship. We obtain hysteresis and butterfly loops that, on the surface, also appear consistent with ferroelectric behavior. However, the remnant polarization disappears on timescales of minutes at room temperature, and furthermore the hysteresis loops do not close when the AC readout signal is larger than the DC bias (Figure S8), a sure sign that non-ferroelectric effects are also at play.[30] Given that the halide perovskites are both ionic and

electronic conductors, we propose that our data are consistent with $CH_3NH_3PbI_3$ being a ferroelectric perovskite due to structural distortions of the tetragonal lattice; however, the characterization of hysteresis loop dynamics in this situation is complicated by both the electronic and ionic conductivity of the sample, as has recently been proposed from bulk measurements by Cahen and co-workers.[8]

4.1.5 *Appendix D*

4.1.6 *Acknowledgements*

We thank Professor Jiangyu Li for helpful discussions. We thank Liam Bradshaw for help with XRD. This Letter is based primarily on work supported by the DOE (DE-SC0013957). We acknowledge additional support from the Alvin L. and Verla R. Kwiram Endowment from the Department of Chemistry at the University of Washington. Part of this work was conducted at the Molecular Analysis Facility, a National Nanotechnology Coordinated Infrastructure site at the University of Washington, which is supported in part by the National Science Foundation (Grant ECC-1542101), the University of Washington, the Molecular Engineering & Sciences Institute, the Clean Energy Institute, and the National Institutes of Health.

4.1.7 *Figures*

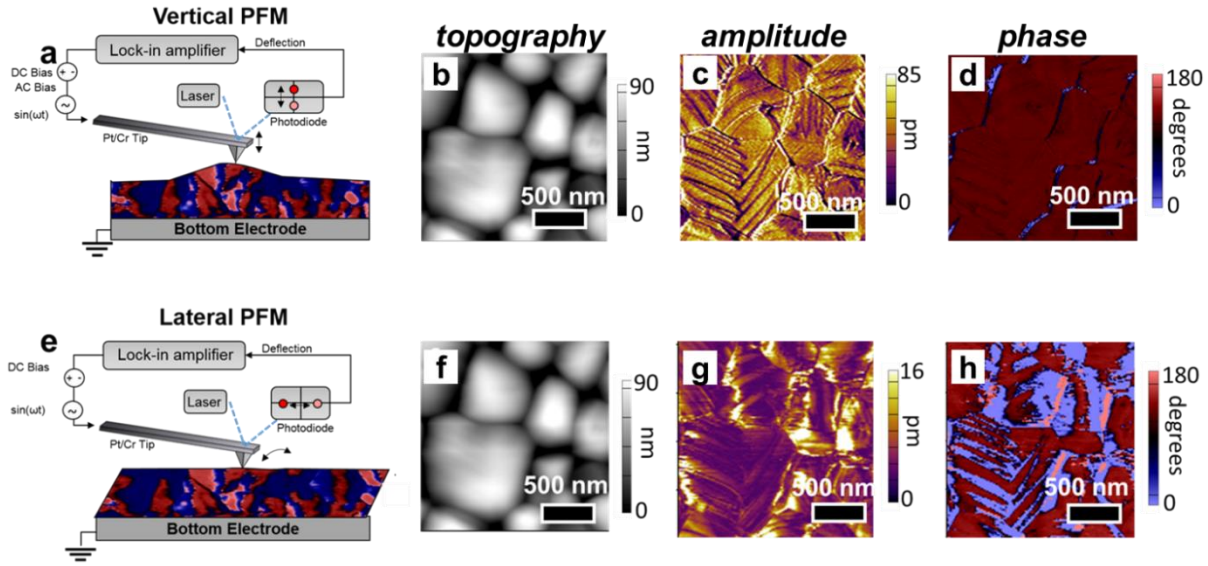

Figure 20 Piezoresponse force microscopy (PFM) schematic and data

a) experimental set up for vertical PFM. Micrographs from PFM including b) topography, c) out of plane (DART-mode) amplitude d) out of plane phase; e) experimental schematic for lateral PFM, f) topography, g) lateral amplitude and h) lateral phase taken on the same 3x3 um^2 location of solvent annealed $CH_3NH3PbI_3$films on titania.

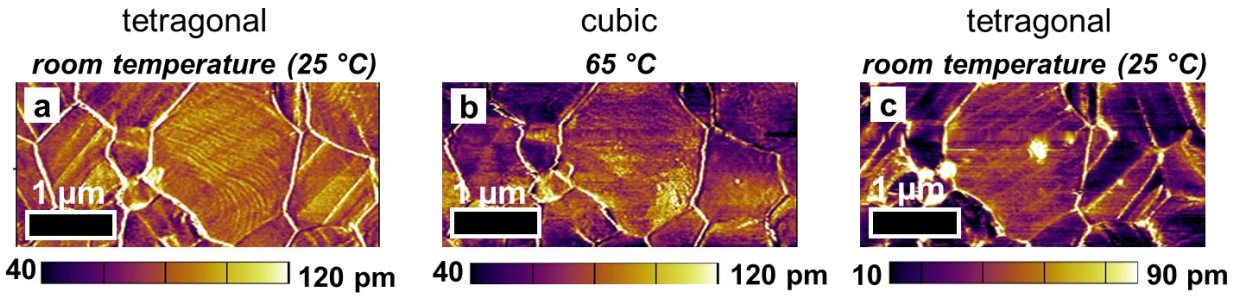

Figure 21 Temperature dependence of out-of-plane PFM (DART-mode) amplitude images for same area of solvent annealed CH3NH3PbI3 film

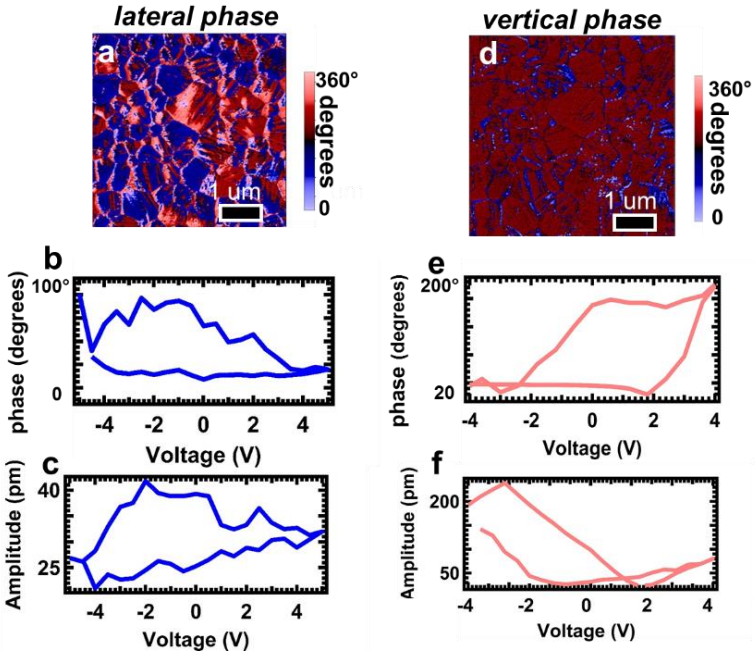

Figure 22Phase maps and electrical switching loops on solvent annealed CH3NH3PbI3 films from DART mode PFM.

a) lateral phase b) lateral hysteresis loop and c) lateral butterfly curve; d) vertical phase, e) vertical hysteresis loop and f) vertical butterfly curve.

4.1.8 *References*

1. Sewvandi, G. A.; Kodera, K.; Ma, H.; Nakanishi, S.; Feng, Q., Antiferroelectric Nature of CH3NH3PbI3− xClx Perovskite and Its Implication for Charge Separation in Perovskite Solar Cells. *Scientific reports* **2016,** *6*, 30680.
2. Rakita, Y.; Bar-Elli, O.; Meirzadeh, E.; Kaslasi, H.; Peleg, Y.; Hodes, G.; Lubomirsky, I.; Oron, D.; Ehre, D.; Cahen, D., Tetragonal CH3NH3PbI3 is ferroelectric. *Proceedings of the National Academy of Sciences* **2017**, 201702429.
3. Frost, J.; Butler, K.; Brivio, F.; Hendon, C.; van Schilfgaarde, M.; Walsh, A., Atomistic origins of high-performance in hybrid halide perovskite solar cells. *Condensed-Matter Material-Science* **2014**.
4. Liu, S.; Zheng, F.; Koocher, N. Z.; Takenaka, H.; Wang, F.; Rappe, A. M., Ferroelectric Domain Wall Induced Band Gap Reduction and Charge Separation in Organometal Halide Perovskites. *The Journal of Physical Chemistry Letters* **2015,** *6* (4), 693-699.
5. Frost, J. M.; Butler, K. T.; Walsh, A., Molecular ferroelectric contributions to anomalous hysteresis in hybrid perovskite solar cells. *Apl Materials* **2014,** *2* (8).
6. Wei, J.; Zhao, Y.; Li, H.; Li, G.; Pan, J.; Xu, D.; Zhao, Q.; Yu, D., Hysteresis analysis based on the ferroelectric effect in hybrid perovskite solar cells. *The journal of physical chemistry letters* **2014,** *5* (21), 3937-3945.
7. Fan, Z.; Xiao, J.; Sun, K.; Chen, L.; Hu, Y.; Ouyang, J.; Ong, K. P.; Zeng, K.; Wang, J., Ferroelectricity of CH3NH3PbI3 perovskite. *The journal of physical chemistry letters* **2015,** *6* (7), 1155-1161.
8. Beilsten-Edmands, J.; Eperon, G.; Johnson, R.; Snaith, H.; Radaelli, P., Non-ferroelectric nature of the conductance hysteresis in CH3NH3PbI3 perovskite-based photovoltaic devices. *Applied Physics Letters* **2015,** *106* (17), 173502.
9. Rothmann, M. U.; Li, W.; Zhu, Y.; Bach, U.; Spiccia, L.; Etheridge, J.; Cheng, Y.-B., Direct observation of intrinsic twin domains in tetragonal CH(3)NH(3)PbI(3). *Nature Communications* **2017,** *8*, 14547.
10. Strelcov, E.; Dong, Q.; Li, T.; Chae, J.; Shao, Y.; Deng, Y.; Gruverman, A.; Huang, J.; Centrone, A., CH 3 NH 3 PbI 3 perovskites: Ferroelasticity revealed. *Science Advances* **2017,** *3* (4), e1602165.
11. Hermes, I. M.; Bretschneider, S. A.; Bergmann, V. W.; Li, D.; Klasen, A.; Mars, J.; Tremel, W.; Laquai, F.; Butt, H.-J.; Mezger, M., Ferroelastic fingerprints in methylammonium lead iodide perovskite. **2016**.
12. Leguy, A. M. A.; Frost, J. M.; McMahon, A. P.; Sakai, V. G.; Kochelmann, W.; Law, C.; Li, X.; Foglia, F.; Walsh, A.; O'Regan, B. C.; Nelson, J.; Cabral, J. T.; Barnes, P. R. F., The dynamics of methylammonium ions in hybrid organic–inorganic perovskite solar cells. *Nature Communications* **2015,** *6*, 7124.
13. Motta, C.; El-Mellouhi, F.; Kais, S.; Tabet, N.; Alharbi, F.; Sanvito, S., Revealing the role of organic cations in hybrid halide perovskite CH3NH3PbI3. *Nature communications* **2015,** *6*, 7026.
14. Bakulin, A. A.; Selig, O.; Bakker, H. J.; Rezus, Y. L. A.; Müller, C.; Glaser, T.; Lovrincic, R.; Sun, Z.; Chen, Z.; Walsh, A.; Frost, J. M.; Jansen, T. L. C., Real-Time Observation of Organic Cation Reorientation in Methylammonium Lead Iodide Perovskites. *The Journal of Physical Chemistry Letters* **2015,** *6* (18), 3663-3669.

15. Brivio, F.; Frost, J. M.; Skelton, J. M.; Jackson, A. J.; Weber, O. J.; Weller, M. T.; Goñi, A. R.; Leguy, A. M. A.; Barnes, P. R. F.; Walsh, A., Lattice dynamics and vibrational spectra of the orthorhombic, tetragonal, and cubic phases of methylammonium lead iodide. *Physical Review B* **2015,** *92* (14), 144308.
16. Gruverman, A.; Kalinin, S. V., Piezoresponse force microscopy and recent advances in nanoscale studies of ferroelectrics. *Journal of Materials Science* **2006,** *41* (1), 107-116.
17. Xiao, Z.; Dong, Q.; Bi, C.; Shao, Y.; Yuan, Y.; Huang, J., Solvent annealing of perovskite-induced crystal growth for photovoltaic-device efficiency enhancement. *Advanced Materials* **2014,** *26* (37), 6503-6509.
18. Kalinin, S. V.; Bonnell, D. A., Imaging mechanism of piezoresponse force microscopy of ferroelectric surfaces. *Physical Review B* **2002,** *65* (12), 125408.
19. Okino, H.; Sakamoto, J.; Yamamoto, T., Contact-Resonance Piezoresponse Force Microscope and Its Application to Domain Observation of Pb (Mg1/3Nb2/3) O3–PbTiO3 Single Crystals. *Japanese journal of applied physics* **2003,** *42* (9S), 6209.
20. Jesse, S.; Mirman, B.; Kalinin, S. V., Resonance enhancement in piezoresponse force microscopy: Mapping electromechanical activity, contact stiffness, and Q factor. *Applied physics letters* **2006,** *89* (2), 022906.
21. Rodriguez, B. J.; Callahan, C.; Kalinin, S. V.; Proksch, R., Dual-frequency resonance-tracking atomic force microscopy. *Nanotechnology* **2007,** *18* (47), 475504.
22. Kalinin, S. V.; Morozovska, A. N.; Chen, L. Q.; Rodriguez, B. J., Local polarization dynamics in ferroelectric materials. *Reports on Progress in Physics* **2010,** *73* (5), 056502.
23. Peter, F.; Rüdiger, A.; Waser, R.; Szot, K.; Reichenberg, B., Contributions to in-plane piezoresponse on axially symmetrical samples. *Review of Scientific Instruments* **2005,** *76* (10), 106108.
24. Roelofs, A.; Böttger, U.; Waser, R.; Schlaphof, F.; Trogisch, S.; Eng, L. M., Differentiating 180° and 90° switching of ferroelectric domains with three-dimensional piezoresponse force microscopy. *Applied Physics Letters* **2000,** *77* (21), 3444-3446.
25. Peter, F.; Rüdiger, A.; Waser, R., Mechanical crosstalk between vertical and lateral piezoresponse force microscopy. *Review of Scientific Instruments* **2006,** *77* (3), 036103.
26. Röhm, H.; Leonhard, T.; Hoffmann, M. J.; Colsmann, A., Ferroelectric domains in methylammonium lead iodide perovskite thin-films. *Energy & Environmental Science* **2017,** *10* (4), 950-955.
27. Howard, C. J.; Stokes, H. T., Group-theoretical analysis of octahedral tilting in perovskites. *Acta Crystallographica Section B: Structural Science* **1998,** *54* (6), 782-789.
28. Rothmann, M. U.; Li, W.; Zhu, Y.; Bach, U.; Spiccia, L.; Etheridge, J.; Cheng, Y.-B., Direct observation of intrinsic twin domains in tetragonal CH3NH3PbI3. *Nature Communications* **2017,** *8*.
29. Stoumpos, C. C.; Malliakas, C. D.; Kanatzidis, M. G., Semiconducting tin and lead iodide perovskites with organic cations: Phase transitions, high mobilities, and near-infrared photoluminescent properties. *Inorganic Chemistry* **2013,** *52* (15), 9019-9038.
30. Vasudevan, R. K.; Balke, N.; Maksymovych, P.; Jesse, S.; Kalinin, S. V., Ferroelectric or non-ferroelectric: Why so many materials exhibit “ferroelectricity” on the nanoscale. *Applied Physics Reviews* **2017,** *4* (2), 021302.

Chapter 5. POLICY TOOLS FOR RENEWABLE ENERGY INNOVATION AND COMMERCIALIZATION

"To truly transform our economy, protect our security, and save our planet from the ravages of climate change, we need to ultimately make clean, renewable energy the profitable kind of energy." -Barack Obama, Address to Joint Session of Congress, Feb. 24, 2009

5.1.1 *Introduction*

The year 2008 marked a transformative moment in U.S. energy production. For the first time in history more renewable energy capacity was created than that of conventional energy. This moment delineated an important transition from the dirty energy of the past to the clean energy of the future. This trend has continued today, with 13.44% of domestically produced electricity in the U.S. coming from renewables in 2015[1]. The success of renewable energy deployment is owed in large part to a combination of research and development (R&D) funds for innovation and public policy and visionary political leadership. Technical expertise alone is not enough to change our energy behavior brute force. Government intervention is necessary to help mediate the financial dangers of developing and adopting emerging renewable energy technology, which still face both technical and economic barriers. The International Energy Agency (IEA) has mirrored this sentiment by stating as one of its imperative actions that "governments must develop policy frameworks that encourage private sector investment in lower-carbon energy options". [2]

Inherent in this idea is the notion that government intervention is correcting a failure of the energy market. These market failures exist on several levels. One example are the market failures that have arisen from our dependence on (foreign and domestic) oil, and other polluting energy such as coal. Not only is the true cost of non-renewable energy not captured in the cost (outside of a

carbon market) but the additional benefits of long term availability of natural resources is not currently captured in the cost of renewables as well. Additionally, the International Solar Energy Society explains that the "historical incentives for the conventional energy resources continue even today to bias markets by burying many of the real societal costs of their use."[3] The additional historic and political advantages of oil and coal are too numerous to parse out here (for an incredible investigation of this topic check out Daniel Yergin's definitive analysis in his Pulitzer prize winning bestseller *The Prize: The Epic Quest for Oil, Money and Power*). Second, government intervention is necessary to protect and incentivize those companies that act as early adapters for emerging renewable energy innovations. Again, due to the lack of certainty in the market for these technologies, companies should have some sort of protection from pure market forces with regards to being a costumer for technology that benefits the whole planet. The same protections should go to technical innovators who use their expertise to solve scientific problems with far reaching benefits. Addressing these market failures clearly points to the centrality of R&D as an element in stimulating growth of renewable energy deployment.

Commercialization of technology is a complicated nexus of R&D, market needs (supply and demand side) and other non-market factors such as political climate. Many questions arise as to the potential impact of government interventions in the energy industry. For example, how can government tools help cut down time horizons for the commercialization of emerging renewable energy technology? How can policy tools be designed to help move a new technology from prototype to market? Further, is there a way to ensure newly commercialized technology stay afloat in a competitive market? The explicit question is *how can policy tools spur innovation and deployment of renewable energy technology by connecting government agencies and the private market?*

5.1.2 *U.S. Infrastructure for Innovation*

The U.S. has a deep infrastructure for innovation, including both private and public actors, government policies and incentives and a plethora of resources (both human and technological). However, no single innovation policy or national energy policy exists for managing this process of innovation, especially at the federal level. The lack of a national energy policy means that state actors are one of the main drivers of both renewable energy policy innovation as well as actual deployment of renewable energy technology. A 2007 report from the IEA shows the veritable buffet of options that states can choose from: "States use several policy measures for this purpose, including regulatory measures (e.g. renewable portfolio standards), clean energy funds (tax credits and production incentives), support for R&D, and indirect tax incentives." Given that energy production, like politics, is local having a rich tool box to choose from can be extremely useful. All states have adopted at least one of the policy tools created to increase deployment of renewables, be it in the form of electricity generation or vehicle fuels. One popular way to address state specific needs is through the creation of a clean energy fund. These funds "can include production incentives, grants and buy-down programs, long-term contracts, debt financing, and risk insurance."[7] For example, Washington state allocated $75.6 million to its Clean Energy Fund for FY 2013-17.[8] The stated mission of this fund is to address common barrier in R&D, commercialization and technology transfer and barriers to financing (using revolving loans). [9]

Many states also contribute to energy research and development conducted at state universities and in the private-sector. Though research universities play a huge role in the innovation of renewable energy, much of that work is in the basic sciences and therefore outside the purview of this paper. Increasingly, efforts have been made (especially aided by state wide clean energy

funds) to spin out fundamental discoveries in the lab to industry partners or even start-up companies. However, as it stands, the general time horizons of academia alone are too long to be the strongest voice in the quest for commercialization. Currently National Laboratories, as discussed in the next section, are the best conduits to connect government resources with private industry. These are just some of the ways that states as actors are crucial to driving renewable energies to the private market.

The federal government plays a crucial role in commercialization and technological innovation by providing research funding for basic science, creating meaningful partnerships with industry, helping shepherd small businesses to success through grants, and most importantly, the national laboratory system. While the bulk of policy tools discussed in this paper will emerge from the DOE (and many agencies within this department), it should be noted that the process for creating a budget and policy tools for energy R&D is extremely complicated (Figure 2). A large number of agencies are involved with the "technology push" of innovation including the National Science Foundation (NSF), National Institute of Science and Technology (NIST), National Aeronautic Space Agency (NASA) and Department of Defense (DOD). As an example of how extensive renewable energy research can be, in 2007 over $13 billion was awarded by these agencies for research in the physical sciences.[7]

The role of the DOE "is to advance the national, economic and energy security of the United States [..] by encouraging the development of reliable, clean and affordable energy. It administers federal funding for scientific research to further the goal of discovery and innovation, thereby ensuring economic competitiveness and improving quality of life."[5] The DOE has a budget of over $23 billion and over 100,000 employees. Additionally, several offices and large initiatives have been created with the expressed goal of encouraging renewable energy

production. In 2009 the Advanced Research Projects Agency for Energy (ARPA-E) was created under the DOE, with an initial budget of $400 million (total $1.6 billion as of FY 15) and the mission of creating cutting edge renewable energy projects.[10] In 2011, the SunShot initiative was created as a national collaborative effort to bring down the cost of solar energy 75% by 2020 (to $1 per kWh).[11] This price point would make solar energy cost competitive with all other forms of energy on the grid. In addition to these very large programs for renewable energy, the DOE has been a vital agency for designing and implementing policy tools with the expressed purpose of spurring renewable energy innovation and deployment by connecting to industry partners.

The emergence of large scale, private entrepreneurial funds for transformative research and problem solving is a new trend in scientific research. In the clean energy space, the Breakthrough Energy Coalition is potentially a revolution in how renewable energy innovation is realized. Potentially. In their stated mission, the Breakthough Energy Coalition defines themselves against many of the policy tools discussed thus far, "The existing system of basic research, clean energy investment, regulatory frameworks, and subsidies fails to sufficiently mobilize investment in truly transformative energy solutions for the future […] We must also add the skills and resources of leading investors with experience in driving innovation from the lab to the marketplace. The private sector knows how to build companies, evaluate the potential for success, and take the risks that lead to taking innovative ideas and bringing them to the world." Further, the Coalition acknowledges the importance of connecting academic research and the private market: "Experience indicates that even the most promising ideas face daunting commercialization challenges and a nearly impassable Valley of Death between promising concept and viable product, which neither government funding nor conventional private investment can bridge. This

collective failure can be addressed, in part, by a dramatically scaled-up public research pipeline, linked to a different kind of private investor with a long term commitment to new technologies who is willing to put truly patient flexible risk capital to work."[26] The major key here is *long term commitment*. One of the most reoccurring downfalls of the policy tools addressed prior is that their continued existence was largely influenced by the political climate of Washington. Although the approach the Coalition will take is admittedly vague (thus not being able to comment on the key features of the tool), the possibility to have civically minded billionaires dishing out heaps of money to the most creative and entrepreneurial innovators is rather enticing. Further development of this organization will hinge on how eligibility for funds is determined, with the hope that a variety of grants are made available. How much skin these mega wealthy entrepreneurs will actually put on the technologies funded will also be important to watch. However, it seems likely that the big hitters like Mark Zuckerberg and Richard Branson will have quite a bit of sway over large industrial contracts and potentially government ones as well. Though it was once hard to image an anti-establishment, entrepreneurial type getting too mixed up in main stream politics, those particular tides have clearly turned.

5.1.3 *Conclusion and Outlook*

Incentivizing innovation and adoption of renewable energy is a complicated issue. The tools presented here are but a subset of a larger available toolbox that has been created within the past two decades. Just as renewable energy is transformative and presents new institutional challenges, so should our policy tools (or combination of tools) be diverse and adaptable as well. By taking into consideration the uncertainty and risk involved with emerging energy markets, policy tools should seek to promote increased stability and certainty. Creating more mechanisms to connect

public institutions (DOE, research universities) to private industry and larger initiatives assure the more rapid transfer of basic science to transformative technology. Further, with the influence of market forces a part of the dialogue for research funding, researchers can created more robust design principles for advanced materials and device fabrication. Finding common metrics and indicators of success is key to helping these actors work together.

Using fiscal incentives such as tax credits and loan guarantees means larger amounts of available capital that can be dedicated to financing innovative research, large scale deployment of cleantech and helping new businesses bridge the "valley of death" between prototype and mass commercialization. Using the regulatory mechanisms of RPSs, a large scale promotion of all renewable energy can happen nationwide, with the flexibility to fit regional energy needs.

Finally, the U.S. needs to continue to use the momentum of the past several years to devise a national renewable energy strategy that will posit the U.S. as a worldwide leader in policy innovation that keeps pace with its position as a technical leader. Providing long term, stable incentives, be it from private money like the Breakthrough Coalition or Congress, as also key to ensure our energy future.

5.1.4 *References*

1. http://www.eia.gov/totalenergy/data/monthly/pdf/sec1_5.pdf
2. Progress, Tracking Clean Energy. "IEA input to the Clean Energy Ministerial." *International Energy Agency* (2013).
3. Aitken, Donald W. "Transitioning to a renewable energy future." *ISES White Paper* (2003).
4. Margolis, Robert M., and Daniel M. Kammen. "Underinvestment: the energy technology and R&D policy challenge." *Science* 285.5428 (1999): 690-692.
5. IEA. International Energy Agency (IEA). World energy outlook. (Paris: OECD/IEA); (2014).
6. Salamon, Lester M., ed. *The tools of government: A guide to the new governance*. Oxford University Press, 2002.
7.. IEA. International Energy Agency (IEA). World energy outlook. (Paris: OECD/IEA); (2007).
8. http://www.commerce.wa.gov/Programs/Energy/Office/Pages/Clean-Energy-Funds-2.aspx
9.http://c.ymcdn.com/sites/www.cleantechalliancewa.org/resource/resmgr/PDF's/CEF_Summary.pdf
10. http://arpa-e.energy.gov/
11. http://energy.gov/eere/sunshot/sunshot-initiative
12. Mendonça, Miguel, Stephen Lacey, and Frede Hvelplund. "Stability, participation and transparency in renewable energy policy: Lessons from Denmark and the United States." *Policy and Society* 27.4 (2009): 379-398.
13. Gipe, P. (Stephen Lacey). (2008). Energy Equity: Diversifying the market with new incentives. Inside Renewable Energy. Podcast retrieved from http://www.renewableenergyworld.com/rea/news/podcast?id=53554.
14. American Wind Energy Association (2007). PTC fact sheet. http://www.awea.org/pubs/factsheets/PTC_Fact_- Sheet.pdf (Originally from this link which is no longer active. Cited in Ref. 12).
15. http://energy.gov/lpo/loan-programs-office
16. http://www.energy.gov/sites/prod/files/2015/12/f27/DOE-LPO_Report_Financing-Innovation-Climate-Change.pdf
17. http://www.energy.gov/sites/prod/files/2014/11/f19/DOE-LPO-Financial%20Performance%20November%202014.pdf
18. energy.gov/lpo/portfolio
19. https://en.wikipedia.org/wiki/Energy_policy_of_the_United_States
20. http://www.nrel.gov/tech_deployment/state_local_governments/basics_portfolio_standards.html
21. Barbose G. (2013), Renewables Portfolio Standards in the United States: A Status Update, Lawrence Berkeley National Laboratory, presented to State-Federal RPS Collaborative National Summit on RPS, Washington, D.C., 6 November.
22. http://www.eia.gov/todayinenergy/detail.cfm?id=4850
23. https://www.sbv.org/a/pages/projects
24. Hargadon, Andrew. Harvard Business School Working Knowledge for Business Leaders, August 4, 2003.
25. http://www.nrel.gov/workingwithus/assets/pdfs/tto-tpa-infographic-fy15.pdf

26. http://www.breakthroughenergycoalition.com/en/index.html

APPENDIX

Appendix A *Supporting Information for Chapter 2.1*

Experimental methods

Preparation of nanocrystals and nanocrystal inks: The CZTS nanocrystals (NC) were synthesized according to literature methods.[1,2] In a typical synthesis, 1.5 mmol of copper(II) acetylacetonate (99.99%, Aldrich), 0.75 mmol of zinc acetylacetonate (99.995%, Aldrich), 0.75 mmol of tin(IV) bis(acetylacetonate) dibromide (98%, Aldrich), and 10 ml of oleylamine (technical grade, Aldrich) are added into a 100 ml three neck flask connected to a Schlenk line. The mixture was heated to ~130 ˚C under vacuum, and then degassed for 30 minutes and purged with argon three times. At this point, the color had changed to a dark brown. The temperature was then raised to 225 ˚C at which point 4 ml of a 1.00 M solution of sulfur in oleylamine was injected. After injection, the color of the solution turned darker brown and eventually black after holding the temperature at 225 ˚C for 120 minutes. The mixture was then cooled to ~80 ˚C by removing the heating mantle. The cooled mixture was split between two centrifuge tubes, which were then filled with a 1:1 hexane:ethanol solution. The samples were then centrifuged at 10000 rpm for 5 minutes. After centrifugation, the supernatant was decanted, and the precipitate was redispersed in hexane. Isopropanol was then added such that the hexane:isopropanol ratio was 1:2. The sample was again centrifuged. This redispersion/centrifugation process was repeated four times. After the final wash, the pellet of nanocrystals was dried under slow nitrogen flow. The dried nanocrystals were redispersed in hexanethiol (200mg/mL) to form the nanocrystal ink.

Preparation of CZTSSe films and fabrication of solar cell devices: The CZTS nanocrystal ink was directly applied to a Mo coated (500 nm) soda lime glass substrate by knife-coating to form

nanocrystal thin films. Typically, 4-7 mL of ink is spread across the substrate with a glass rod. The wet films are then dried in air on a hotplate at 350 ˚C. The coating and drying steps are repeated until an optically thick film forms, which may take 2-8 layers depending on the ink and coating technique. Films were then annealed with elemental Se (selenization) at a temperature of 500 ˚C for 20 min in a vented graphite box inside a quartz tube furnace with Ar flow. For SKPM characterization these films were transferred to a N_2 atmosphere glove box after the furnace cooled down to room temperature. For device fabrication, the films were soaked in DI water for 5 min and then immediately immersed in a 65 ˚C bath solution containing 150 mL DI water, 22 mL 0.015 M $CdSO_4$ and 28 mL of a 14.8 M NH_3H_2O solution for chemical bath deposition (CBD) of the CdS buffer layer. After 1 min soaking, 22 mL 0.75 M thiourea solution was added to the above solution to initiate the formation of CdS. The deposition continued for 11 min to obtain a thickness of about 40 nm. 50 nm i-ZnO and 250 nm ITO layers were then deposited in one run by RF sputtering on a Lesker Lab 18 sputter system (Kurt J. Lesker Company). The devices were finished by thermal deposition of the 50 nm Ni and 500 nm Al top contact grids through a shadow mask.

Device characterization: Current-voltage (I-V) measurements were performed using a Keithley 2400 source-measure unit and 100 mW/cm^2 simulated AM1.5G light from a xenon arc lamp via appropriate filters.

SPM experiments: SPM data were acquired on a MFP-3D-BIO (Asylum Research)-based SPM with custom modifications[3-5] using 300 kHz Pt-coated cantilevers (BudgetSensor ElectriTap300) with a work function of ~4.8 eV[6-8] (outside of a UHV environment) for SKPM. SKPM images were obtained in a two-pass process. Topography was collected in standard atomic force

microscopy (AFM) intermittent contact mode on the first pass. During the second pass the tip was moved to a constant height above the surface (50 nm) and the surface potential of the same line was measured. During the lift pass an AC bias (700 Hz, 2 V peak-to-peak) was applied to the cantilever from a function generator, combined with a DC bias from the AFM controller via a home-built summing amplifier. The cantilever phase signal from the AFM control was then sent to an SR830 lock-in amplifier, referenced at 700 Hz, and the lock-in signal was returned to the AFM controller to use as a feedback signal. A feedback loop in the controller was set to null this phase signal by adjusting the DC bias applied between the tip and the substrate, thereby measuring the contact potential difference.[3,9] Samples were assembled in a flow cell while in a N_2 glove box and imaged under constant nitrogen flow. Details and schematics for the AFM techniques have been reported previously.[3]

SEM/EDS experiments: Samples for SEM/EDS were imaged without additional preparation after SPM measurements. SEM images were taken using a FEI Sirion SEM at 5 kV. EDS compositional profiles were also taken on the Sirion SEM at 20 kV using the AZtecEnergy EDS software package (version 2.1).

Additional Experimental Results

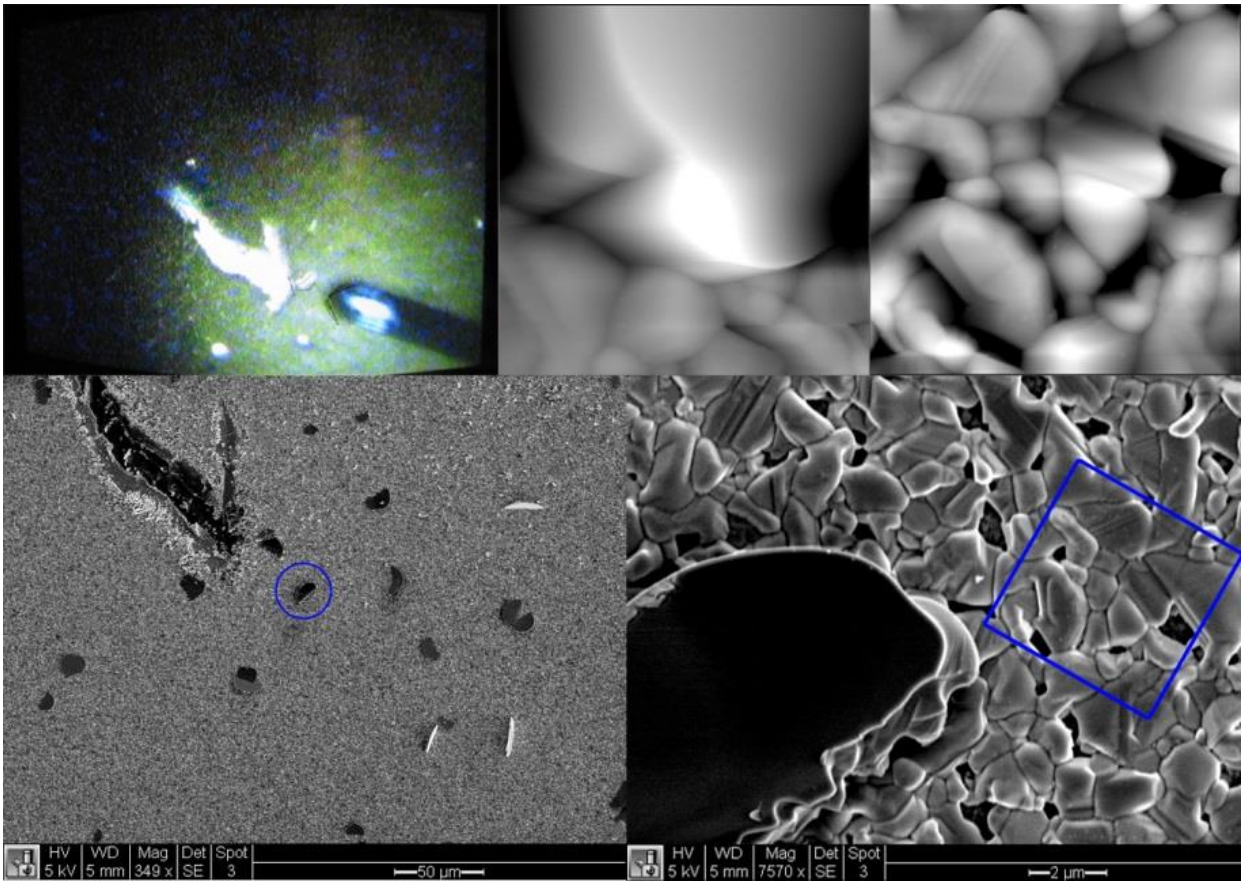

Figure S1 Top down view showing the approach for correlating AFM with SEM micrographs. Top left: CCD camera on AFM; Top center: AFM topography showing the same feature as in the bottom right SEM image; Top right: AFM topography image of the same are as shown in the SEM image, bottom right (blue square); Bottom left: SEM image of the same area as top left (the circle shows the same feature as in bottom right); bottom right: SEM image.

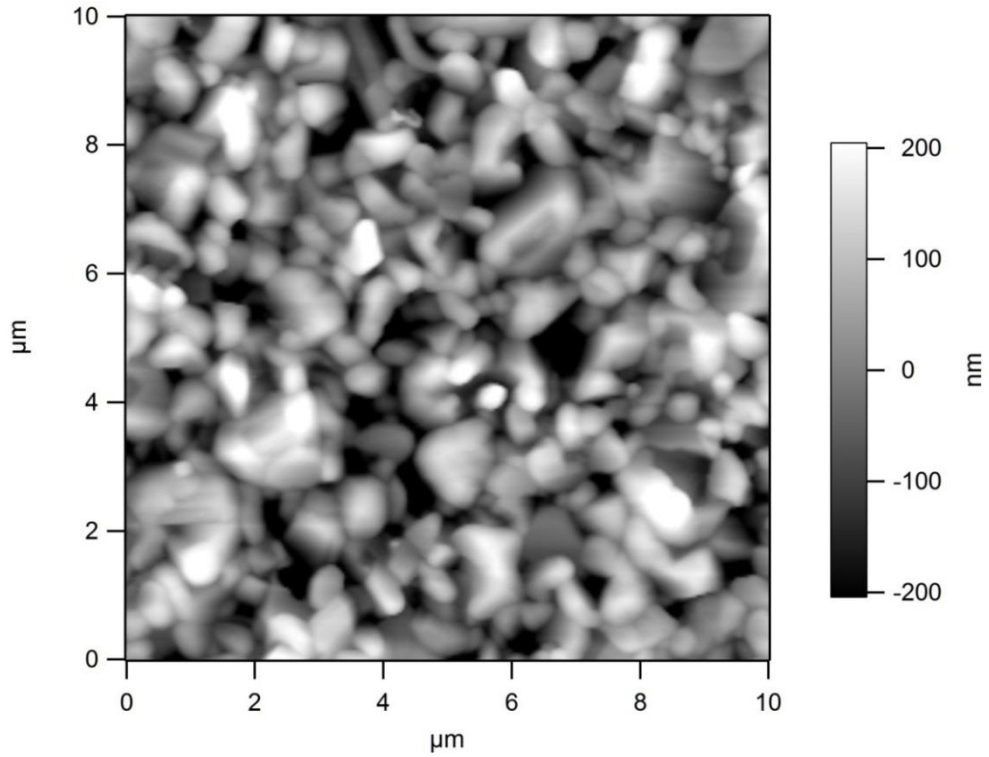

Figure S2 10x10 µm topography scan (flattened) of the NC-CZTS sample used in this study.

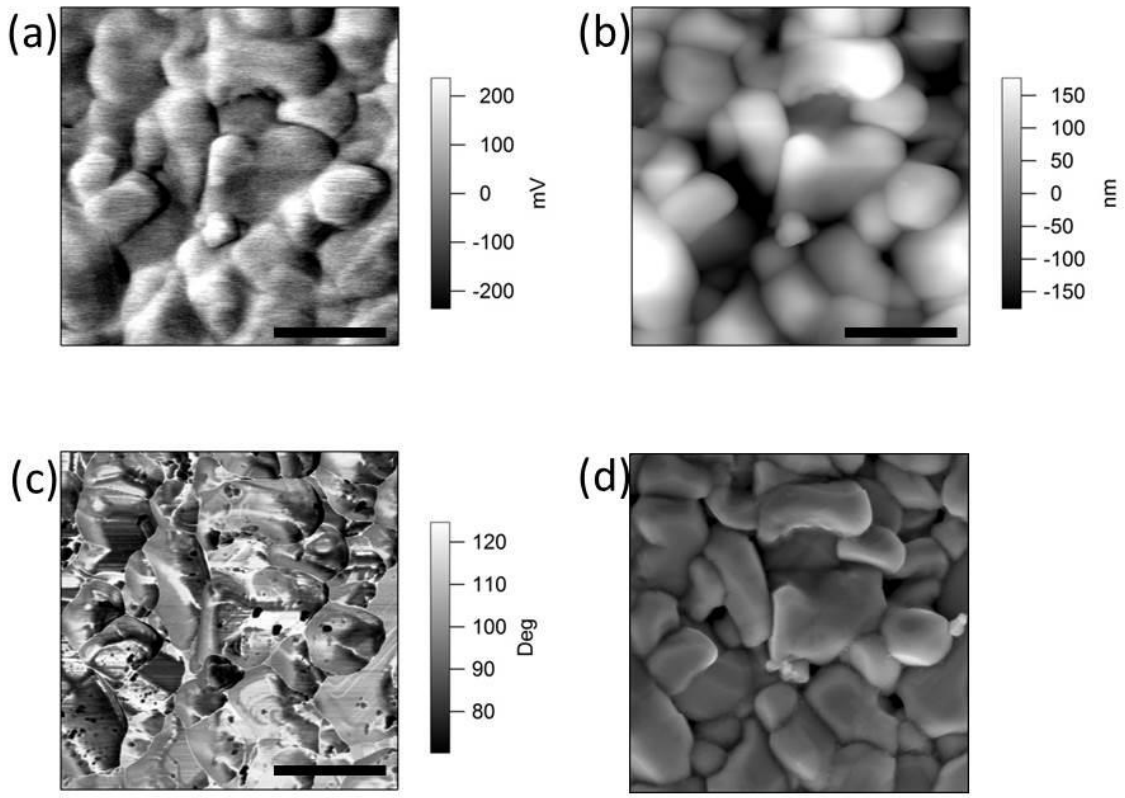

Figure S3 Scanning probe and scanning electron microscopy images of a NC-ink CZTSSe sample: a) SKPM, b) topography, c) phase and d) SEM image of the same sample area. The SKPM image shows differences in surface potential for regions of similar topographical height suggesting that the SKPM signal is not predominantly induced by the topography. The scale bar represents 1 μm.

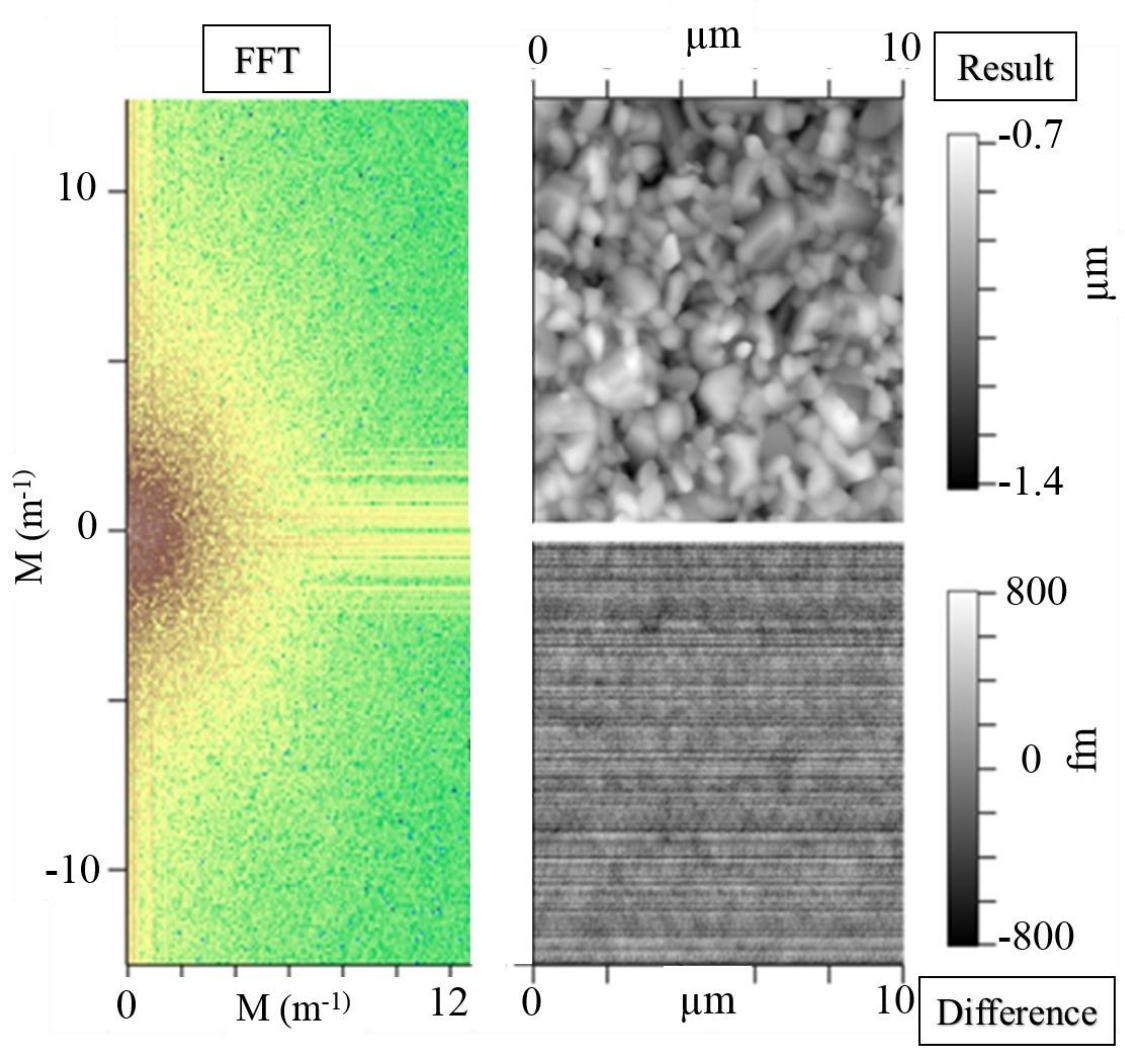

Figure S4 Fast Fourier transform (FFT) of the film shown in Figure S2. The film reveals a characteristic feature size and distinct grains, which allowed the area scanned with the AFM to be identified under the SEM.

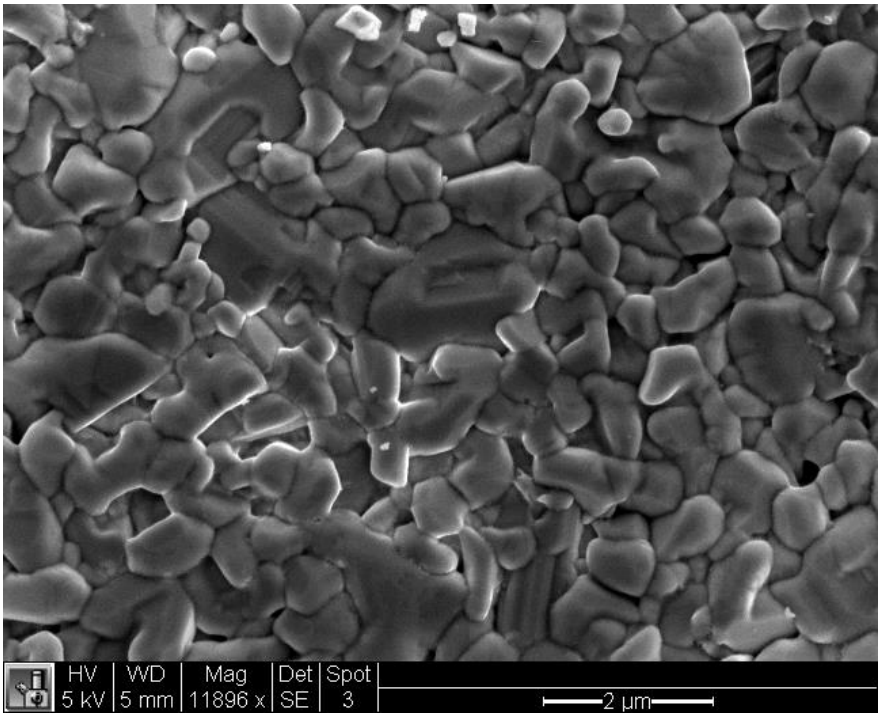

Figure S5 SEM micrograph of the NC-CZTS sample used in this study (area overlaps with Figure S2).

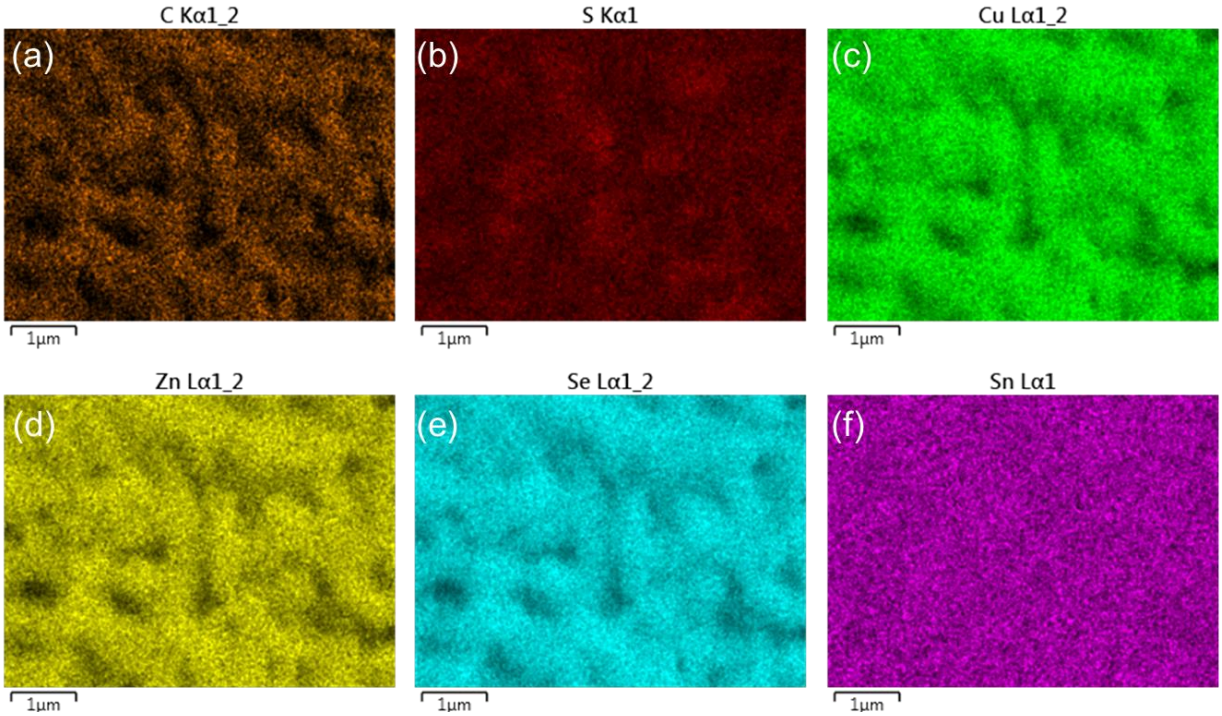

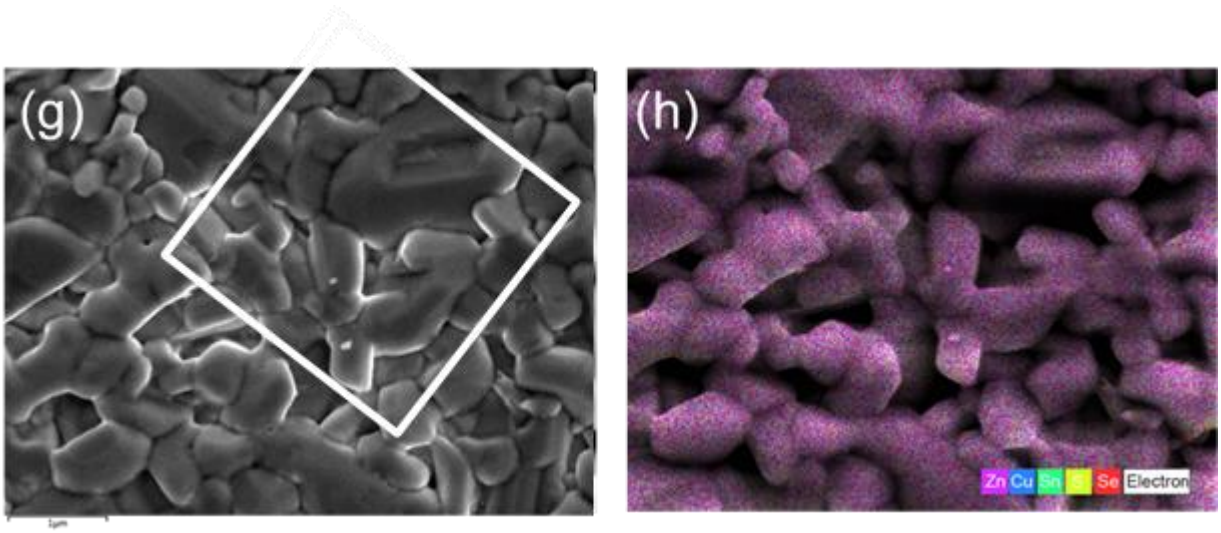

Figure S6 Elemental EDS scans (a – f), corresponding SEM micrograph (g) and layered EDS scan (h) of NC-CZTS sample. The white frame on top of the SEM image indicates the same area that was scanned with the AFM (see Figure 2 and 3 of the main text).

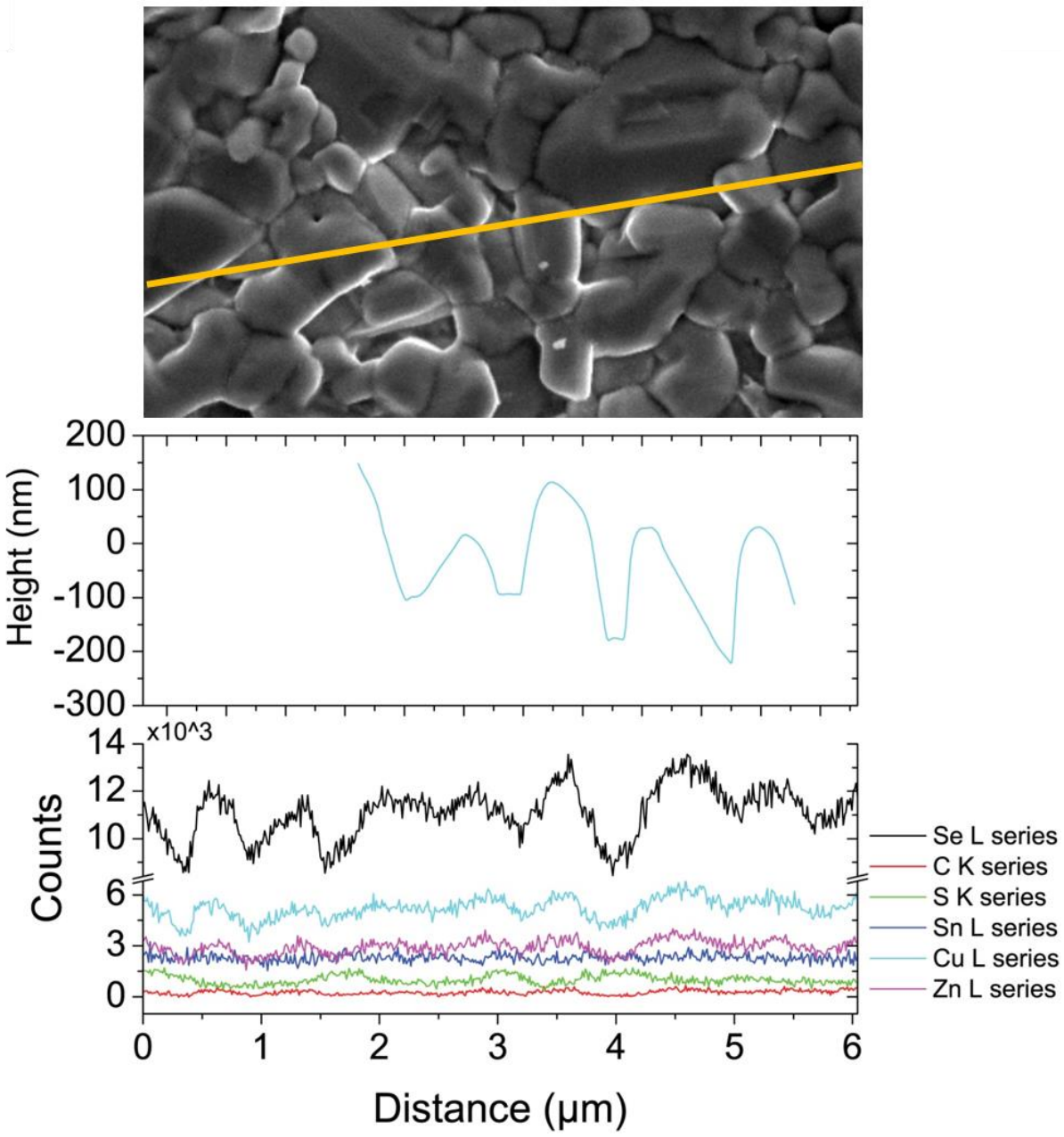

Figure S7 Comparing EDS line scan (20 averages, same line trace as in Figure 4) showing all relevant chemical constituents with AFM topographical height.

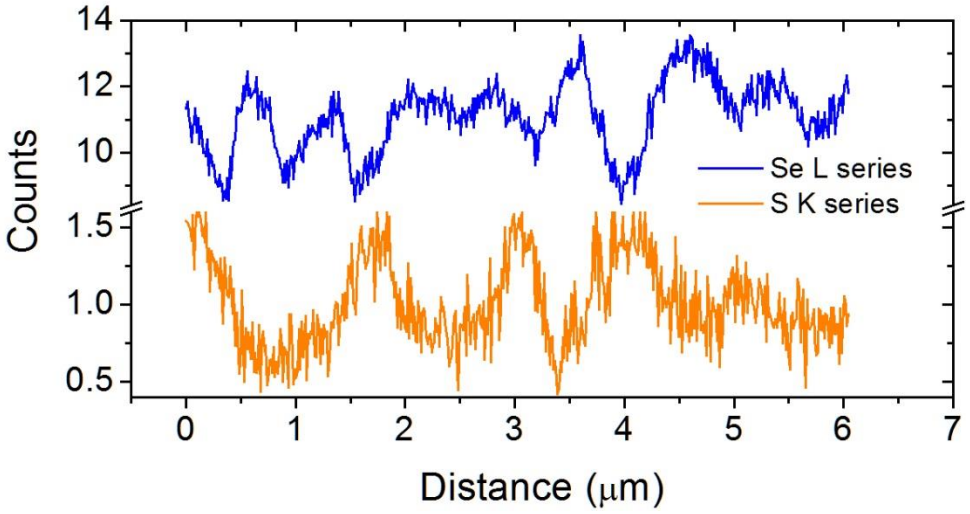

Figure S8 EDS line scans (20 averages, same line trace as in Figure 4) of S and Se.

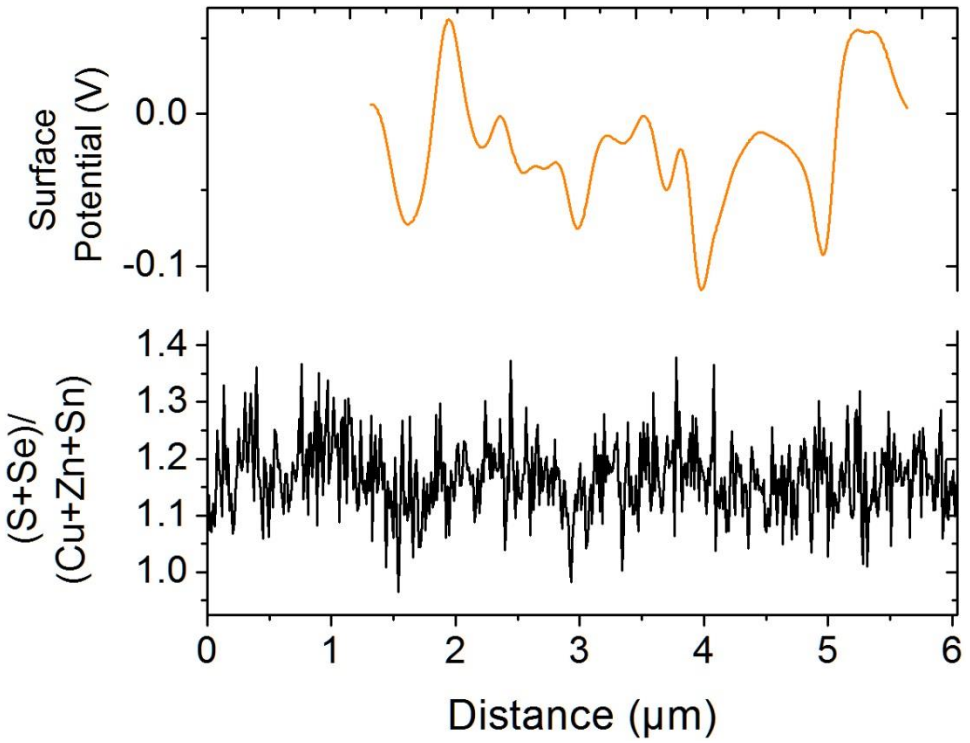

Figure S9 SKPM signal (top) and S+Se/(Cu+Zn+Sn) ratio along the red line trace in Figure 3.

No obvious correlation between surface potential and S+Se/(Cu+Zn+Sn) is observed.

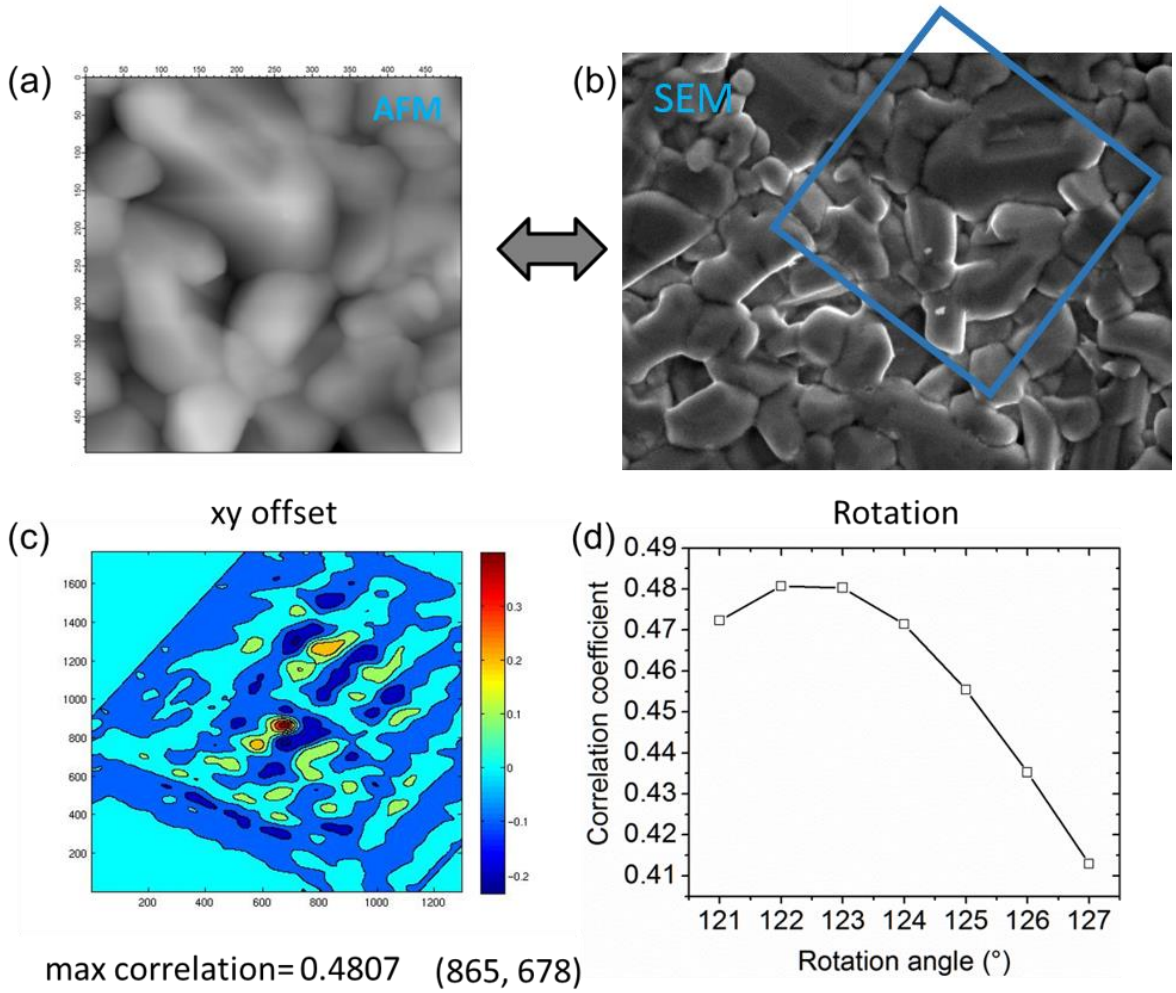

Figure S10 Approach for correlating AFM topography (a) and SEM micrographs (b). The inset area in (b) corresponds to the area scanned with the AFM (a). Digital image correlation upon x-y displacement and image rotation was performed using an algorithm provided by the software IgorPro6.1. Figure (c) shows one representative image correlation and (d) the correlation coefficient as a function of the rotation angle for the best x-y correlation.

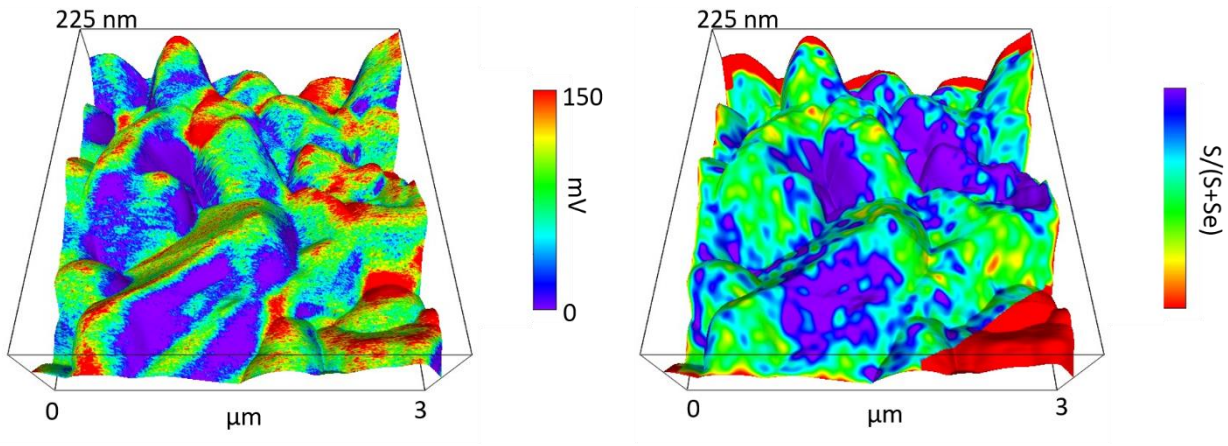

Figure S11 a) Surface potential overlaid on topography and b) S/(S+Se) ratio overlaid on topography, showing 2D correlation between spikes in sulfur and dips in potential from SKPM. Most areas of purple on the left correlate with areas of purple on the right.

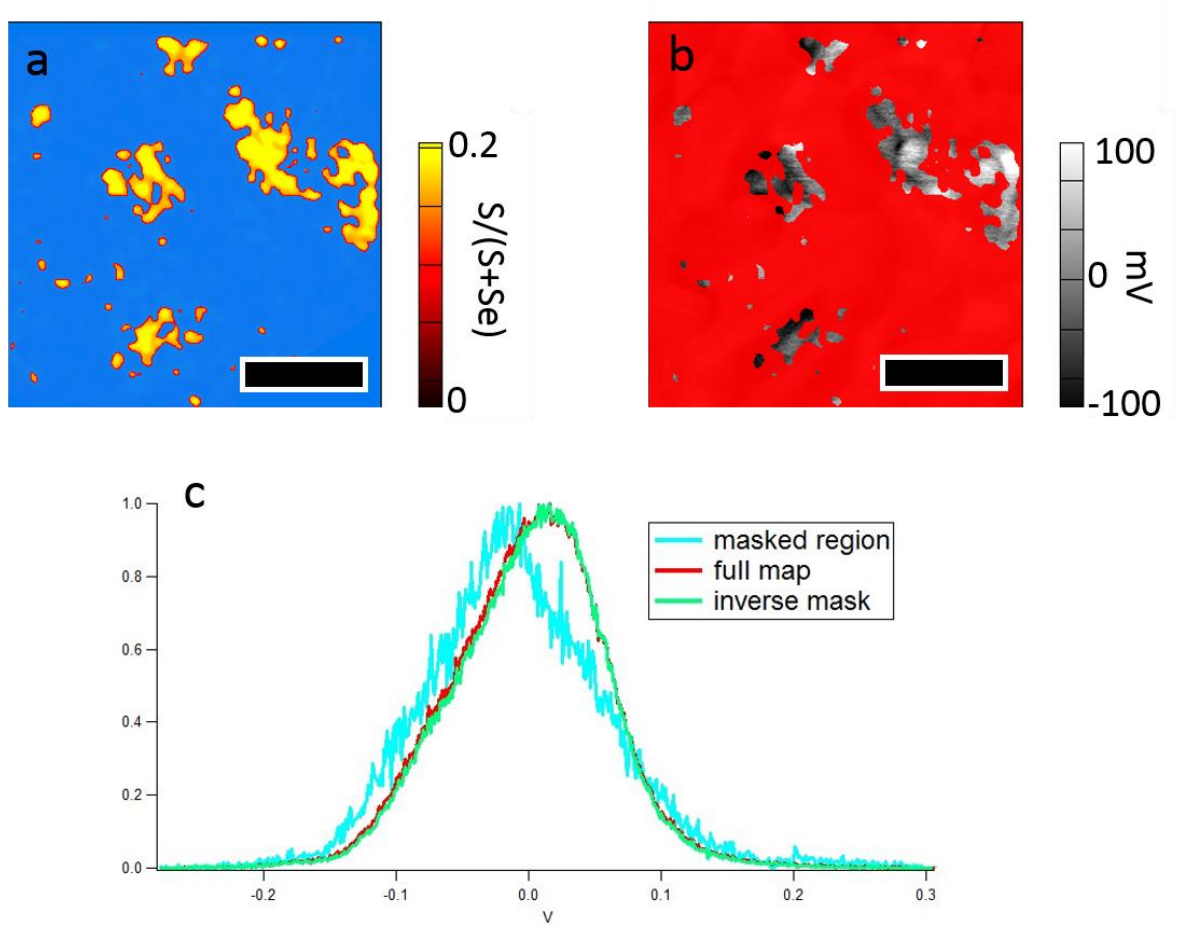

Fig. S12 Comparison of areas with high (>0.2) ratio of S/(S+Se) to areas of low (<-50 mV) potential. (a) areas of high S(S+Se) ratio (yellow), (b) same areas overlaid on potential map (grey). (c) histogram showing distribution of potentials in masked region from (a), entire map and inverse of the mask region. 45% of pixels from yellow area in (a) fell below -50 mV showing more areas of low potential are associated with high S/(S+Se) ratio than are distributed across entire film. Scale bars = 1 μm.

Figure S13 SEM of NC-CZTS sample. The area is the same as in Figures 2 and 3. Spectra of the whole area as well as of specific areas with prominent features in the EDS and SKPM maps were analyzed. For instance, the EDS line trace labeled “Line Data 1” is shown in Figure 3.

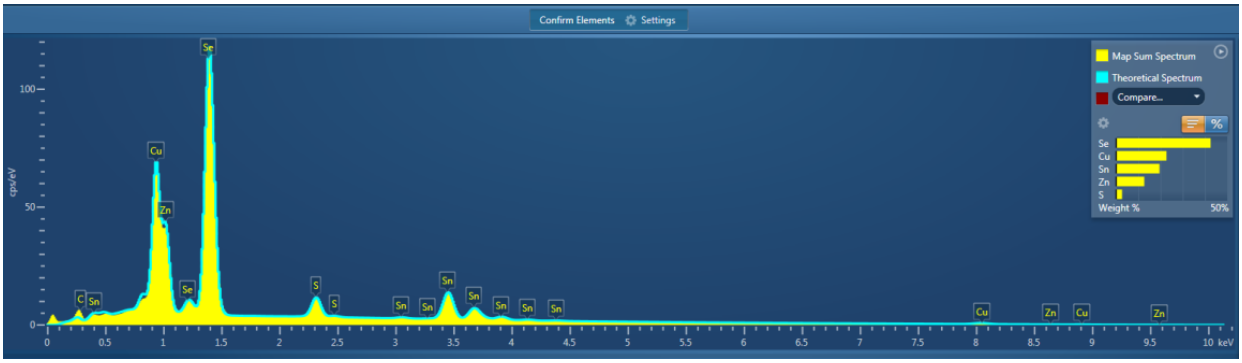

Figure S14 Typical EDS spectrum of NC-CZTS sample as acquired by the AZtecEnergy EDS software (version 2.1) from Oxford Instruments.

NC-CZTS, Mo excluded (cyan: theoretical curve, whole SEM map area)

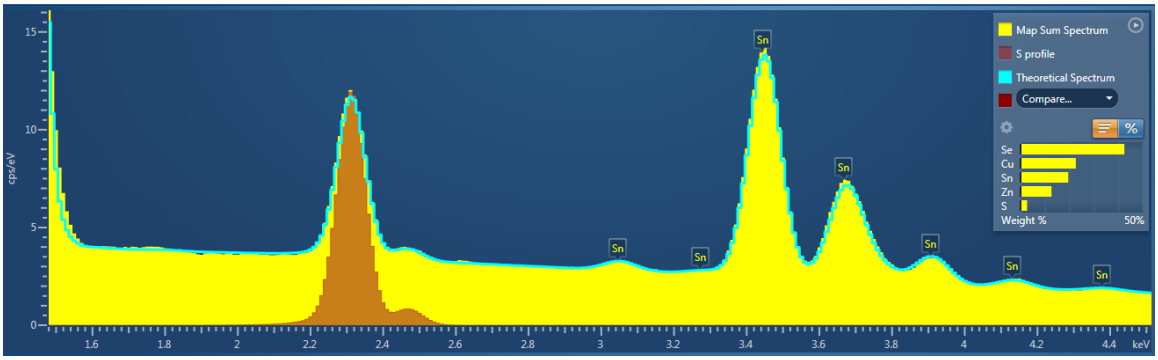

NC-CZTS, Mo <u>included</u> (cyan: theoretical curve)

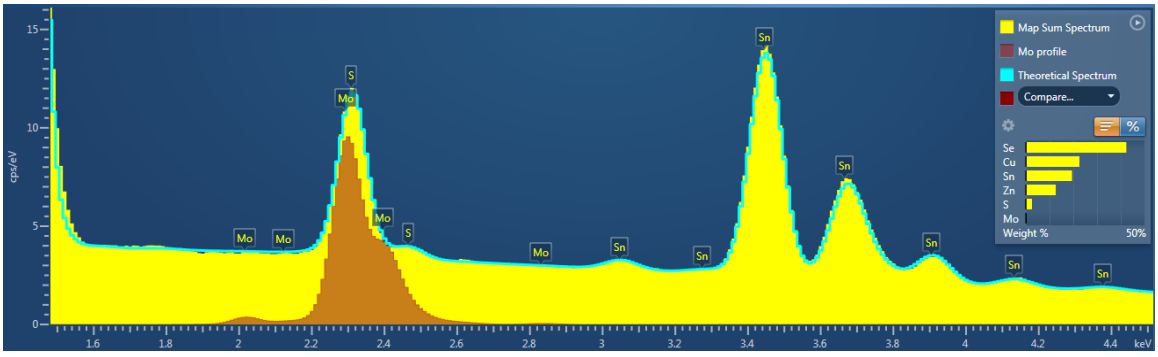

NC-CZTS, Mo included, S excluded (cyan: theoretical curve)

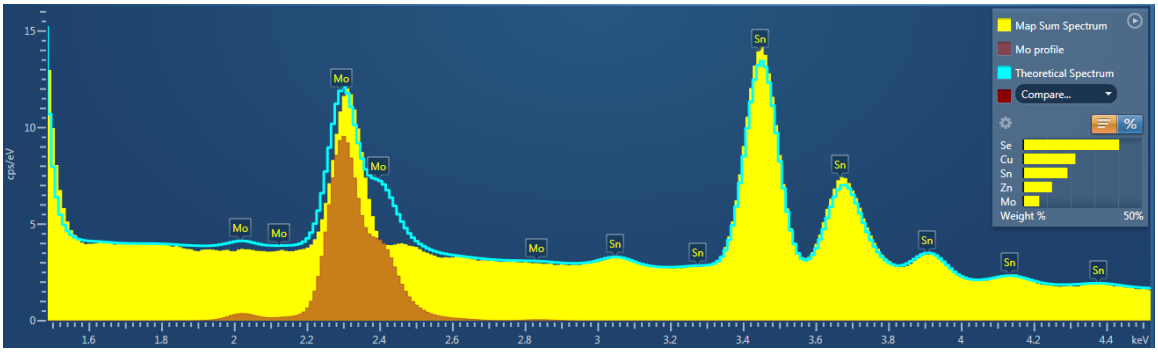

Figure S15 Experimental and theoretical EDS spectra as measured and computed by the AZtecEnergy EDS software (version 2.1) from Oxford Instruments. Top: Mo was not included in the elemental analysis; Center: Mo was included in the elemental analysis; bottom: Mo was included and S excluded from the elemental analysis.

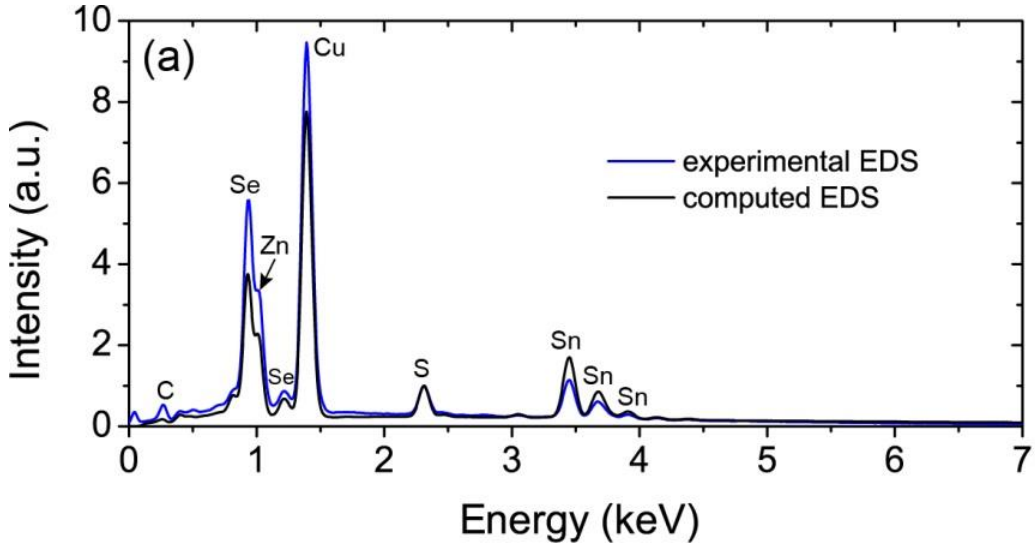

A

Map Sum Spectrum	Atomic %
S	6.27
Cu	26.59
Zn	14.47
Se	40.37
Sn	12.30
Total	100.00
(Mo not included)	

B

Map Sum Spectrum	Atomic %
S	6.04
Cu	26.67
Zn	14.48
Se	40.23
Mo	0.28
Sn	12.30
Total	100.00
(Mo included)	

C

Map Sum Spectrum	Atomic %
S	5.96
Cu	25.26
Zn	13.75
Se	38.35
Mo	5.0
Sn	11.68
Total	100.00
(Mo included)	

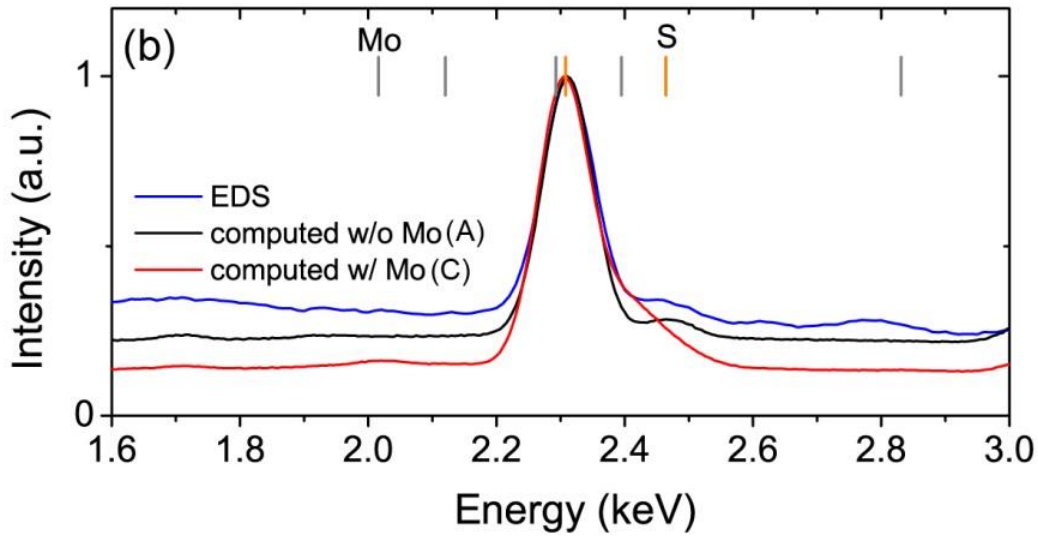

Figure S16 (a) Experimental and computed EDS spectra of the SEM area shown in Figure 3 and Figure S12. The theoretical EDS spectra were computed using Inca software from Oxford Instruments. Using EDS composition analysis with the AZtecEnergy EDS software we obtained the composition A (molybdenum not included) and B (molybdenum included). When molybdenum (Mo) was manually set to be included the system evaluated the Mo content to be 0.28 atom%. In Figure S15(a) the theoretical spectrum was computed without Mo. Discrepancies between the measured and the computed EDS spectrum are most likely due to deviations in the geometry of the setup in the calculations and the experiment and the morphology of the sample. (b) Experimental and computed EDS spectrum around the overlap region of sulfur (S:Kα1) and molybdenum (MoLα1). The most prominent spectral line positions are shown at the top. The two computed EDS spectra are based on the composition A (no Mo), extracted from the AZtecEnergy software, and a theoretical composition that was set to mimic an atomic percentage of 5%, while keeping the relative amounts of the other constituents constant (composition C).

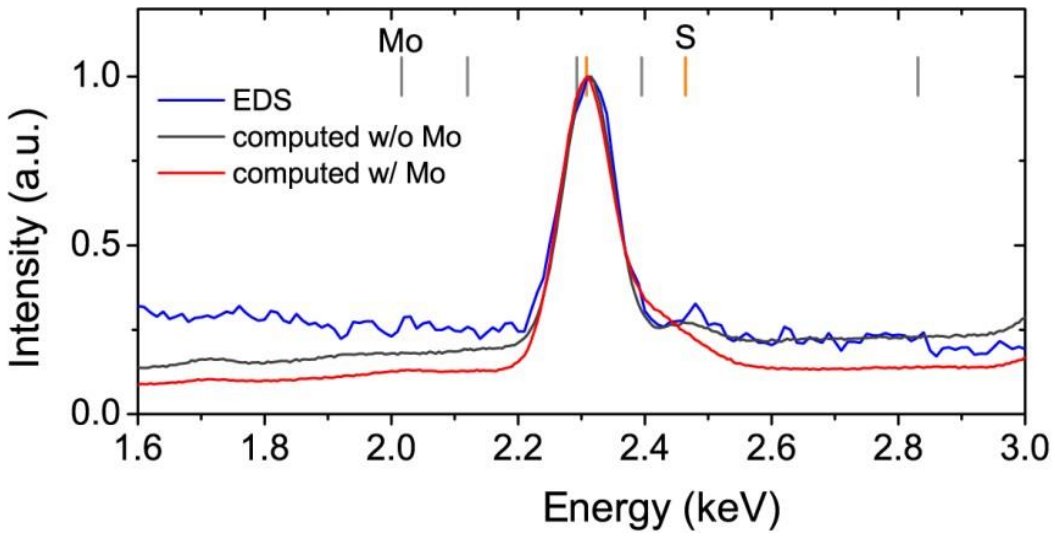

Figure S17 Experimental and computed EDS spectrum of the area designated by spectrum 4 in Figure S12. See caption of previous Figure for details.

Observations/Conclusions

The comparison in Figure S15(b) shows that the theoretical spectrum with no molybdenum matches the experimental EDS spectrum closely. In particular, the two signals that originate from sulfur (2.31 and 2.46 keV) are well separated. The spectrum with 5 atom% of molybdenum, on the other hand, shows a pronounced shoulder at 2.40 keV that is not present in the experimental EDS spectrum. The same qualitative trend is observed when probing an area of large sulfur content (e.g., area designated by spectrum 4 in Figure S12, compare with Figure 3; see EDS spectrum in Figure S16).

Note that the average S/Se ratio is 0.155. In regions of high S/Se ratio, e.g., area designated by spectrum 4 in Figure S12, the ratio is in the order of 0.212. This represents an increase by 37%. Compared to regions of low S/Se ratio, e.g., area designated by spectrum 6 in Figure S12 (S/Se=0.130), the increase is even more pronounced (63%). Overall, the low amount of molybdenum predicted by the AZtecEnergy software (0.28 atom%) together with the absence of the molybdenum shoulder in the experimental EDS spectrum and considering the thickness of the CZTS film (~1.5 μm) and an estimated depth of penetration for the electron beam of 0.5 – 0.6 μm suggest that the signal detected at the sulfur/molybdenum overlap energy predominantly originates from sulfur in the sample. This allows the conclusion that the areas showing correlated features in the SKPM and the EDS maps emerge from variations in the S/Se ratio.

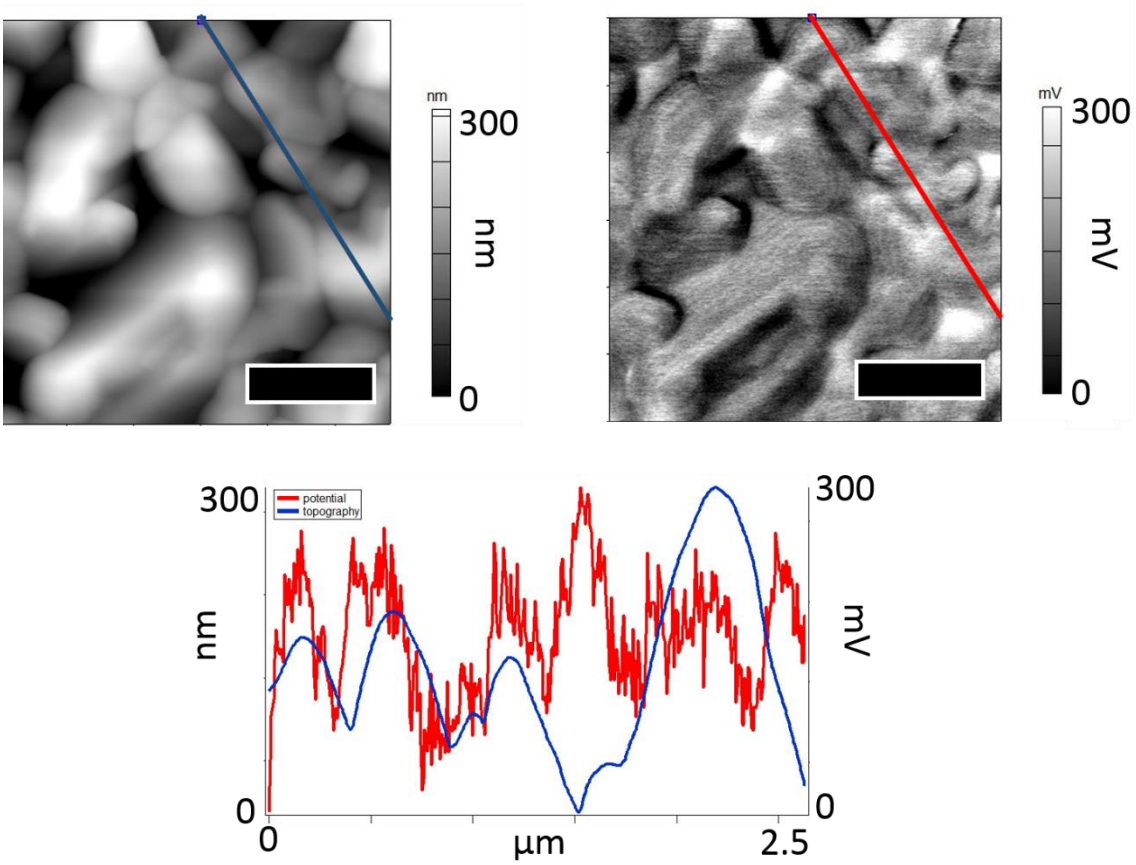

Figure S18 Line scan showing no correlation between topography and surface potential images. (a) AFM topography (same as Figure 3b), (b) SKPM potential map (same as Figure 3d), and (c) overlay of the two line scans. A Pearson product-moment correlation returns a coefficient of -0.032 revealing little to no correlation between these two lines, with -1 being completely anticorrelated and 1 being completely correlated.

References

(1) Guo, Q.; Hillhouse, H.; Agrawal, R. *J. Amer. Chem. Soc.* **2009**, *131*, 11672-11673.

(2) Guo, Q.; Ford, G.; Yang, W.; Walker, B.; Stach, E.; Hillhouse, H.; Agrawal, R. *J. Amer. Chem. Soc.* **2010**, *132*, 17384-17386.

(3) Pingree, L.; Reid, O.; Ginger, D. *Adv. Mater.* **2009**, *21*, 19-28.

(4) Groves, C.; Reid, O. G.; Ginger, D. S. *Acc. Chem. Res.* **2010**, *43*, 612-620.

(5) Giridharagopal, R.; Ginger, D. S. *J. Phys. Chem. Lett.* **2010**, *1*, 1160-1169.

(6) Derry, G.; Ross, P. *J. Chem. Phys.* **1985**, *82*, 2772-2778.

(7) Beierlein, T.; Brutting, W.; Riel, H.; Haskal, E.; Muller, P.; Riess, W. *Synth. Met.* **2000**, *111*, 295-297.

(8) Gland, J.; Sexton, B.; Fisher, G. *Surf. Sci.* **1980**, *95*, 587-602.

(9) Sadewasser, S.; Glatzel, T. *Kelvin Probe Force Microscopy: Measuring and Compensating Electrostatic Forces*; Springer Verlag: Heidelberg, 2011; Vol. 48.

Appendix B *Supporting Information for Chapter 2.2*

Experimental

Molecular ink preparation and semiconductor film formation. Non-doped and Li-doped inks we prepared as follows: 1140.8 mg Cu(CH3COO)2·H2O (99.99%, Sigma-Aldrich) and 886.4 mg SnCl2·2H2O (99.99%, Sigma-Aldrich) were mixed in 5 ml DMSO (99.99%, anhydrous, Sigma-Aldrich) and stirred overnight at room temperature; then 555.0 mg ZnCl2 (99.99%, Sigma-Aldrich) was added and stirred until completely dissolved; finally, 1560.2 mg thiourea (obtained from Sigma-Aldrich and recrystallized from DI water twice; details of recrystallization are given in SI) was added and a transparent, colorless solution was obtained after 2 hours stirring. The solution was split into two equal parts, solution A was diluted by 1.0 ml DMSO (without LiF) and solution B was diluted by 1.0 ml DMSO containing 2 mg LiF (99.99%, anhydrous, Sigma-Aldrich). The atomic ratio in solution B was Li/(Cu+Zn+Sn)=0.011. Both solutions were filtered with 2 μm PTFE filters prior to coating. Inks were spin-coated onto molybdenum coated sodalime glass substrates at a spin speed of 1500 rpm for 60s and then immediately annealed on a hotplate (set point of 540 °C) for 2 min. This process was repeated five times to create a layer of approximately 700 nm. All solution preparation, spin-coating, and annealing were conducted in a N2 filled glovebox system with oxygen and water at less than 10 ppm. The CZTS films were then annealed with elemental Se in a vented graphite box at temperature of 540°C for 20 min to form CZTSSe.

Solar cell device fabrication and characterization. The Starting from the selenized film as described above was first submerged in DI water for 5 min and then immediately put into CdSO4/NH3 solution for chemical bath deposition (CBD) of 30 nm CdS as described in previous reports.30, 35. Then, the devices

Appendix C *Supporting Information for Chapter 3.2*

Experimental Methods

Materials. Methylammonium iodide (MAI) was synthesized according to a literature procedure as follows.[2] γ-Butyrolactone was dried over molecular sieves and degassed by continuous nitrogen stream. The perovskite precursor solution was prepared by mixing 159 mg (1.0 mmol) of MAI and 461 mg (1.0 mmol) of lead(II) iodide (PbI_2, 99.9985% purity) in 1.0 mL of 7:3 volume ratio of γ-butyrolactone and dehydrated DMSO mixed solvents. The resulting 1.0 M of $CH_3NH_3PbI_3$ precursor solution was stirred 30 min at 60 °C and filtered with a 0.45 μm PTFE filter. The solution was stored under a dry nitrogen atmosphere. Other materials were used as received.

Film and device fabrication. The planar heterojunction scheme was used in the fabrication of the degraded devices. A PEDOT:PSS layer (50 nm) was spin-coated at 3000 rpm on an ITO substrate that had been cleaned by detergent, distilled water, acetone, and isopropyl alcohol, followed by plasma cleaning. A 200-nm-thick perovskite layer was deposited by spin-coating in an inert environment using solvent washing technique;[28] after heating the precursor solution at 100 °C, the solution was spin-coated at 500 rpm for 5 seconds, 1000 rpm for 40 seconds, and 4000 rpm for 40 seconds. In the middle of the last period, 700 μL of toluene was dripped onto the spinning substrate. The perovskite layer was then annealed at 100 °C for 15 minutes. The films were subjected to the degradation process and subsequent UV-vis spectroscopy and scanning probe characterization described below at this point in the device fabrication. An 80 nm thickness of PCBM layer was then spin-coated from a 30 mg/mL chlorobenzene solution at 1500 rpm on the perovskite layer in an inert environment. 8 nm of BCP layer and aluminum contacts of 100 nm thickness were thermally evaporated onto the PCBM layer.

Degradation. The films were left in a home-built humidity controllable container under the light of a white LED, LZ1-10CW00. LED Engin (See Figure S9 for LED spectrum) for varying amounts of time corresponding to varying photon doses. All degradation experiments were conducted at approximately constant room temperature (25 °C).

Compositional and morphological characterization. The composition of the perovskite layer as a function of photon dose was studied by taking UV-vis spectra after each exposure. A ITO/PEDOT:PSS film was measured as a background. The morphology of the perovskite layer as a function of photon dose was probed with topographical AFM in AC mode at scan rate 1.0 Hz. As an *in situ* AFM experiment, a fresh film was degraded under white light at 113 mW/cm^2 in an ambient atmosphere (23 °C, 55%RH) in AFM so that the evolution of morphology as a continuous function of photon dose could be observed.

Device characterization. Current density−voltage ($J-V$) curves were recorded at a scanning rate of 0.15 V/s, under illumination of simulated AM1.5G illumination at intensity of 100 mW/cm^2 in an inert atmosphere. Hysteresis index was defined by |1-PCE (forward scan)/PCE (reverse scan)|. EQE measurements were performed under vacuum with a monochromated light from a 100 W tungsten-halogen bulb and source meter using a calibrated Si-photodiode as a reference. Devices and the photodiode were masked to control the active area as 1.3 mm^2.

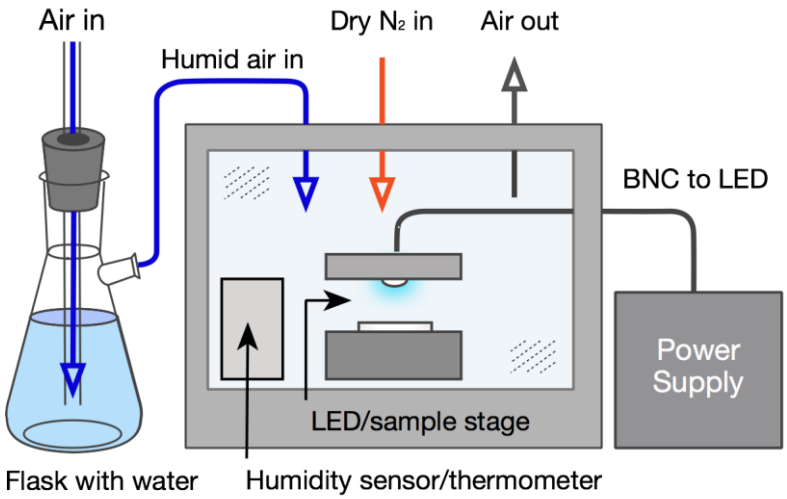

Figure S1. Set up of house-built humidity control container for degrading films and devices. Power supply was used to control the intensity of cool white, 5500 K LED (LZ1-10CW00, LED Engin). Lab air could be connected to flow through flask of DI water. Valves allowed control of humidity throughout degradations.

Table S1. Summarized photovoltaic parameters[a] for reverse scans of the devices completing PCBM/BCP/Al layers (A) after and (B) before exposing 100 mW/cm^2 light in 40%RH air.

	Photon dose (J/cm^2)	Jsc (mA/cm^2)	Voc (V)	FF	PCE (%)	HS[b]
(A)	0	10.22 ± 0.63	0.90 ± 0.01	0.80 ± 0.01	7.34 ± 0.52 (8.07)	0.03 ± 0.02
	1500	10.55 ± 0.34	0.97 ± 0.01	0.81 ± 0.01	8.23 ± 0.27 (8.47)	0.04 ± 0.02
	3000	8.80 ± 0.83	0.96 ± 0.01	0.85 ± 0.02	7.22 ± 0.64 (8.19)	0.13 ± 0.03
	3400[c]	3.40 ± 0.79	0.90 ± 0.04	0.79 ± 0.05	2.46 ± 0.76 (3.41)	0.19 ± 0.04
	3600[c]	1.80 ± 0.10	0.83 ± 0.04	0.65 ± 0.09	0.97 ± 0.20 (1.22)	0.39 ± 0.06
	3800[c]	0.94 ± 0.23	0.54 ± 0.03	0.32 ± 0.02	0.16 ± 0.03 (0.22)	0.14 ± 0.09
(B)	0	7.25 ± 0.43	0.87 ± 0.01	0.87 ± 0.01	5.47 ± 0.33 (5.91)	0.09 ± 0.01
	150	7.34 ± 0.33	0.87 ± 0.01	0.68 ± 0.04	4.39 ± 0.21 (4.83)	0.06 ± 0.01
	300[c]	7.81 ± 0.48	0.89 ± 0.01	0.49 ± 0.05	3.40 ± 0.25 (3.81)	0.08 ± 0.05
	450	7.12 ± 0.35	0.89 ± 0.01	0.44 ± 0.06	2.74 ± 0.35 (3.32)	0.05 ± 0.01
	750	6.52 ± 0.34	0.88 ± 0.01	0.29 ± 0.04	1.66 ± 0.28 (2.15)	0.06 ± 0.03

1200	5.64 ± 0.39	0.89 ± 0.01	0.19 ± 0.03	0.95 ± 0.16 (1.19)	0.13 ± 0.05
1500	4.59 ± 0.35	0.88 ± 0.02	0.15 ± 0.02	0.62 ± 0.13 (0.78)	0.15 ± 0.05
2100[c]	2.69 ± 0.89	0.77 ± 0.27	0.13 ± 0.04	0.27 ± 0.14 (0.45)	0.15 ± 0.07
2700[c]	2.01 ± 0.64	0.75 ± 0.20	0.11 ± 0.03	0.17 ± 0.08 (0.26)	0.17 ± 0.04

[a] Average values from 8 pixels with standard deviation. Maximum values in parentheses.
[b] Hysteresis index = |1-PCE (forward scan)/PCE (reverse scan)|.
[c] Average values from 6 pixels.

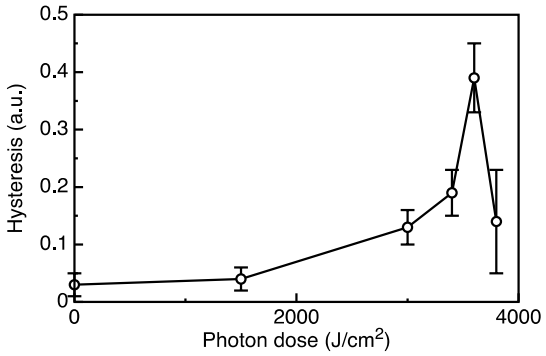

Figure S2. Hysteresis index as a function of photon dose. Hysteresis index was defined by |1-$PCE_{forward\ scan}/PCE_{reverse\ scan}$|. Error bars represent standard deviation.

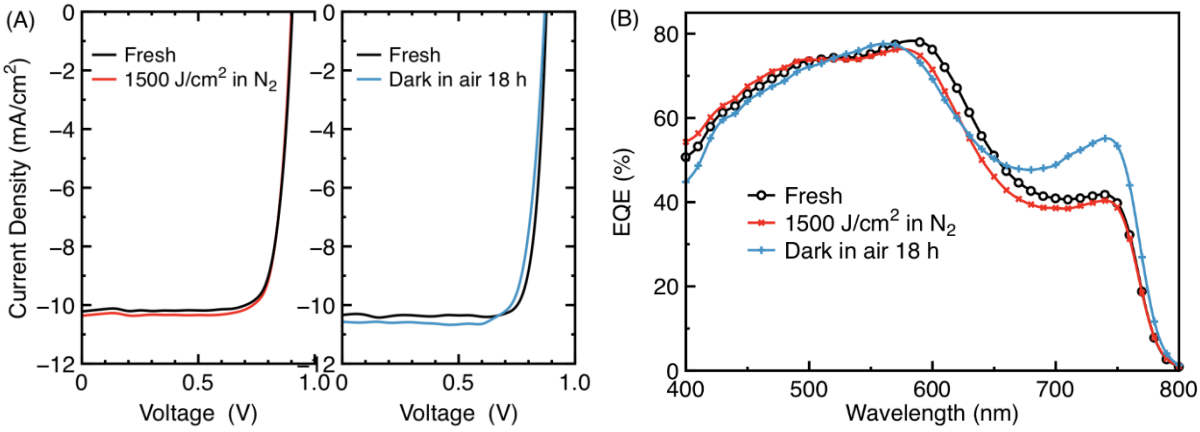

Figure S3. (A) Current density-voltage curve and (B) EQE spectra for the $MAPbI_3$ devices made from fresh films, a film irradiated 1500 J/cm^2 photon dose (~4 hours) in N_2 atmosphere, and a film kept in dark under ambient air (40%RH, r.t.) for 18 hours.

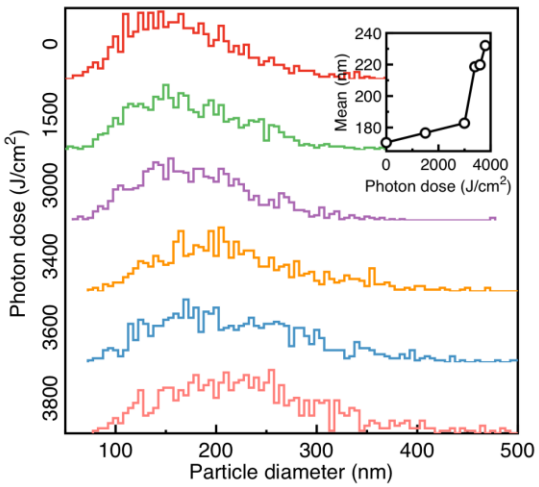

Figure S4. Distribution of crystal particle size obtained from AFM images in Figure3C. Inset: Mean particle diameter as a function of photon dose.

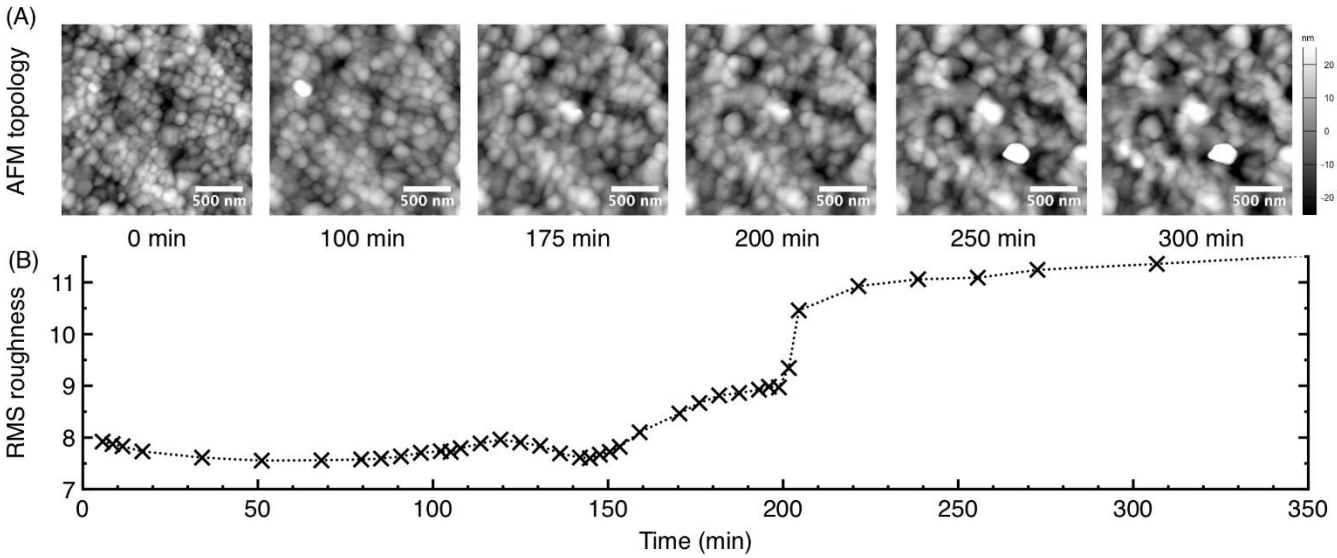

Figure S5. (A) *in situ* AFM topology images (2 × 2 μm) of a $MAPbI_3$ film in air (r.t. 55%RH) with 113 mW/cm^2 irradiation. (B) Corresponding RMS roughness as a function of time.

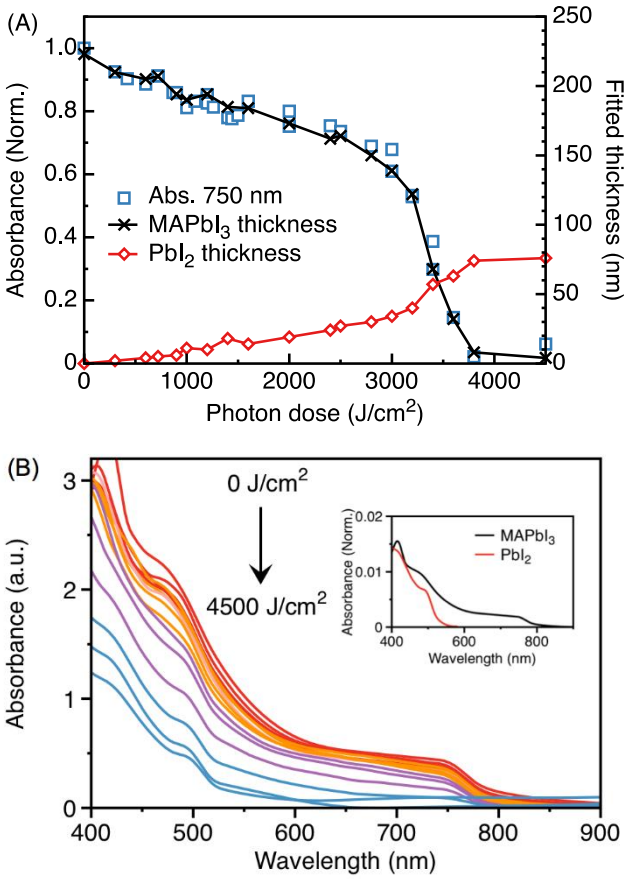

Figure S6. (A) Normalized absorbance at 750 nm and calculated thickness of $MAPbI_3$ and PbI_2 components within the degraded films. The values were obtained by fitting the absorption spectra of neat $MAPbI_3$ film (218 nm) and PbI_2 film (97 nm) to the spectrum of each degraded film (B). Inset: Absorption spectra of the neat $MAPbI_3$ and PbI_2 films normalized by the thickness. A molar percentage was computed from the thickness data multiplied by the molar ratio of $CH_3NH_3PbI_3$ and PbI_2 in a film, which is assumed as 1:1.997 using the density values of $CH_3NH_3PbI_3$, (4.16 g/cm^3)[1] and PbI_2 (6.16 g/cm^3).

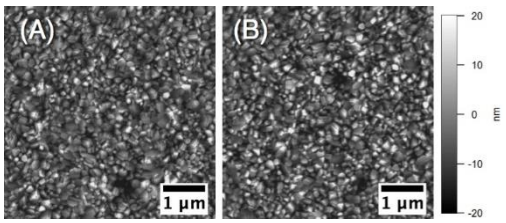

Figure S7. AFM topology images (5 × 5 μm) of (A) a fresh $CH_3NH_3PbI_3$ film and (B) a film stored in 40% RH humid air in the dark at room temperature for 11 hours.

Modified Elovich kinetic fitting

The Elovich equation[2] has been widely applied to evaluate these adsorption kinetics, using the equation

$$dq_t/dt = \alpha exp(-\beta q_t) \quad \text{(S1)}$$

where q_t is the amount of vapor adsorbed at time t, and α and β are constants. The constant α is the initial adsorption rate, which depends on the activation energy, as q_t approaches zero. Using $q_t = 0$ at $t = 0$, equation S1 can be integrated into

$$q_t = \frac{1}{\beta} ln(t + t_0) - \frac{1}{\beta} lnt_0 \quad \text{(S2)}$$

where $t_0 = 1/\alpha\beta$. Assuming the absorption of the perovskite decreases as water molecule adsorbed to the surface of the perovskite, we write equation S3 and fit to the decay traces in Figure 5 to obtain values of α and β.

$$I_t = I_0 - q'_t = 1 - \frac{1}{\beta} ln(t + t_0) + \frac{1}{\beta} lnt_0 \quad \text{(S3)}$$

where I_t is the normalized absorbance at photon dose t, q'_t is the water vapor adsorbed at photon dose t normalized to the intensity. Identical t_0 value, such that I_t vs $\ln(t + t_0)$ becomes a straight line, was applied throughout the fitting (Figure S8, fit lines). The calculated values are summarized in Table S2.

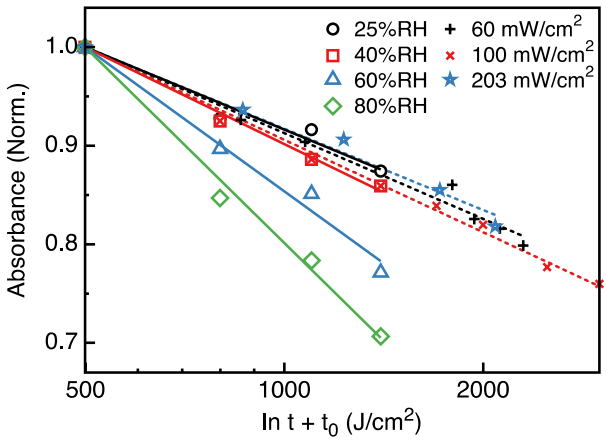

Figure S8. Modified Elovich kinetic plots for the adsorbances at various humidity and intensity in Figure 5 as a function of photon dose ($t + t_0$). t_0 value (498.98) was optimized to make I_t vs ln ($t + t_0$) straight lines.

Table S2. Calculated Values of α and β in the modified Elovich Equation[a]

RH (%)	α (cm^2J^{-1})	β	R^2
25	2.41×10^{-4}	8.31	0.954
40	2.84×10^{-4}	7.06	0.991
60	4.22×10^{-4}	4.75	0.983
80	5.73×10^{-4}	3.50	0.991
Intensity (mW/cm^2)	α (cm^2J^{-1})	β	R^2
60	2.52×10^{-4}	7.97	0.981
100	2.71×10^{-4}	7.39	0.993
203	2.39×10^{-4}	8.40	0.983

[a]R^2 = correlation coefficient.

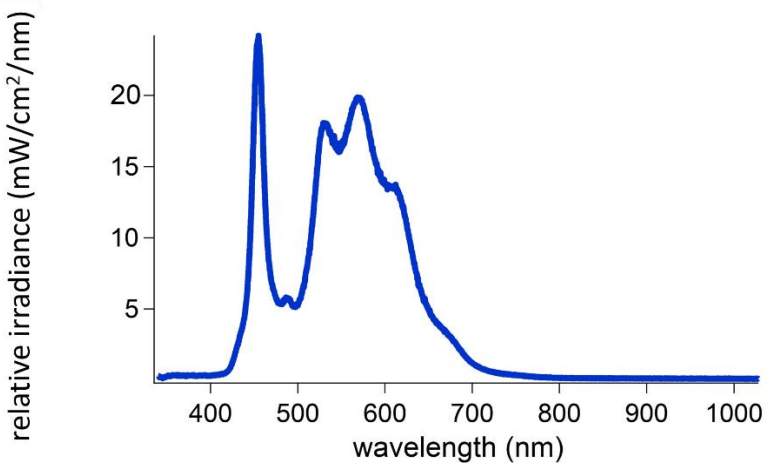

Figure S9. Cool white LED spectrum used for degradation showing relative irradiance.

References

1. Stoumpos, C. C.; Malliakas, C. D.; Kanatzidis, M. G. Semiconducting Tin and Lead Iodide Perovskites with Organic Cations: Phase Transitions, High Mobilities, and near-Infrared Photoluminescent Properties. *Inorg. Chem.* **2013**, *52*, 9019-9038.
2. Low, M. J. D. Kinetics of Chemisorption of Gases on Solids. *Chem. Rev.* **1960**, *60*, 267–312.

Appendix D *Supporting Information for Chapter 4.1*

Methods

Materials

Unless otherwise stated, all materials were purchased from Sigma Aldrich or Alfa Aesar and used as received. Methylammonium iodide (MAI) were purchased from Dyesol Ltd.

Perovskite Fabrication

Thin films were fabricated on fluorine doped tin oxide (FTO) substrates (TFD inc.). These were sequentially cleaned by sonicating in dilute detergent, acetone, and isopropanol, and subsequently treated with oxygen plasma for 10 minutes. A compact titania layer was spincoated on top of FTO and sintered at 500 °C with ramping temperatures for 2 hours. Perovskite thin films were fabricated in a nitrogen-filled glovebox using a one step-deposition and solvent annealing method. Perovskite inks of 30% wt. % were made from stoichiometric amounts of MAI and $Pb(Ac)_2$ in DMF solvent with 8 µL of HPA as the final step. Substrates we spincoated at 2000 rpm for 45 s and room temperature annealed for 10 mins. Samples were then place on a petri dish on a hot plate at 100 °C with 15 µL of filtered DMF solvent. The substrates and DMF were covered to allow for solvent annealing for 5 min. Samples were promptly removed and appeared shiny and grey after solvent annealing.

Characterization

Scanning Probe Microscopy All topography and PFM images were taken using a Cypher ES with dry nitrogen in the dark for all measurements. All images were taken with a 75 kHz Cr/Pt conductive tip with 3 N/m force constant (BudgetSensors).

XRD X-ray diffraction was carried out using a Bruker D8 diffractometer.

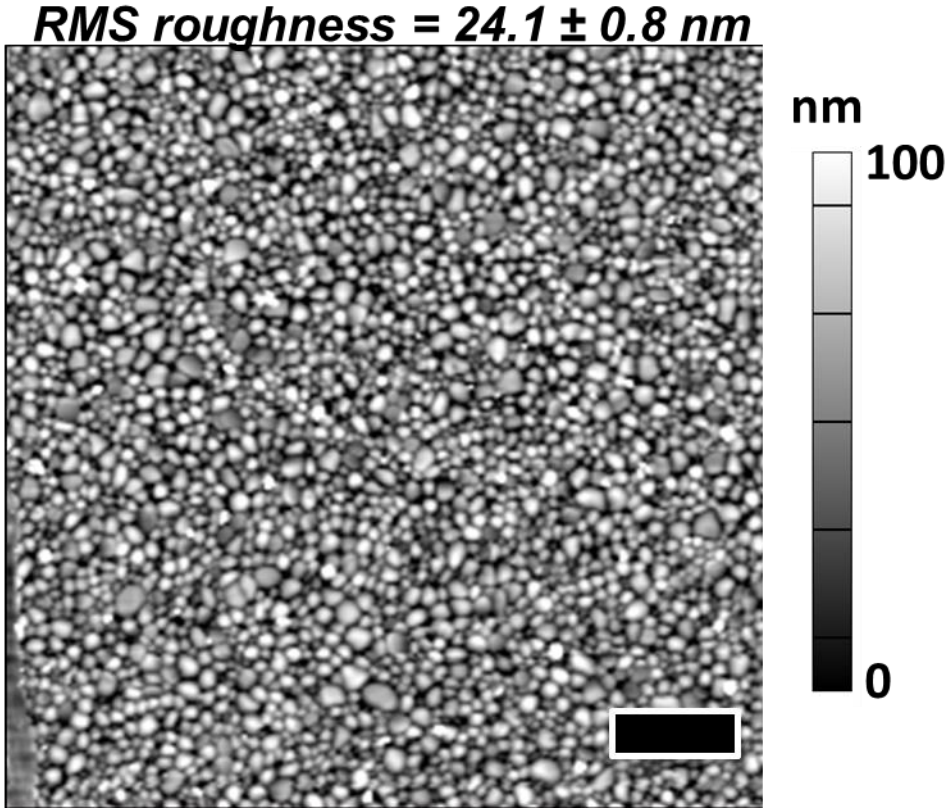

Figure S1 30 x 30 um scan of solvent annealed MAPI film at room temperature using standard tapping mode AFM. Scale bar = 5 um. Roughness is calculated from the average of 6 different 30 x 30 μm images.

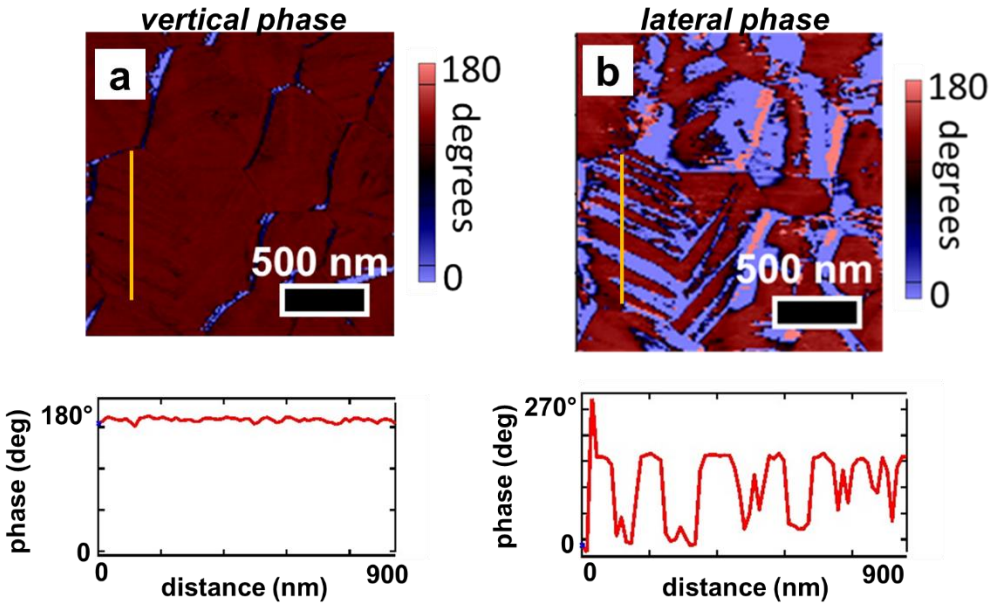

Figure S2 Phase maps from both a) vertical and b) lateral PFM including line scans across same grain.

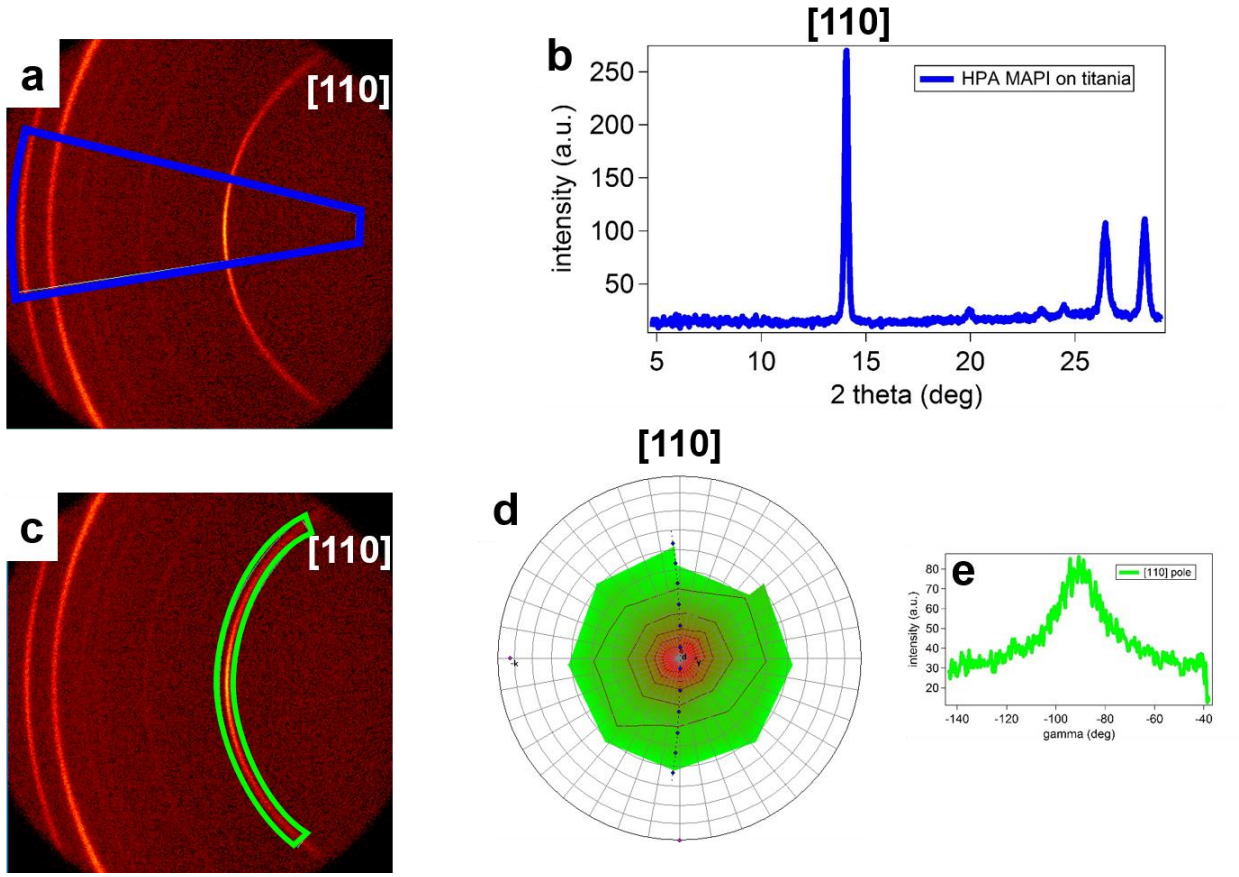

Figure S3 Figure 4 XRD results on $CH_3NH3PbI_3$ film. (a) area diffraction with blue box showing region integrated for (b) XRD pattern; (c) same area diffraction as (a) showing green box around (110) plane; (d) pole figure for (110) plane of $CH_3NH3PbI_3$; (e) trace across one slice of pole figure (i.e. along line in green box in (c)).

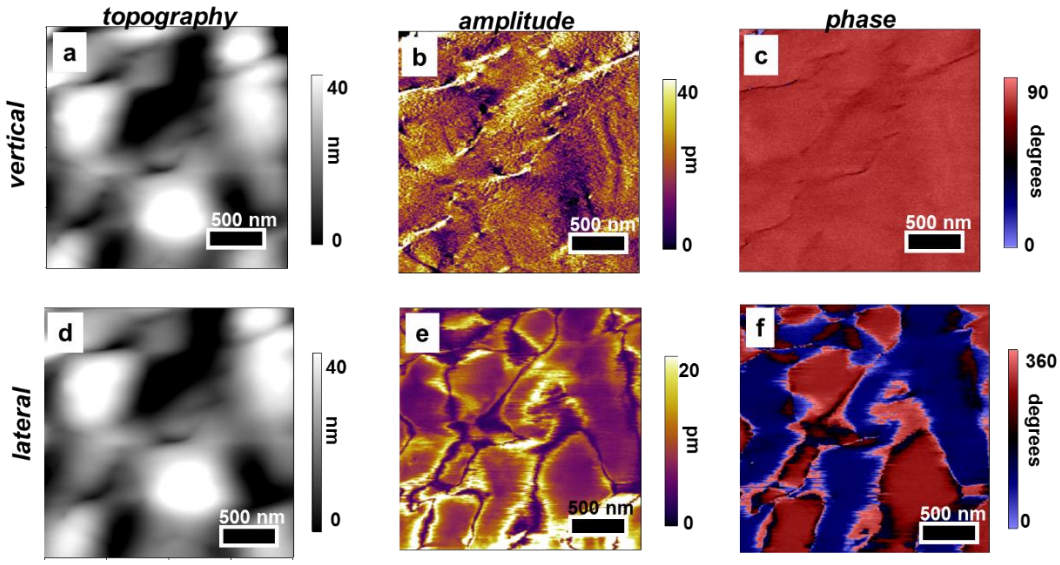

Figure S4. Micrographs from vertical PFM and lateral PFM taken on CsPbI3 films on titania substrate. a) topography, b) out of plane amplitude and c) out of plane phase; d) topography, e) lateral amplitude and f) lateral phase taken on the same 2x2 µm location.

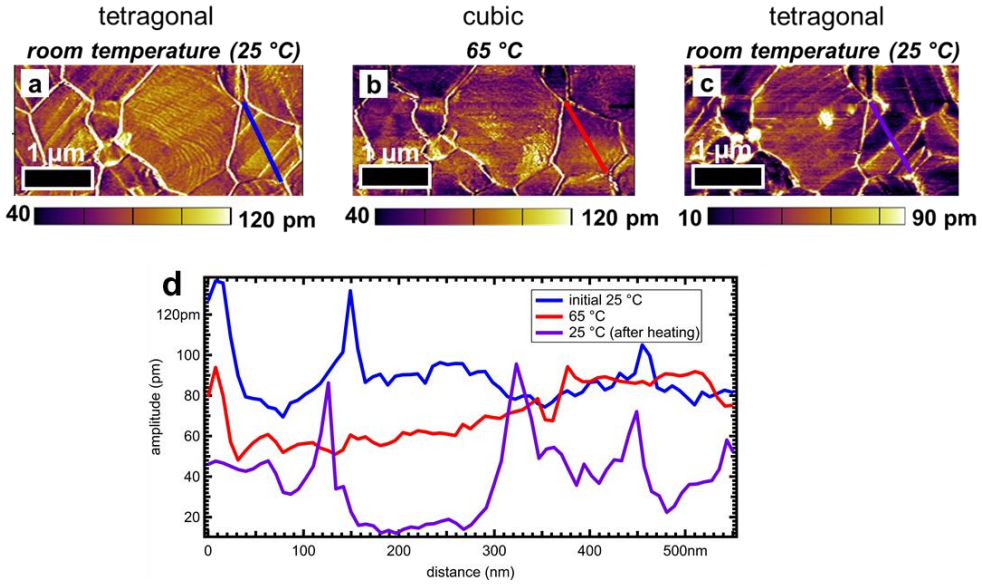

Figure S5. Line scans across same grain from Figure 2 comparing DART amplitude signal as a function of temperature.

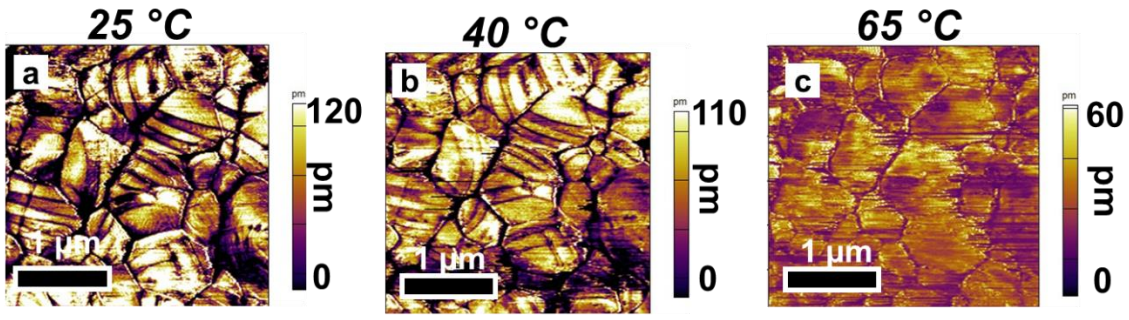

Figure S6 Vertical (DART-mode) amplitude around tetragonal to cubic phase transition at 55 °C showing disappearance of domains above transition.

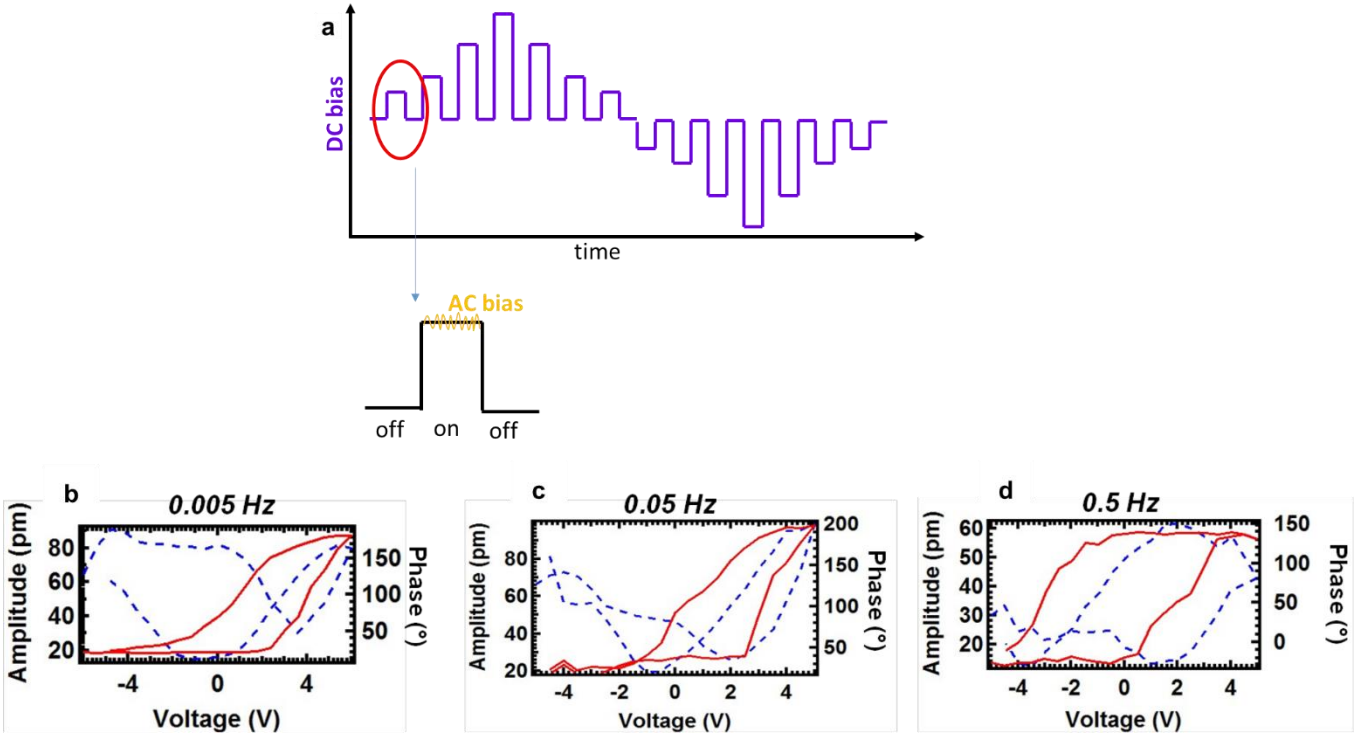

Figure S7 Waveform from DART switching spectroscopy and frequency dependent hysteresis loops (red trace) and butterfly curves (blue dotted trace) with slower scan rates showing a slowly collapsing hysteresis loop.

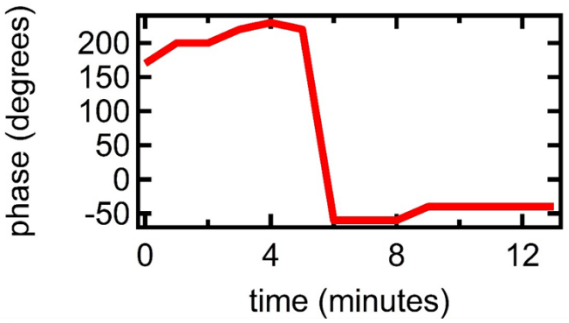

Figure S8 Phase from DART-mode PFM as a function of time immediately after poling with +2.8 V. Phase is seen to flip back after 6 minutes.

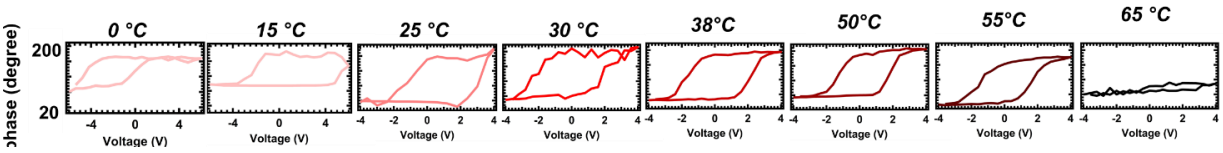

Figure S9 Temperature dependent hysteresis loops from DART-mode switching spectroscopy showing a collapse in the signal past tetragonal to cubic phase transition.

VITA

SARAH M. VORPAHL

EDUCATIONAL BACKGROUND

PhD University of Washington, Chemistry expected August 2017
Thesis: "Nanoscale Characterization of Organic/Inorganic Thin Film Photovoltaic Materials Using Electrical Scanning Probe Microscopy"
GPA 3.49
PhD concentration in Public Policy and Management June 2016
BS Northeastern Illinois University, Chemistry December 2011
Graduated Summa Cum Laude
GPA 3.98
BA University of California Santa Cruz, Modern Literary Studies December 2004
Minor: History of Art and Visual Culture
GPA 3.45

RESEARCH EXPERIENCE
University of Washington, Seattle WA
2012-present

Advisor: Prof. David S. Ginger and Prof. Hugh Hillhouse

- Characterizing next generation photovoltaic materials using novel scanning probe microscopy and correlating with scanning electron microscopy and photoluminescence imaging

Northeastern Illinois University, Chicago IL 2010-2012
Advisor: Prof. Kenneth T. Nicholson

- Imaged structural changes of IR fluorescent photoreceptors using scanning tunneling and atomic force microscopy

Washington State University, Pullman WA 2011

Advisor: Prof. Kerry W. Hipps
NSF Research Experience for Undergraduates

- Characterized single layers of small molecules in acid using liquid cell scanning tunneling microscopy

University of Chicago, Chicago IL 2010

Advisor: Prof. Steven Sibener
NSF Research Experience for Undergraduates

- Characterized self-assembled monolayers and polymer blends for superhydrophobic films using atomic force microscopy

COMMUNITY ACTIVITES
Women in Chemical Sciences, University of Washington
Founder/Member 2012-present
President 2012-2014
http://students.washington.edu/wcsuw/

- Founded student led organization that currently includes 75+ members and is fully funded and supported by the Department of Chemistry

- Awarded three Danz Endowed Lectures from the Graduate School to bring high impact speakers to give large public lectures at UW:

Amy Cuddy (Associate Professor of Business Administration, Harvard) 2013
Jill Cornell Tarter (Bernard M. Oliver Chair for SETI) 2015
Anita Sarkeesian (Director, Feminist Frequency) 2016
WA State Department of Commerce, Intern 2017
- Communicating achievements and goals of Clean Energy Fund to public and policy making audience
Clean Energy Ambassador 2013-present
Clean Energy Institute, University of Washington

- Organized/participated in outreach events focused on educating the public and local government officials on renewable energy topics and research taking place at UW
Strengthening STEM through Diversity, Organizer 2016
University of Washington

- Organized one day conference bringing together over 100 students, faculty and staff from 30 departments on campus and in the Seattle community to discuss mentorship and community building for minoritized students in STEM fields; raised over $4000 in funds from various student groups and departments on campus.
Diversity in Clean Energy, Student Officer 2016-present
Clean Energy Institute, University of Washington

Women Chemist Committee Chair 2015- 2016
American Chemical Society, Puget Sound section
Puget Sound Women Chemists Retreat, Organizing Committee 2015
Pack Forest Conference Center, Eatonville, WA
UW Chemistry Graduate Club, Social Chair 2014-2015
Graduate Student Symposium Planning Committee, Speaker Chair 2013-2014
248th ACS National Conference, San Francisco, CA

COMMUNITY ACTIVITIES
Volunteer Work

DJ, Rainy Dawg Radio, University of Washington, Seattle, WA 2016
Photonics Fair, University of Washing, Seattle, WA 2016
Expanding Your Horizons Conference, Seattle, WA 2013-2016
Mercer Island Science Fair Judge 2016
Paws on Science, Pacific Science Center, Seattle, WA 2013-2015
Shoreline STEM Festival, Shoreline, WA 2015
Huskies on the Hill, Olympia, WA 2014
Echo Lake Science Night, Shoreline, WA 2014
Seattle Science EXPO, Seattle Science Festival, Seattle, WA 2013
Life Sciences Weekend, Pacific Science Center 2012
SACNAS National Conference, Seattle, WA 2012
Public Workshops and Lectures
"Thriving in Graduate School with Peer Mentoring", UW Seattle 11/05/15
"Future of Energy: Solar Cells from Plastic," Lecture, UW Bothell, 10/06/14
"Mentoring Up!," Panel Session, UW Seattle, 03/31/14
"It's not just you! A workshop on impostor syndrome", Workshop, UW Seattle, 11/02/13

PUBLICATIONS AND PRESENTATIONS
Publications

1. Matsumoto, F., Vorpahl, S., Banks, J., Sengupta, E., and Ginger, D., "Degradation Kinetics and Morphology Evolution of Organometal Halide Perovskite Solar Cells."Journal of Physical Chemistry C, 2015, 119 (36), pp 20810–20816

2. Xin, H, Vorpahl, S., Collord, A., Braly, I., Uhl, A., Kruegerc, B., Ginger, D., and Hillhouse, H., "Lithium-Doping Inverts the Nanoscale Electric Field at the Grain Boundaries in Cu2ZnSn(S,Se)4 and Increases Photovoltaic Efficiency," Physical Chemistry Chemical Physics, 2015, DOI: 10.1039/C5CP04707B

3. DeQuilettes, D., Vorpahl, S., Stranks, S., Nagaoka, H., Eperon, G., Ziffer, M., Snaith, H., Ginger, D., "Impact of Microstructure on Local Carrier Lifetime in Perovskite Solar Cells," Science 348, 6235, 2015, 683-686

4. Nagaoka, H., Ma, F., deQuilettes, D., Vorpahl, S., Glaz, M., Colbert, A., Ziffer, M., Ginger, D., "Zr Incorporation into TiO2 Electrodes Reduces Hysteresis and Improves Performance in Hybrid Perovskite Solar Cells while Increasing Carrier Lifetimes, J. Phys. Chem. Lett., 6, 4, 2015, 669-675

5. Salvador, M.*, Vorpahl, S.*, Xin, H., Williamson, W., Shao, G., Karatay, D., Hillhouse, H., Ginger, D. "Nanoscale Surface Potential Variation Correlates with Local S/Se Ratio in Solution-Processed CZTSSe Solar Cells" Nano Letters, 14, 12, 2014, 6926-6930

6. Jahanbekam, A., Vorpahl, S., Mazur U., and Hipps, K.W., "Temperature Stability of Three Commensurate Surface Structures of Coronene Adsorbed on Au(111) from Heptanoic Acid in the 0 to 60 °C Range" J. Phys. Chem. C, 117, 6, 2013, 2914–2919

7. "Better Batteries for Future Energy Demands," Xconomy, 10/12/2015

Presentations

1. Vorpahl, S., Eperon, G., Moerman, D., Giridharagopal, R., Ginger, D., "Ferroelectric Domains Correlate with Charge Extraction in Perovskite Thin Films," poster presentation, Orcas 2016: International Conference on Energy Conversion and Storage, 2016, Friday Harbor, San Juan Islands WA.

2. Vorpahl, S., Moerman, D., Glaz, M., Ginger, D., "Electrical Scanning Probe Microscopy of Perovskite Solar Cell Films," poster presentation, 12th International Symposium on Functional π-electron Systems, 2015, Seattle, WA.

3. Vorpahl, S., Karatay, D., Harrison, J., deQuilettes, D, Ginger, D., "Understanding Advanced Materials for Energy by Analysis of Scanning Probe, Electron and Fluorescence Microscopy Images," Joint NSRC Workshop, Oak Ridge National Laboratory, 2015, Oak Ridge, TN

4. Vorpahl, S., Nagaoaka, H., Ma, F., Ginger, D., "Characterizing Long Range Order of Dipoles in Methyl Ammonium Lead Trihalide Perovskites using Piezoresponse Force Microscopy," poster presentation, Orcas Conference 2014, Friday Harbor, WA.

5. Vorpahl, S., Xin, H., Hillhouse, H., Ginger, D., "Doping Changes the Potential at the Grain Boundaries in Cu2ZnSn(S,Se)4 Photovoltaic Absorber Layers," poster presentation, 248th ACS National Conference, San Francisco, CA

6. Vorpahl, S., Xin, H., Hillhouse, H., Ginger, D., "Doping Changes the Potential at the Grain Boundaries in Cu2ZnSn(S,Se)4 Photovoltaic Absorber Layers," poster presentation, Puget Sound Women Chemists Retreat, University of British Columbia, Vancouver, Canada

7. Salvador, M., Vorpahl, S., Xin, H., Williamson, W., Shao, G., Karatay, K., Hillhouse,H., Ginger, D., "Correlating Surface Potential Variation with Varying S/Se Ratio in Cu2ZnSn(S,Se)4 Solar Cells," oral presentation, Fall 2013 MRS Conference, Boston, MA

8. Jahanbekam, R., Vorpahl, S., Mazur, U., Hipps, K.,"Understanding Temperature and Concentration Dependence in the Supramolecular," poster presentation,2011 SACNAS National Conference, San Jose, CA